A MICROFLUIDIC DIGITAL MELT PLATFORM FOR SENSITIVE BIOMARKER ANALYSIS AND PARALLELIZED PROFILING OF MOLECULAR HETEROGENEITY

by
Christine M. O'Keefe

A dissertation submitted to Johns Hopkins University in conformity with the requirements for the degree of Doctor of Philosophy

Baltimore, Maryland
March 2020

© 2020 Christine O'Keefe
All Rights Reserved

Intended to be blank

Abstract

Variability in gene regulation is a fundamental characteristic of biology, allowing cellular adaptation in many states, such as development, stress response, and survival. In early disease onset, genetic and epigenetic variability permit the formation of multiple cellular phenotypes. In cancer, increased cellular plasticity ultimately results in the foundation of a tumor with the phenotypic alterations necessary to dynamically adapt, proliferate, metastasize, and acquire therapeutic resistance throughout the course of the disease. One prominent form of cellular regulation is DNA methylation, an epigenetic chemical modification that can alter gene expression. Hypermethylation-induced silencing is known to occur early on in tumorigenesis, often in precursor phases of the disease. Furthermore, tumors have been shown to undergo epigenetic reprogramming throughout progression of the disease. In light of these observations, methylation heterogeneity may serve as a novel biomarker for early cancer detection.

Early detection of cancer remains challenging, as symptoms often manifest in later stages and current screening techniques often lack the requisite sensitivity and specificity. To maximize effectiveness, routine screening techniques should be noninvasive, simple, and unbiased. To this end, liquid biopsies (e.g. blood samples)

containing cellular debris, such as tumor-derived cell-free DNA in the plasma, are ideally suited towards routine screening. However, detection of tumor-derived molecules in plasma is challenging, as they are often rare and may be eclipsed by a high background of molecules from healthy cells. Thus a sensitive platform capable of quantifying epigenetic heterogeneity could uncover new insights and improve early detection.

In this dissertation, I present a microfluidic digital melt platform for facile, highly-sensitive detection and molecule-by-molecule profiling. The platform is applied towards the quantification of epiallelic heterogeneity. Digitization of rare molecules into thousands of microchambers followed by parallelized sequencing interrogation through high resolution melt enables order of magnitude higher sensitivity than current techniques and insight into new intermolecular characteristics. I also demonstrate how this platform may be modified to complement and improve the sensing capabilities of existing commercial technologies. Finally, I validate the potential clinical utility of this platform through detection of methylation heterogeneity in complex clinical samples towards noninvasive screening applications. The technical capabilities along with the operational simplicity of this platform facilitate adoption by other laboratories and offer potential clinical utility. This system may offer new insights into the mechanisms of epigenetic regulation in pathogenesis, and potentially improve early diagnosis.

Advisor: Tza-Huei Jeff Wang
Committee members: Dr. Ishan Barman, Dr. Tian-Li Wang, Dr. Tza-Huei Jeff Wang

Acknowledgements

First I would like to thank my family for all their unconditional support throughout the years. My parents, Fran and Jerry O'Keefe, who encouraged me when I needed it and continued to try to help even when they started to grow frustrated with the verbiage I used in my academic papers. My siblings, Genevieve, Thomas, and Celeste, who occasionally slipped in some sincere words of support and encouragement when I needed it alongside their only moderate teasing about my endless years in school. Truly, I am incredibly grateful for such a close-knit family that keeps me grounded and can always have a good time together.

I would like to thank God for the great many blessings He has given me. He provided me with the tools I needed to perform this research and persevere for the last several years in graduate school.

My principle advisor, Dr. Jeff Wang, who has been very supportive. He guided my intellectual and professional development through the past several years of my PhD. He constantly demanded the best of me and the lab, and drove me to reach higher and to be able to accomplish more in my research. I also want to thank my additional mentor, Dr. Tom Pisanic, who struggled with me through several years of troubleshooting and disappointments, allowed me to vent in frustration, and offered encouragement to continue working.

Thanks to my thesis committee: Dr. Tian-Li Wang and Dr. Ishan Barman. I am very grateful for the time they dedicated to helping me fulfill my requirements, and their thoughtful suggestions on how to improve my work.

My fellow labmates were a shining light of hope throughout many difficult times during my PhD, and I could not have sanely pursued this journey without them. The ones who came before me, especially Helena Zec, Wen Hsieh, Natt Athamanolap, and Ye Zhang, set a high bar for performance in the lab that I constantly strove to meet. Their mentorship and comradery were invaluable throughout my PhD. My co-year oldtimer, Anu Kaushik, who worked in the trenches of droplets with me. Yang Zhao, who for some reason thought my project was worth going through the same struggle together. Fanen Chen, Pei-Wei Lee, Alex Trick, Liben Chen, Pengfei Zhan, Dongjin Shin, Sixuan Li, Andrew Li, Joon Soo Park, Alejandro Stark for keeping up my spirits and having fun both inside and outside the lab.

I owe much gratitude to the scientific and private organizations that had enough faith in me to fund my research: the National Science Foundation Graduate Research Fellowship Program, the P.E.O. organization, and the Siebel organization. I will continue to work so that their faith was not misplaced.

Many of my friends outside of lab supported me and put up with many rants in the past years of PhD. Without them I might not have finished, they provided so much encouragement. Thanks to Katy McVay, Emily Guo, Melanie Zile, Ethan Nyberg, Caitlin Walker, Emily Rodriguez, Rachel Thompson, Laura O'Hanlon, Pippa Sykes. And thank you, dear reader, for making it this far in my dissertation.

Finally, I have to thank my now husband, Doctor Sean Hersey. As we took our PhD journeys together, he offered daily support and understanding. Thank you for doing all the cooking when I was busy trying to meet deadlines. Thank you for dealing with my frustration and understanding. Thank you for trying so hard to understand all the details of my problems so that you can try to help me with it. Thanks for writing little matlab programs for me to help my things faster. Thanks for always pushing me to do excellent work.

Table of Contents

List of Tables

List of Figures

Chapter 1

EPIGENETICS IN EARLY CANCER EVOLUTION

Cancer evolution models

Despite the well-known advantages of early cancer detection, many types of cancer are not detected until late stages, when treatment is more challenging and the chance of survival is much lower. Deficiency in early detection may be attributed to both lack of understanding of early cancer development as well as inadequate or lack of compliance with current screening methods. In order to improve the chances of survival, early detection is critical. There are two avenues of approach to increase early detection rates. First, better diagnostic methods should be used that can reliably detect cancer at its early stages. Next, these early biomarkers should be detectable by a simple, routine screening method that is inexpensive and reasonably convenient.

During carcinogenesis, cancers acquire functional characteristics that result in unregulated and aggressive growth. Cancer cells undergo malignant transformation through a progressive acquisition of genomic aberrations, such as mutations, insertions, and deletions, that disrupt the normal regulatory processes of the cell. Numerous studies

have uncovered several “driver mutations” which are well-associated with carcinogenesis [1], [2]. However, due to the numerous possible driver mutations per cancer and their lack of specificity, their diagnostic utility is limited to a small fraction of patients [3].

A universal characteristic of cancers is genomic instability. Many tumors exhibit intratumoral heterogeneity that can be observed early in carcinogenesis [1], [4]. Most models predict that a gradual loss of genomic stability results in the clonal expansion of abnormal cells with increased cellular plasticity [4]–[6]. Tumors are believed to follow a Darwinian selection model, in which a phenotype eventually arises expressing the characteristics of a founder tumor cell that thereby drives tumorigenesis. Further clonal expansion gives rise to heterogeneous clonal populations, permitting the tumor to acquire many of the hallmark phenotypic alterations that allow cancer to dynamically adapt, proliferate, metastasize, and acquire therapeutic resistance throughout the progression of the disease [1], [4], [7]–[9].

Epigenetic Regulation

There are many levels of cellular regulation. Historically, many studies have focused on the regulation and aberrations thereof at the genetic level, i.e. the base code of a cell’s DNA. However, transcription and translation of the genetic code goes through numerous checkpoints and undergoes several modifications before reaching functional maturity. Modifications that affect gene expression and are not direct changes to the base code are broadly encompassed in the field of epigenetics. Epigenetic changes include modifications to the backbone of DNA, to the chromatin, to proteins, or to RNA. Most

tumors exhibit hundreds-to-thousands-fold more epigenetic aberrations than mutations [10].

Epigenetic alterations are of particular interest because, unlike genetic alterations, they are reversible. Therefore, identifying tumor-driven epigenetic changes holds promise for treatment options. In fact, several epigenetic therapies are already clinically available [11]–[13]. Results of most treatments are mixed, which warrants further investigation into epigenetic mechanisms.

The most well-studied form of epigenetic modification is DNA methylation, a chemical modification that results in an additional methyl group to a cytosine nucleotide that is followed by a guanine (CpG), considered the "backbone" of DNA. The accumulation of these methylation events, or hypermethylation, can contribute to gene silencing and is known to be aberrant in cancer [12], [14], [15]. Interestingly, many tumors simultaneously exhibit global DNA hypomethylation [9], [13], [14], [16], indicating that methylation has a profound effect on cellular regulation. Recently, studies have found that tumors exhibit DNA hypermethylation silencing in the promoter region of tumor suppressor genes (TSGs) early in tumorigenesis, prompting several studies investigating the use of DNA hypermethylation as biomarkers for early detection of cancer [16], [17].

Epigenetic "Priming"

Many studies have attempted to uncover the molecular origins of cancer, but the foundational events are still elusive and thus are under academic debate. Traditionally,

progressive mutations are thought to be the driving events of tumorigenesis. However, recent evidence points to epigenetic and methylation aberrations as preceding events to driver or passenger mutations, which "prime" the genome for genetic abnormalities [18]. Several models have predicted that epigenetic plasticity within chromatin structure, histone variants, or miRNAs, can permit or even cause genetic alterations [4]–[6], [16].

Epigenetic silencing occurs most frequently at earlier, precancerous stages of tumor development, and thus can be detected during or even prior to the development of precursor lesions [19]–[21]. There is also recent evidence to support that epigenetic aberrations such as DNA methylation may occur before genetic alterations (such as mutations) [18], [22]. For example, many colon cancers demonstrate overexpression of the *Wnt* pathway [23]. Precancerous lesions were found to have hypermethylation in the *SFRP* gene family, which interact with *Wnt* pathway receptors [23], [24]. Hypermethylation-induced silencing of these genes persisted in those lesions that progressed to primary colon cancers, whereas none of these lesions possessed any mutations known to be related to the *Wnt* pathway. This suggests that epigenetic silencing predisposed the precursor legions to genetic changes associated with clonal expansion, ultimately leading to tumorigenesis [18]. This process has been described as "epigenetic sensitization," in which aberrant epigenetic events confer the neoplasticity required for clonal expansion.

Variable methylation

DNA methylation occurs as a stochastic process, and can thus vary on a patient-by-patient and even cell-by-cell basis [1], [25], [26]. In fact, the extensive level of

"nonsynonymous" alterations, that is those not shared between patients, indicates that carcinogenesis many occur via numerous possible pathways [1]. The precise effects of this variability and heterogeneity are only beginning to be elucidated. Nonetheless, very recent studies have observed that intermediate DNA methylation heterogeneity is predictive of metastatic versus localized clones in Ewing sarcoma [27], and that recurrent methylation reprogramming of numerous CpG sites across the epigenome in acute myeloid leukemia patients occurs throughout the progression of disease [28]. Therefore, further investigation into the temporal scope of DNA methylation heterogeneity on a single CpG site basis could provide greater insight into tumor cellular reprogramming mechanisms.

A number of mathematical models have posited that variability in DNA methylation patterns starts to increase in adenomous precursor tissue [29], [30]. Using meta-analysis of genome-wide methylation data, some studies have shown that measuring variance in CpG methylation within a region can serve as a better predictor of disease than mean methylation levels [20], [31]. This model corresponds intuitively with our understanding of stochasticity in cellular regulation [32]. In one study, hypervariable CpG sites were identified in patients three years prior to diagnosis of cervical cancer [30].

We propose that analyzing this genetic variability is key to understanding critical phases in cancer development and progression (Figure 1.1). By better characterizing genetic and epigenetic variability, especially in precancerous phases, we hope to improve early detection and diagnosis.

Screening through liquid biopsies

Recently it has been found that disease-associated cell-free DNA (cfDNA) can be readily found in patient blood plasma. This discovery has opened new avenues for molecular diagnostics and prognostics in many diseases [33]–[36]. So-called "liquid biopsies" of cell-free DNA (cfDNA) provide several advantages over traditional techniques by offering sampling that is noninvasive, heterogeneous, and unbiased, prompting increasingly more research into its clinical utility as a diagnostic and theranostic platform [37]–[41]. Perhaps the most prominent applications of liquid biopsies are aimed at early detection and therapeutic monitoring of cancer, whereby liquid biopsies can provide a simple, noninvasive means of sampling DNA derived from throughout the body [42]–[44]. In fact, several studies have shown that genetic and epigenetic molecular aberrations, such as mutations, copy number variations and DNA methylation correlate with tumor evolution and can likewise be found in cfDNA in the plasma [45]–[48].

Liquid biopsies provide a simple and non-invasive solution to high-throughput analysis of patient samples, and are currently in use to monitor therapeutic resistance, prognosis, and in screening for biomarkers. However, cfDNA is typically present in concentrations of <50ng/ml in the plasma [17], of which fractions as low as 0.01% may be tumor-derived strands [42]. Of the tumor-derived fraction, we endeavor to examine the methylation heterogeneity among epi-alleles. Consequently, detection of these ultra-rare biomarkers requires extremely sensitive and specific analysis techniques.

Methods of Detection

To detect methylation patterns of DNA, most techniques rely on bisulfite conversion. Bisulfite conversion is a chemical process that converts unmethylated cytosines to uracils, thereby creating a sequence change that is representative of the template methylation status (Figure 1.2). Methylation Specific PCR (MSP) [49] is a technique designed for sensitive detection of locus-specific methylation by using primers specific only to fully methylated sequences. MSP and its derivatives, such as SMART-MSP [50], Methyl-Light [50], and real-time qMSP [51], [52], can detect methylated fractions as low as 0.01%,. However, these methods are semi-quantitative and are restricted to a single methylation pattern; thus they are impractical for quantification of DNA methylation heterogeneity on a single CpG site resolution of rare samples, such as those found in a liquid biopsy.

Molecular analysis has been significantly advanced by techniques such as next-generation sequencing and digital PCR (dPCR) approaches, namely droplet digital PCR (ddPCR), but currently available instrumentation has significant drawbacks that impede its applicability for detection and assessment of heterogeneity within rare molecular variants. Although sequencing can provide genome-wide sequence information, it has limited sensitivity, requiring 2,000-5,000 reads to achieve 0.1% analytical specificity [53], and has been shown to have critical shortcomings in sequencing repetitive sequences, such as found within CpG islands [54], [55]. Coupled with its complex workflow and high cost, these limitations undermine its utility for routine detection of very rare biomarkers.

In contrast, current dPCR-based methods such Methyl-BEAMing [56] and MethyLight ddPCR [57] offer a cost-effective approach to achieve single-copy sensitivity,

but also only detect a specific methylation pattern, thus precluding their ability to detect and quantitate heterogeneous methylation patterns. An ideal technology should be able to combine the advantages of these two techniques, and permit detection of rare and heterogeneous DNA patterns (Table 1).

High Resolution Melt (HRM) is a facile means of assessing sequence variations within a target locus by measuring the release of DNA intercalating dye during temperature-dependent denaturation. Current commercial dPCR technologies, such as the QX200 (Biorad) and Raindance systems, have limitations preventing ready adaptation to HRM as a molecular profiling tool, while most non-commercial ddPCR technologies with real-time monitoring capabilities require droplet trapping before monitoring, severely compromising throughput [58], [59]. Although a number of commercial array-based dPCR strategies do exist, namely QuantStudio (ThermoFisher) and Biomark (Fluidigm), they lack HRM analysis capabilities, likely due to numerous technical challenges. The limited number of in-house attempts have generally been encumbered by significant obstacles, such as maintaining thermal control and uniformity throughout the device [60], achieving sufficient sequence resolution of a few nucleotides [61], observing dim fluorescence and optical noise from small reaction volumes as well as managing stochastic amplification variations from digital starting concentrations [62]. These issues primarily stem from fundamental limitations in commercially-available hardware or the use of off-the-shelf analysis software.

DREAMing

To that end, we designed and developed an assay, termed Discrimination of Rare Epi-Alleles by Melt (DREAMing), that interrogates the methylation status of a target sequence on a molecule-by-molecule basis, described fully in our previous work [63]. In essence, primers were developed for a PCR-type assay that are methylation-*preferred*, such that all epi-allelic variants of the target sequence can be amplified, but methylated templates experience an amplification bias, permitting single-molecule sensitivity amongst high background DNA. The methylation status is interrogated by DNA Melt analysis, which utilizes an intercalating dye to visualize denaturation of ds-DNA during temperature ramping. The temperature at which exactly half of the strand is denatured is termed the "melt temperature" for that sequence. A single methylation mark, after bisulfite conversion, causes the amplicon to denature at a higher temperature due to the increased stability of C-G hydrogen bonds and base stacking. In DREAMing, two melt temperatures are identified, one for the unmethylated background and one for the methylated variant. Due to the digitization of methylated variants, DREAMing represents a quantitative analysis of DNA methylation heterogeneity.

While DREAMing has shown many promising results, its initial implementation contains some drawbacks. In principle, DREAMing requires digitization of rare template molecules from a bulk solution. The probability of sample digitization within a well is given by the Poisson distribution:

$$P(n, \lambda) = (\lambda^n e^{-\lambda})/n!,$$

where n is the number of target molecules and λ is the ratio of positive wells to total wells. Thus for the sample to be confidently digitized in a 96-well plate, no more than 9 of the

wells should contain the rare target molecule, severely limiting the dynamic range and amount of heterogeneity that can be assessed. One possibility to circumvent these issues is the use of a larger plate or multiple plates. However, many plates are needed to significantly improve the sensitivity, and doing so would be both cost and time-prohibitive in reagent consumption and excessively long reaction times. Thus, while the DREAMing technique provides a means of evaluating methylation at single-copy sensitivity, the unavailability of commercial high-density, HRM-capable instrumentation restricts its use for many research and clinical applications.

Overview of dissertation

The goal of this dissertation is to provide a facile means of detecting and quantifying rare and heterogeneous genetic and epigenetic biomarkers in complex samples among a high background population. To address this technological gap, I utilized a comprehensive bottom-up approach involving both hardware and software solutions aimed at addressing these technical challenges. This was achieved by design and fabrication of a microfluidic platform called HYPER-Melt (High-density Enumeration and Profiling by Melt), consisting of a 4096 nanoliter-well static array microfluidic device and optical-thermal platform for digital PCR and digital HRM. This high-density array can digitize and analyze thousands of individual molecules while limiting reagent consumption to that of a typical microtiter well, and provide an absolutely quantitative measure of sequence heterogeneity within a target locus throughout a molecular population. The presented all-in-one chip design is simple to fabricate and use, offers a consolidated workflow, enables

rapid and automatic loading and digitization, and is robust to reaction conditions. The optical-thermal setup minimizes light scattering and thermal instability, and I introduce a post-processing software solution that can be employed to circumvent irregularities imposed by hardware limitations thereby permitting reproducible HRM-curve acquisition.

I incorporated the DREAMing technique into the HYPER-Melt platform to achieve highly parallelized assessment of intermolecular methylation variation at single-copy sensitivity. The capabilities of this platform were validated through serial dilutions of mixed epialleles, with demonstrated detection limits as low as 1 methylated variant in 2,000,000 unmethylated templates (0.00005%) of a classic tumor suppressor gene, *CDKN2A* ($p14^{ARF}$).

Next, I improved the applicability of this platform towards detection of rare biomarkers by improving the efficiency of target detection. By implementing a multilayer device design and other geometric strategies, flow through the device can be passively manipulated to encourage less sample waste. I demonstrated improvements in loading and detection efficiency of the platform, resulting in an increased detection efficiency from 15% to 80%. Furthermore, I describe a novel capture device that can bridge the digital melt platform with existing commercial technologies for wider adoption and higher-throughput towards large patient cohorts.

Next, I expanded the capabilities of the platform by enabling the assessment of methylation heterogeneity of biomarker panels through development of a dual-probe identification scheme that is fundamentally scalable to high degrees of multiplexing. The strategy involves ratiometric probe-based identification, incorporating “wobble” bases in

order to form methylation-agnostic probes. In addition, I designed and developed a multicolor imaging platform to enable rapid target identification, capable of wide-field fluorescence imaging of up to four colors.

Finally, I assessed the clinical utility of this platform as a novel screening tool for cancer in complex biological fluids. First, I present a digital assay for and N-myc downstream-regulated gene 4 (*NDRG4*), a tumor suppressor gene that is commonly methylated in colorectal cancer. I discriminated methylation patterns of the *NDRG4* locus in liquid biopsies of healthy and colorectal cancer patients. Next, I present a high-throughput device for assessment of methylation biomarkers in DNA extracted from Pap Specimens in both healthy and ovarian cancer patients.

Overall, the HYPER-Melt platform allows for extremely sensitive quantification and analysis of methylation heterogeneity, and provides multi-dimensional information about single molecules that could offer greater understanding of intermolecular variability with respect to biological processes such as carcinogenesis and development.

Specific Aims:

1. **Develop a microfluidic platform capable of ultra-sensitive detection and HRM-based discrimination of locus-specific sequence modifications.**
    1.1 Develop and fabricate a microfluidic device for evaporation-resistant dPCR
    1.2 Design and construct a thermal-optical platform for parallelized, high-resolution melt curve acquisition
    1.3 Develop scalable image processing and data analysis pipeline for epiallelic discrimination

2. **Develop a high-throughput device for efficient sample loading and compatibility with commercial instrumentation.**

    2.1 Improve microfluidic array to detect and discriminate rare epialleles with minimal sample loss

    2.2 Perform ultra-high throughput droplet-based epiallelic discrimination for commercial compatibility

    2.3 Develop image segmentation method for real-time droplet analysis

3. **Develop the capability for assessment of methylation patterns of a panel of biomarkers**.

    3.1 Demonstrate feasibility of ratiometric fluorescence multiplexing scheme

    3.2 Construct multicolor fluorescence optical instrumentation

4. **Assess the performance of quantifying DNA methylation heterogeneity in complex samples in noninvasive sampling approaches**.

    4.1 Detect and quantify methylation heterogeneity of lung cancer markers on circulating DNA from liquid biopsies

    4.2 Detect and quantify methylation heterogeneity of ovarian cancer markers in cervical-vaginal fluid

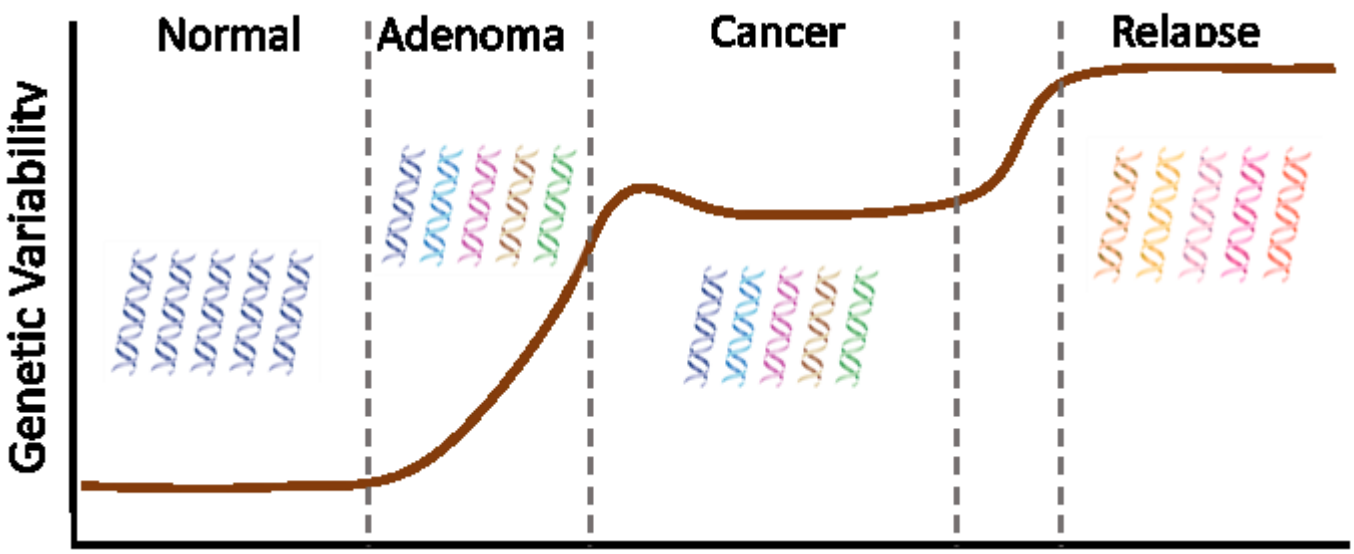

Figure 1.1. Genetic Variability in Tissue Stages

The genetic variability of cancer is predicted to be highest at precancerous stages, just before neoplastic transformation. Therefore, genetic variability may be a candidate biomarker for early cancer detection.

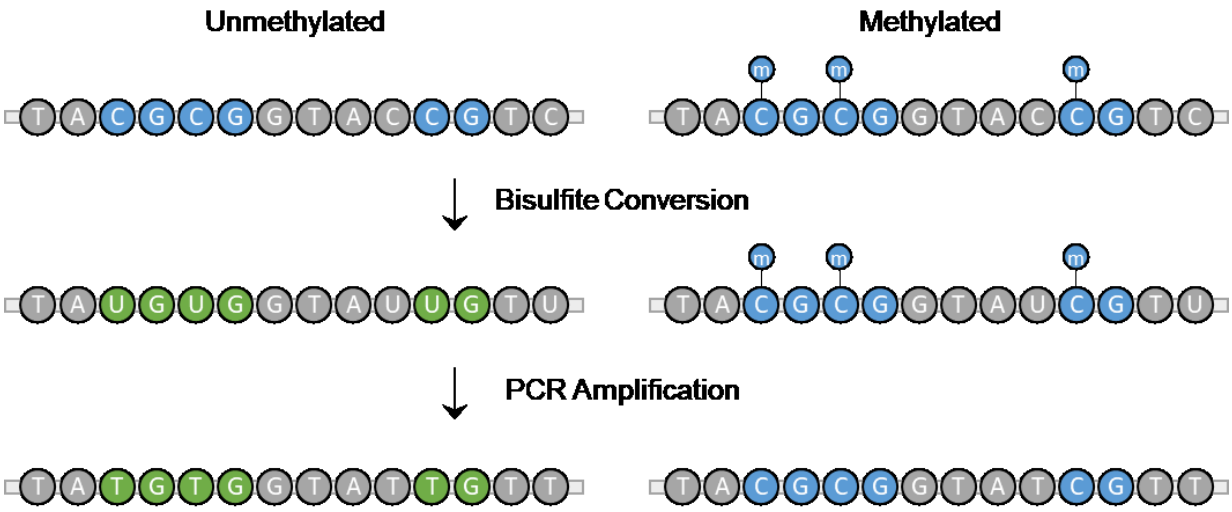

Figure 1.2: Bisulfite Conversion of DNA

After bisulfite conversion, unmethylated cytosines are converted to uracil, but methylated cytosines are not. After PCR, this results in a sequence change.

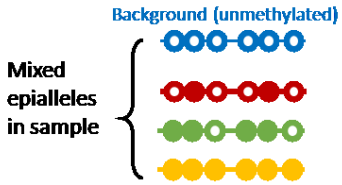

Technique	MSP	Sequencing	ddPCR	Ideal*
Heterogeneous Detection	1 target	All targets	1 or 2 targets	All targets
Sensitivity	0.01%	0.1%	<0.01%	<0.001%

Table 1. Methylation Detection Methods

Existing technologies for quantifying methylation are assessed for their sensitivity and quantitation of heterogeneity. Red indicates insufficient performance and green indicates sufficient.

Chapter 2

HIGHLY PARALLELIZED MOLECULE-BY-MOLECULE ANALYSIS WITH DIGITAL MICROFLUIDICS

Microfluidics and Digital Technologies

Many diseases constitute intermolecular heterogeneity early in development as a fundamental means to acquire a selective advantage and proliferate. Notably, even infrequent outliers in a population can significantly alter clinical outcome. To better understand cellular or molecular populations on a molecule-by-molecule basis requires efficient methods of single-molecule analyses. Traditional PCR analysis techniques, such as quantitative PCR (qPCR), detect an ensemble measurement of all molecules present in a solution. Due to the requirement of standards for quantification, qPCR is only semi-quantitative. Furthermore, when target molecules exist in a high background, qPCR often demonstrates insufficient sensitivity for detection. To perform a true molecule-by-molecule

analysis, each molecule must be segregated from the rest of the population. In traditional formats, physical separation of every molecule in solution is unpractical and requires exhaustive use of reagents and materials.

The advent of digital microfluidic technologies has significantly improved single molecule detection and analysis. Microfluidics enables rapid manipulation of small volumes of fluid, thereby facilitating digitization of individual molecules into discrete chambers. The ability to compartmentalize samples into droplets for high-throughput measurements has greatly improved sensitivity towards detection of rare molecules and has opened doors for new insights into single cell and single molecule analyses [64]–[68]. Digital analysis provides much higher sensitivity as well as absolute quantification; thus is ideally suited for detection of rare molecules and quantification of intermolecular heterogeneity.

Two primary strategies have been proposed for microfluidic digitization of samples into small volumes. The first is a static array, in which the fluid is loaded into a low-aspect-ratio planar device and subsequently divided into individual chambers of sub-microliter volumes. Alternatively, a volume of aqueous solution may be serially emulsified into droplets. Droplet platforms have fundamentally higher throughput potential, but often involve more complex instrumentation and are not suited towards real-time analyses. Therefore, we focus our attention primarily on the static microchamber strategy to achieve real-time molecule-by-molecule profiling.

There are two fundamental challenges in performing digital PCR (dPCR) on sub-microliter volumes. First, the small volumes are highly susceptible to evaporation, thus

eliminating any signal. Second, the individual reaction chambers must remain robustly digitized throughout the reaction to prevent cross-contamination and false positives. Several microfabricated chips for digital PCR have been proposed by other laboratories. To address evaporation, most of them involve a complicated fabrication step to insert an evaporation barrier [69], [70]. While effective, this step complicates the fabrication process and is not scalable. To digitize the chambers, most designs utilize mechanically-intensive micro-valves for partitioning [69]. Actuated microfluidic valves require increased complexity in microfabrication and in device operation. During the repeated fabrication step, multiple layers, a valve and a fluidic layer, must be fabricated and aligned. Then, in order to actuate the valves, a complex pressure regulation system with multiple inputs and outputs is required. Thus, the complex fabrication and operational equipment have hitherto significantly hindered adoption of digital analysis techniques.

Here we present an ultra-thin digital microfluidic device that can accommodate high temperatures for extended periods while minimizing evaporation. The device utilizes a very simple fabrication scheme, and can achieve a limit of detection of 100 attomolar of synthetic target. We show that performing dPCR in this device presents a practicable way to quantify rare targets, especially in high background. We demonstrate proof-of-concept use of this device to identify synthetic DNA representative of methylated *CHFR*, a potential biomarker for many diseases, in high background. We believe that this simple and cost-effective technique will enable wider adoption of dPCR.

Digital Device Design

We sought to prevent evaporation without the need for specialized equipment or materials and without the addition of layers that may introduce noise in the fluorescence signal. The design presented here emphasizes simplicity and avoids such complications by utilizing a single fabrication layer, surface-tension partitioning, and readily available laboratory equipment. Furthermore, surface tension-based partitioning can be scaled to higher density arrays and higher degrees of digitization in future work.

In our device, sample loss and optical scattering were mitigated by the development and use of an ultra-thin fabrication technique (Figure 2.1) to reduce the external volume of PDMS. We aimed to fabricate a single pattern layer with <25 μm between the height of the pattern and the surface of the PDMS. However, PDMS membranes with a thickness of less than ~100 μm experience strong adhesion to a high-aspect-ratio silicon mold, and are likely to tear during removal, damaging both the mold and chip. Therefore, our technique utilizes a sacrificial PDMS layer to enable imprinted-release of the 60 μm pattern layer from the mold without tearing and with high reproducibility. The incorporation of the ultra-thin pattern layer, a glass coverslip, and hydration lines effectively prevents evaporation during digital PCR [71], minimizes optical interference, and reduces thermal deviation, critical to digital melt analysis.

We next sought to validate this design for its two primary functions: (1) to examine whether the new fabrication method sufficiently inhibited evaporation and permitted repeated thermal cycling and (2) whether dPCR could be executed on the device.

Device Loading and Evaporation Reduction

To provide simplicity in operation, the device utilizes a vacuum-assisted loading method followed by surface-tension partitioning to rapidly fill and digitize each microchamber. Samples were initially prepared by mixing the reagents and sample off-chip. The chip undergoes desiccation after fabrication to produce a negative pressure differential across the seal of the inlet (Figure 2.2). When punctured, the sample was drawn into the device by the force of the vacuum, filling all the wells in less than five seconds. Next, an oil-based solution is pressure-driven through the channels. Surface tension between the partitioning oil and the aqueous reaction mixture prevents the oil from entering the wells, thus isolating and digitizing the template molecules, typically in less than 3 minutes. During the PCR reaction, the oil remains pressurized to prevent the sample from exiting into the channels. The addition of PDMS in the partitioning oil produces a solidified, permanent barrier between reaction chambers that is maintained throughout the assay. This technique allows the microfluidic chip to be easily transported for digital melt or other analysis without requiring continuous pressurization, and minimizes contamination risk by locking the post-PCR samples in place.

The simple, thin-chip microfabrication technique employed reduced the evaporation by an order of magnitude compared to traditional microfluidic devices, which overcomes a critical problem for high temperature assays. Given the same reaction conditions, an average of 8% evaporation can be seen per well on the thin chip, whereas 80% of the reaction evaporates after 60 cycles on a device with standard thickness (Figure 2.3). This reduction allows for assays that require many cycles, such as high-sensitivity single-molecule analyses, to be completed on the microfluidic chip.

Digital PCR

After amplification, fluorescent images of the device were acquired from a Typhoon scanner. The resultant image was loaded into Matlab for analysis, and the average fluorescence of each well was calculated. Each well may be identified by a binarization of the grayscale image using an automatic threshold defined by Matlab's built-in Otsu method. After processing, plotting the average fluorescent intensity of each well produces a bimodal histogram, (Figure 2.4. and an average signal to background ratio of 10:1 was calculated. A sample raw image can be seen in Figure 2.4. The two populations are separated by Matlab's multithresh, and the resulting number of positive and negative wells are counted. The occupancy can be calculated using the equation

$$Occupancy = N_{total} * \mathrm{LN}\left(N_{total}/N_{negative}\right),$$

which assumes a Poisson distribution of positive target throughout the wells of the chip, where N is the number of wells.

The microfluidic device can be used to perform digital PCR across a range of concentrations. The segmentation of the reaction mixture into many wells reduces the background such that single events become quantifiable. We demonstrated digital PCR for concentrations ranging from 100 – 0.1 fM. The calculated results closely match the expected results, as shown in Figure 2.5. A linear fit of the data produces a line with $R^2 = 0.999$ and a slope of 0.88. These results indicate that the device is incredibly precise, although roughly 10% of the target DNA may be lost during sample preparation or during

loading. The exact mechanism of loss warrants further investigation. Nevertheless, the device achieves sensitive detection and absolute quantification across 4 orders of magnitude, down to 0.1 fM.

Discussion

The development of a robust digital PCR device meets a clinical need for detection and quantification of rare genetic events. Rare mutations or allelic variations can be biomarkers of disease. A device that can quantify these rare events at a digital level can allow for early detection of these biomarkers. We have shown that this microfluidic device can quantify rare events, and performs at a robust and reproducible level.

The implementation of digital microfluidic devices has been limited by fabrication and usability. The device presented here requires only simple fabrication techniques and is facile to use. Minimization of evaporation is essential for running PCR on a PDMS device. This challenge has led most other dPCR devices to employ a complex fabrication method [69], [70], [72]. However, we demonstrate a technique that minimizes evaporation without any additional use of equipment or materials. In addition, the device presented here does not require valves, which necessitate external operating equipment. Rather, it utilizes a single layer and a single inlet, minimizing the external equipment required to operate. This method may allow wide adoption of dPCR throughout the microfluidic community.

Further improvements to this system include increasing the limit of detection and multiplexing the reaction. Increasing the limit of detection can be achieved by expanding

the grid of wells, therefore increasing the partitioning of the sample. One challenge in incorporating an increased number of reaction wells is the resolution of the imaging system. A new, ultra-high resolution imaging mechanism is required in order to increase well density without expanding the size of the chip beyond feasible dimensions. Multiplexing the reactions on the device becomes less challenging with a high-resolution imaging system. Without separation of targets, however, care must be taken to avoid nonspecific amplification. Nevertheless, this method of fabrication will drive adaptation and progress in the field of digital PCR.

In this work, we have applied a unique fabrication method to build ultra-thin PDMS-based microfluidic devices for dPCR. The method can be adopted in any laboratory and obviates the need for complicated processes such as CVD or spin-coating of polymers, thereby limiting the time and cost of fabrication, as well as making dPCR technology more accessible. Wider adoption of this sensitive and powerful technology may facilitate advances in detection of rare biomarkers.

Methods

Device Fabrication

The device consists of five layers, a break-out of which is shown in Figure 2.2A. One blank wafer is spun with 15:1 PDMS at 2100 rpm and another blank is spun with 6:1 PDMS at 100 rpm, which serves as a temporary layer. After baking for six minutes, the 6:1 blank layer is peeled from the wafer and placed over the 15:1 PDMS. This combination bakes for six more minutes to loosely bond the two PDMS layers. The two bonded PDMS

layers are then removed from the wafer and attached to a thin glass slide via O_2 plasma bonding (15:1 side facing the glass). After bonding and a five minute bake, the sacrificial PDMS layer can be peeled from the chip, leaving just the thin layer. A similar process is used to fabricate the thin pattern layer, using 15:1 PDMS for the silanized pattern wafer (900 rpm) and 6:1 PDMS for a temporary blank layer (100 rpm). Finally, a thin glass coverslide is plasma bonded to the top PDMS layer to reduce evaporation, and an adaptor placed over the inlets to interface with tubing.

Device Loading and Thermocycling

The PCR reaction mixture consisted of 16.6 mM $(NH4)_2SO_4$,67mM Tris pH 8.8,10mM β- mercaptoethanol, 1X ROX Reference dye (IDT), dNTPs (10 mM, ThermoFisher Scientific), Forward and reverse primers (0.3 uM, IDT), 0.08 U/μL Platinum Taq Polymerase (ThermoFisher Scientific), TAQ Probe (0.2 μM), synthetic DNA target (IDT), 0.1% Tween-20 (MilliporeSigma), BSA (New England Biolabs), and water (Quality Biological). 1.1 g of uncured PDMS (Ellsworth) mixed at a ratio of 10:1 (base:crosslinker), and 5 g of silicone oil (100 cst, SigmaAldrich) composed the oil phase.

The chip undergoes desiccation after fabrication to produce a negative pressure differential across the seal of the inlet (Figure 2.2). When punctured, the sample was drawn into the device by the force of the vacuum, filling all the wells in less than five seconds. Next, an oil-based solution is pressure-driven through the channels. Surface tension between the partitioning oil and the aqueous reaction mixture prevents the oil from entering the wells, thus isolating and digitizing the template molecules, typically in less than 3 minutes. During the PCR reaction, the oil remains pressurized to prevent the sample from exiting into the channels. The addition of PDMS in the partitioning oil produces a

solidified, permanent barrier between reaction chambers that is maintained throughout the assay.

The device is thermocycled on a flatbed peltier for up to 60 cycles (5 minutes of 95°C, then 60 cycles of 15 seconds at 95°C and 60 seconds at 60°C).

Imaging and Image Processing

Chips are imaged on a Typhoon 9410 Variable Mode Imager at 10 μm resolution. Fluorescent images are obtained for both the TaqMan probe (FAM) and the reference dye (ROX). Following detection, the images are imported into Matlab for processing and analysis. A mask is overlaid with the image file. The resulting image contains fluorescent data from only the areas of interest. The central pixels of each well are used to measure average intensity. Matlab's built-in bimodal population separation function, multithresh, is used to set a threshold for positive wells. Finally, the number of positive and negative wells are counted, and occupancy is calculated assuming a Poisson distribution of reaction mixture throughout the device.

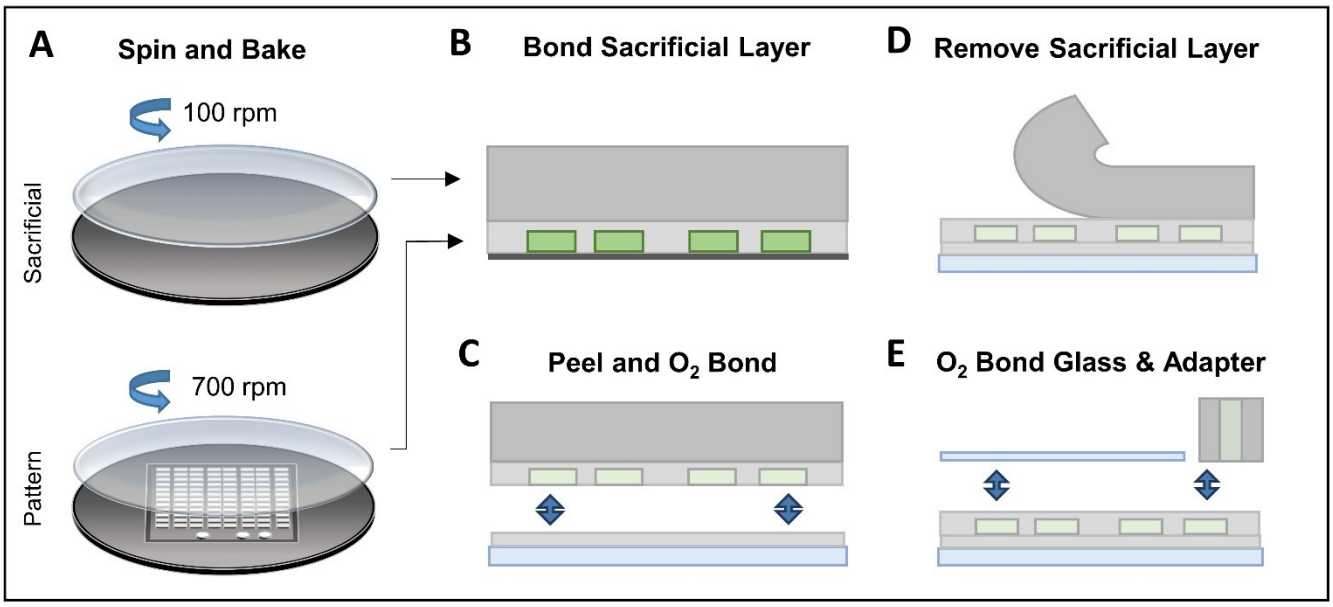

Figure 2.1. Ultra-Thin Microfabrication

(A,B) A sacrificial layer was temporarily bonded to the ultra-thin pattern layer by a brief bake step. This enabled separation of the joint PDMS layers from the mold without tearing of the PDMS. (C) The ultra-thin pattern layer was then O_2-plasma bonded to a PDMS-spin-coated glass slide. (D) After a brief bake step, the sacrificial layer could be removed. (E) Finally, a thin glass coverslide and tubing adapter were O_2-plasma bonded to the surface. This figure is reprinted with permission from reference [73].

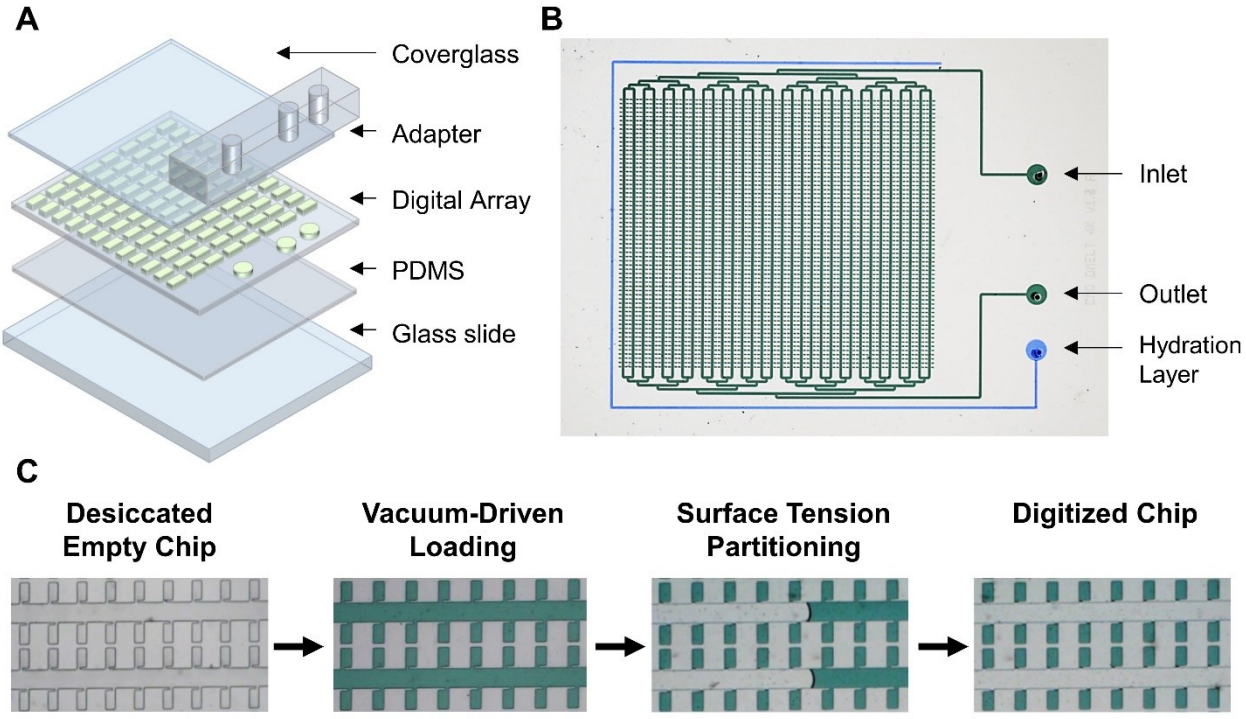

Figure 2.2. Microfluidic device design and operation.

(A) Breakout of the microfluidic chip. The layers include a PDMS-coated glass slide, single PDMS pattern layer, thin glass coverslide, and PDMS tubing adapter for the inlet, outlet, and hydration line. (B) A single ultra-thin pattern layer and hydration line effectively prevent evaporation through the permeable material. (C) The chip is desiccated to produce a negative pressure differential across the inlet. When punctured, the sample mixture automatically loads into the chambers. Next, a partitioning fluid is pressurized through the channels to isolate the reaction chambers. This figure is reprinted with permission from reference [73].

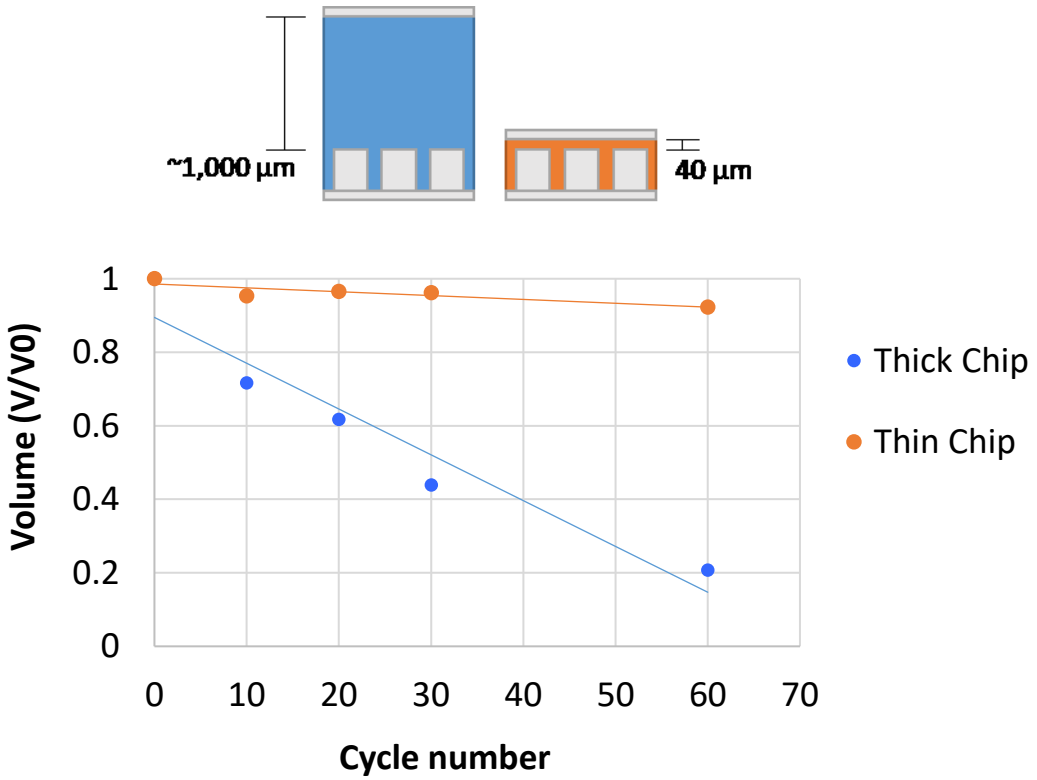

Figure 2.3. Evaporation during PCR.

Thick chips fabricated using conventional techniques experienced 80% evaporation. In contrast, the thin chips only experienced 8% volume loss after 60 cycles of thermal cycling (5 minutes of 95°C, then 60 cycles of 15 seconds at 95°C and 60 seconds at 60°C).

A

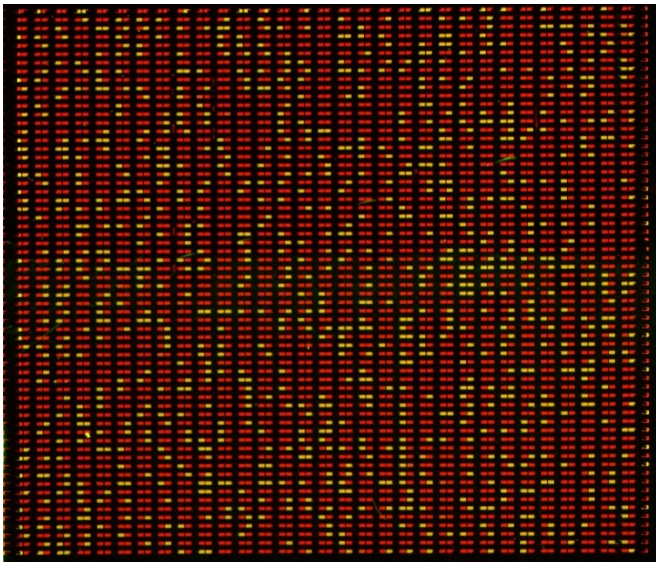

B

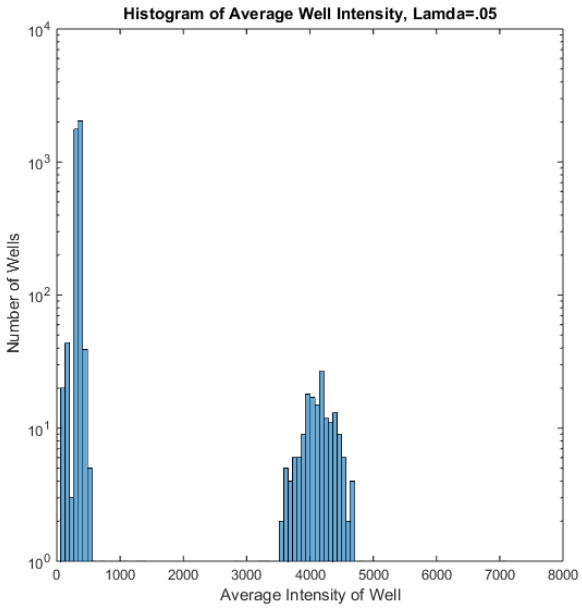

Figure 2.4. Digital PCR Results

(A) Two overlaid fluorescent images of the microfluidic chip acquired by a Typhoon Scanner. The signal image (green) was obtained with 526 nm emission and 488 nm filter, and is overlaid with the reference image (red). After Matlab processing, average intensities

of each well are obtained (B). The sample result shown had an expected occupancy of 0.48 copies/μL and a measured occupancy of 0.44 copies/μL.

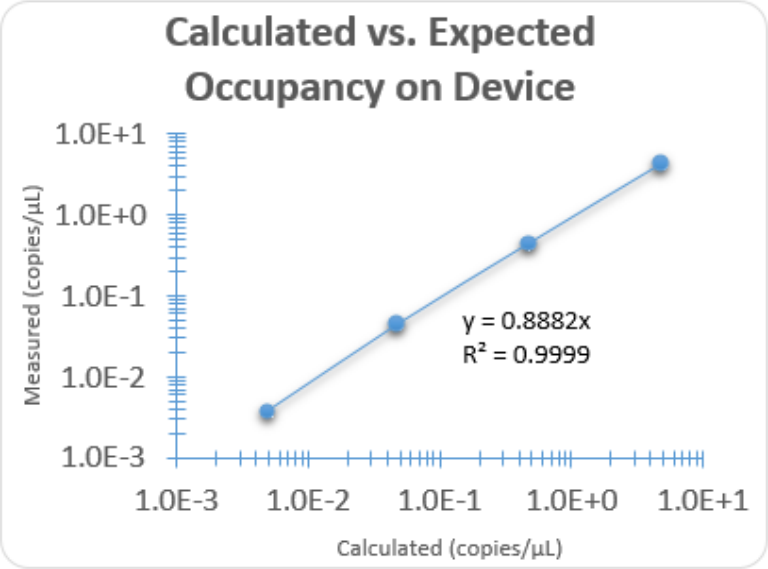

Figure 2.5. Digital Quantification Accuracy

A comparison of expected and measured copies per well. The expected value was calculated based on the stock concentration and dilution in the reaction mixture. The measured value is obtained from digital counting of positive wells adjusted by Poissonian occupancy.

Chapter 3

MICROFLUIDIC DIGITAL HIGH RESOLUTION MELT

High-throughput Parallelized Real-time Analysis

Variability in gene regulation is a fundamental characteristic of biology, allowing cellular adaptation in many states such as development, stress response, and survival. One prominent manifestation of this variability with respect to human health is Darwinian selection within human disease [74]–[76]. From bacterial infections to cancer, diseased populations rely on the ability to generate different phenotypes in order to respond and thrive in their environment [77]–[80]. Hence, many diagnostic principles rely upon the detection of genetic and epigenetic biomarkers, which often consist of minor DNA variations that occur even down to the single nucleotide level, such as mutations, deletions, frame shifts, and methylation, that provide selective advantage [1], [16], [81]. Likewise, in many cases, early detection and diagnosis largely improves the patient's prognosis and

survivability [82]. Although the advent of so-called “digital” analysis technologies has furthered the detection of rare modifications in a binary manner, the stochastic and variable nature of disease onset and progression could be better understood with a more multi-dimensional analysis approach. Thus, a system that enables both rare detection and population profiling on a molecule-by-molecule basis could greatly aid in detection and understanding of disease.

High resolution melt (HRM) is a facile technique that enables multi-dimensional DNA sequence interrogation through measurement of sequence-dependent denaturation with a dsDNA intercalating dye, which could be powerful if applied at a digital level. Where there exist some commercial technologies for digital PCR, there does not yet exist a commercially available system for digital HRM (dHRM). Droplet based technologies, such as Biorad and Raindance systems, rely on a single-point readout, which is not suitable for real-time monitoring of fluorescence intensity. Fluidigm and Life Technologies are not equipped for real-time monitoring and precise temperature control. Furthermore, their cartridges utilize micro-valves for digitization, which require complex external machinery and operation, and are too costly for disposable use, a requirement to prevent contamination in ultra-sensitive analysis. Therefore, they fail to meet several design criteria, such as compatibility with available platforms (often require their own custom/proprietary equipment), scalability to higher throughput, and sufficient input volume.

To perform highly parallelized copy-by-copy DNA molecular profiling, we developed a digital microfluidic platform called HYPER-Melt (High-density Profiling and

Enumeration by Melt). HYPER-Melt provides a facile means of detecting and assessing sequence variations of thousands of individual DNA molecules through digitization in a nano-well microchip array, allowing amplification and interrogation of individual template molecules by detecting high-resolution melt fluorescence changes due to sequence-dependent denaturation. As a model application, HYPER-Melt is used here for the detection and assessment of intermolecular heterogeneity of DNA methylation within the promoters of classical tumor suppressor genes. The capabilities of this platform are validated through serial dilutions of mixed epialleles, with demonstrated detection limits as low as 1 methylated variant in 2,000,000 unmethylated templates (0.00005%) of a classic tumor suppressor gene, *CDKN2A* ($p14^{ARF}$). The clinical potential of the platform is demonstrated using a digital assay for *NDRG4*, a tumor suppressor gene that is commonly methylated in colorectal cancer, in liquid biopsies of healthy and colorectal cancer patients. Overall, the platform provides the depth of information, simplicity of use, and single-molecule sensitivity necessary for rapid assessment of intermolecular variation contributing to genetic and epigenetic heterogeneity for challenging applications in embryogenesis, carcinogenesis and rare biomarker detection.

Overview of Epiallelic Profiling by HYPER-Melt

To achieve high-density molecular profiling, we developed a microfluidic chip and associated instrumentation for digitization and interrogation of individual DNA sequences (Figure 3.1). The chip is first rapidly loaded with the reaction mix containing rare epiallele targets (Figure 3.1A). The chip is then placed on a flatbed heater to perform PCR and

HRM. A mirrorless interchangeable lens camera (MILC) acquires images of the entire chip at each temperature increment during the melt process (Figure 3.1B). The images are processed and analyzed for each reaction chamber to procure a melt curve derivative, from which the location of the peak defines the melt temperature (Figure 3.1C). Finally, the melt temperatures of all the amplicons were calculated to catalog the initial template methylation variants, and compiled in a histogram for quantitative methylation heterogeneity analysis (Figure 3.1D).

Assessment of DNA methylation heterogeneity follows the assay principles laid out in our previous report [63]. Briefly, primers were developed such that they provide methylation-*preferred* amplification, in which all epiallelic variants of the target sequence are amplified, with a significant bias toward the amplification of the partially and fully methylated template molecules. This strategy greatly increases detection sensitivity in the presence of a high background of unmethylated DNA. Post-PCR, HRM analysis is performed by observing the release of a DNA-saturating dye (e.g., EvaGreen) during temperature ramping [83]. As the temperature is increased, the amplicons denature, resulting in a measurable decrease in fluorescence. The temperature at which exactly half of the template strands of a particular amplicon become denatured is termed the melt temperature (T_m) for that target-sequence. Following bisulfite conversion, methylated templates exhibit an increased T_m due to the greater stability of C- versus T-base stacking [84].

In the digital methylation profiling assay, reaction volumes containing both unmethylated DNA and a single rare epiallele produce a melt curve with two peaks. The

left-most peak pertains to the unmethylated/background DNA. The right-most peak corresponds to the rare epiallele, whose methylation density can then be resolved by its T_m. Due to the digitization of differentially methylated epialleles, HYPER-Melt provides absolute quantitation of all methylated variants and overall methylation heterogeneity.

The dynamic range of HYPER-Melt and other digital approaches can be described by the Poisson distribution: $P(n, \lambda) = (\lambda^n e^{-\lambda})/n!$, where the probability that any given chamber will contain n copies depends on λ, the average concentration in copies per chamber volume. For the principle of HYPER-Melt to apply, each chamber may contain no more than one rare methylated variant. By definition, the dynamic range of the device scales with the total number of chambers available. Our proof-of-concept design contains 4096 wells per microfluidic chip, which facilitates detection and discrimination of over 1500 heterogeneously methylated variants simultaneously, and can be readily scaled to higher quantities.

Design of Thermo-Optical Platform

To date, one of the greatest challenges preventing other researchers and commercial imaging modalities from developing a digital melt platform is the high-throughput imaging of a high-density array of sub-microliter volume chambers. The endeavor proved particularly challenging because it incorporated the balance of two typically competing imaging strategies: small-volume real-time fluorescence monitoring and rapid wide-field-of-view acquisition.

Small-Volume Real-Time Image Acquisition

Reductions in reaction volume challenge the capabilities of most continuous fluorescence monitoring equipment. For example, even commercial instruments, such as the Biorad, struggle to produce high-fidelity melt curve results when reaction volumes are decreased below 10 uL. Many of the reported real-time fluorescence tracking microfluidic chips have a very limited number of chambers, use complex imaging components, do not track volumes below tens of nanoliters, and do not have single molecule starting concentrations [60], [85]–[87]. Realization of nano-or micro-liter imaging therefore comes at the expense of field-of-view.

Wide Field-of-View

Large array image acquisition typically requires the use of a microarray scanner or another such imaging setup that includes motion and panning of either the camera or object of interest and subsequent image stitching in order to image the entire volume at high resolution and sensitivity [69], [88]. Another alternative is the use of multiple imaging setups [89]. Although these methods can be very effective at end-point detection, there is a large time cost involved in real-time imaging. Longer melt durations induce photo-bleaching, compound the challenge of maintaining thermal uniformity, and decrease throughput. Thus, these methods are not suitable for a high throughput digital melt platform.

To achieve a digital melt platform capable of high-throughput imaging of a high-density array of sub-microliter volume chambers we sought a compromise between two, often competing, challenging imaging goals: small-volume real-time fluorescence monitoring and rapid wide-field-of-view acquisition.

To reduce the effects of noise that can interfere with the melt signal, we developed an imaging system capable of measuring thousands of small-volume fluorescence variations simultaneously by adapting and optimizing both conventional and unconventional imaging components. In order to increase the signal level and minimize the Poissonian fluctuation of the nanoliter reaction volumes, a multifaceted optimization approach was employed by taking into account the Poissonian statistics and fluorescence efficiency of the excitation light and fluorescence emission, respectively[90].

The probability that a photon reaches a detector can be described by Mandel's Fomula:

$$p(k,\ t,\ T) = \int_0^{\infty} \frac{(\eta_W W(t))^k e^{-\eta_W W(t)}}{k!} p(W(t))\, dW(t) \quad ,$$

where

$$W(t) = \int_t^{t+T} \int_{\boldsymbol{A}} I(r,t) d\boldsymbol{A}\, dt$$

describes the energy of light hitting detector surface. We focus on the relevant components that are controllable, that is *T*, integration time, *W*, emitted photon intensity, *I*, excitation intensity, *p*, the probability of light hitting the detector, *A*, the size of the detector, and *r*, the working distance.

Excitation light intensity was increased via incorporation of multiple LEDs to provide strong and steady excitation, as well as uniform illumination of the sample (Figure 3.2). To increase detection probability of the sensor, we utilized a full-frame 36 x 24 mm sensor, and optimized the image exposure, ISO, and aperture to balance the signal-to-background ratio with a reasonable image capture rate.

In order to perform on-chip heating, we devised a strategy to address local non-uniformities and thermal fluctuations that commonly occur in commercial flatbed heaters, which can greatly compromise data integrity in highly temperature-critical applications such as HRM. To help reduce thermal variations, we employed thermally-stabilizing heat block layers, comprising a flatbed adapter, thermal paste contact enhancer, and a silicon wafer to efficiently transfer heat evenly across its surface. The final stabilizing layer is the glass slide of the digital melt chip itself. Previous attempts used thin glass slides (0.01mm), albeit rapidly conductive, lack rigidity and endured bowing during temperature ramping, thus affecting the heat transfer. Therefore, we substituted a thicker, more rigid glass slide (1mm) to provide thermal dissipation, improve robustness of the chip handling, and achieve more efficient fabrication. The additional thermal stabilization layers increased the thermal uniformity of the chip by 172.3% (Figure 3.3B). With the current setup, melt curves were acquired in just under 10 minutes with a 0.2^{o}C temperature resolution and a Signal to Noise ratio of 5.60 (Figure 3.3C,D).

Validation of HYPER-Melt System

To assess the intermolecular heterogeneity of the amplicons, images of the entire chip were collected during temperature ramping (Figure 3.4). All pictures were aligned to the first image using an open-source Automated Image Registration program (AIR) [91]. Next, the pixel-space locations of each well were semi-automatically identified by a customized Matlab program. The user selects the four corner points of the array image, from which a script generates a linearly scaled mask of the array. Misalignment between

the chip and camera detector is initially corrected by applying a homography transformation of the array mask using the four user-selected points and the generated corners. The well boundaries are then shrunk by 10% on each side so that only the central mass of the mixture is used for measurement. Finally, each well mask within the grid is locally optimized in a 5x5 pixel neighborhood to correct for any additional warping and to identify the center of each well (Figure 3.5).

Once the grid mask is defined, it is propagated throughout each image to obtain the fluorescence intensity values from each pixel at each time point. The outlying points from each well are removed, and the remaining intensity values from each frame within the temperature interval were averaged to obtain a raw curve. Several filters were tested in order to ascertain those that best preserved the integrity of the raw data. A combination of a low-pass filter and Savitz-Golay filter were found to best remove additional noise while still preserving melt information. Next, the derivative was calculated to find the temperature at the inflection point of the melt curve termed the "melt temperature" (T_m). A digital melt histogram was created that reveals the four distinct populations, which can be readily separated by simple thresholding. The methylation density of the original template in each reaction volume was then classified by its melt temperature, providing a quantitative analysis of methylation heterogeneity on a locus-specific, molecule-by-molecule basis.

To assess the capabilities of the HYPER-Melt platform, synthetic targets representative of various bisulfite-converted sequences of the tumor suppressor gene, *CDKN2A* ($p14^{ARF}$), were used as a model system. Four methylation densities were

analyzed: 0%, 33%, 67% and 100%. The unmethylated (0%) sequence represented the background population and was set to 500 copies per nL. The three methylated variants were digitized on chip, amplified and identified by HYPER-Melt. The detected number of targets for each epiallele was calculated by the number of positive melt-discriminated wells while accounting for a Poisson distribution.

In terms of sensitivity, the platform demonstrated absolute quantitation, as the calculated number of copies closely matched the expected number (Figure 3.6). The average number of copies detected represents the combined average of the three epiallelic variants detected per experiment. The experiments for each of 0, 1, and 10 expected copies were repeated. A linear fit produces a slope of 0.91, suggesting that overall, 91% of the expected DNA was detected, with an R^2 value of 0.97. This discrepancy likely represents slight material deformation which deviates from the expected geometry used during calculations. The results of this analysis demonstrate that the HYPER-Melt platform provides robust, absolute quantitation over five orders of magnitude, attaining accurate HRM-based detection down to single copy sensitivity.

A serial dilution of methylated variants at concentrations of 0, 1, 10, 100, and 1000 copies/chip was performed in the presence of the 2 million unmethylated epialleles (Figure 3.7). Representative traces of fluorescence signals from individual wells are shown for each test (Figure 3.7B), which were classified by melt temperature via thresholding and color-coded by methylation density. Once discriminated by melt temperature, the digital result was converted to a methylation density heatmap (Figure 3.7C), which was then further quantified and analyzed via a methylation heterogeneity histogram (Figure 3.7D).

The master mix was divided such that the same reaction volume was loaded into the chip as well as a control benchtop reaction for validation of the PCR and melt success (Figure 3.7E).

Overall, the specificity of the HYPER-Melt platform for rare heterogeneously methylated epialleles was demonstrated down to fractions as low as 1 in 2 million unmethylated copies, or 0.00005%. Even higher specificities are ostensibly achievable by the HYPER-Melt platform as it is only limited by the appropriate dynamic range of the application. Heterogeneously methylated epialleles can be readily differentiated with < 1°C resolution, enabling sequence-specific discrimination of < 4 CpG cites.

Discussion

The HYPER-Melt platform provides a practical and rapid technique for absolutely quantitative assessment of intermolecular variability in DNA methylation levels of a target locus with a demonstrated sensitivity of 1 in 2 million background copies at < 1˚C resolution (~4 CpG-sites). Its clinical applicability was demonstrated with commensurate performance, achieving 20-300X more sensitivity than the gold standard (qMSP), for assessment of methylation heterogeneity of *NDRG4* in liquid biopsies. HYPER-Melt was also compared to more sensitive methods (i.e. ddPCR), where it demonstrated more sensitive detection and discrimination of heterogeneous targets (Figure 3.8). There are number of key innovations that, when combined, enabled achievement of significantly higher HRM sensitivities than previously demonstrated in the literature.

The development of a wide-field-of-view imaging platform is critical to achieving real-time fluorescence monitoring of such a large array of nanoliter reaction chambers. Present commercial digital PCR technologies suffer from a number of key drawbacks and are not yet suitable for digital HRM applications. Droplet-based technologies, such as the QX200 (Bio-Rad) and Raindance systems, rely on a single-point readout, which is not amenable for real-time monitoring of fluorescence intensity. QuantStudio 12K Flex (ThermoFisher) and Biomark (Fluidigm) are not equipped for precise temperature control, and the high cost of their OpenArray (ThermoFisher) and Digital Array IFC (Fluidigm) cartridges undermines their clinical attractiveness. Many of the reported real-time fluorescence tracking microfluidic chips have a limited number of chambers [85], [86], use complex imaging components [60], do not track volumes below tens of nanoliters and do not demonstrate digital starting concentrations [85]–[87]. Other microfabricated chip designs for digital PCR involve a complicated fabrication step to insert an evaporation barrier [69], [70], or utilize mechanically-intensive micro-valves for partitioning [69]. Multi-layer micro-valve partitioning strategies suffer from complex fabrication methods, a limiting valve footprint that reduces scalability potential, and require intricate operational instrumentation. Large array image acquisition techniques usually necessitate the use of a microarray scanner or similar instrumentation that includes motion and panning of either the camera or object of interest, followed by subsequent image stitching or the use of multiple imaging setups in order to image the entire volume at sufficient resolution and sensitivity [69], [88], [89]. Although these methods can be very effective at end-point detection, in real-time imaging they accrue costs of time, photo-bleaching, and thermal

instability, thus rendering these methods not suitable for a high-throughput digital melt platform.

In contrast, HYPER-Melt uses readily-available imaging components, such as an LED array and a commercial MILC, a predominantly automated processing pipeline, and a simple and scalable valve-less microfluidic design to achieve small-volume, wide field-of-view imaging and high-fidelity melt curve acquisition. Because native current commercially available hardware for a thermal-optical platform are not sufficient to produce high-fidelity melt curves in a highly parallelized manner, we optimized the configuration of readily available components to minimize thermal-optical noise and implemented a software solution to extract parallelized single molecule information. A common strategy for object detection in fluorescent images is thresholding; however, this is susceptible to error due to artifacts and requires very uniform illumination of the sample. Alternatively, we introduced a detection technique using a known-mask mapping. This technique capitalizes on the known grid design, and offers several advantages. First, a map generation script was created to allow for automatic generation based on a few geometric user inputs, so that the overall analysis can be universally applied to any grid-based design. Furthermore, the localized well-search algorithm relaxes the requirements of illumination uniformity due to its restriction to the neighborhood of each well.

The presented microfluidic solution provides absolutely quantitative sequence heterogeneity information at ultra-high sensitivity while maintaining the practicality and simplicity necessary for routine use. Notably, recent studies have demonstrated that even minor populations of mutated molecules or heterogeneously-methylated epialleles can

have direct clinical implications. For example, intermediate DNA methylation heterogeneity is predictive of metastatic versus localized clones in Ewing sarcoma [27] and observations of methylation reprogramming on a single CpG site basis in Acute Myeloid Leukemia (AML) patients emphasize that molecular heterogeneity plays an important role in tumor progression and adaptation to the microenvironment [28]. APC mutations at levels as low as 0.01% could be indicative of early colorectal cancer [92]. HYPER-Melt provides an enabling platform for similar studies looking to examine the role of rare, heterogeneous genetic or epigenetic aberrations on a molecule-by-molecule basis without excessive cost and time.

The capabilities of the HYPER-Melt platform were demonstrated with the DREAMing assay [63], designed to detect methylation density of rare molecules amongst a background of unmethylated or perceived healthy molecules. The primers were designed to introduce an amplification bias towards the rare molecules, allowing single-copy detection even in a high background. This approach achieves highly sensitive, absolute quantitation of the digitized methylated variants. There are some drawbacks of this approach, such as the lack of quantitativeness towards the background molecules due to lack of digitization. The T_m corresponds to the number of CpGs that are methylated, which may include several permutations depending on the locus. Further analysis would be required to identify those exact CpG sites. We previously described how a linear regression can be modeled between control points with an *in silico* model (such as *uMelt* [93]) [63]. Such a model specifies the confidence interval of methylation density at each melt temperature and identifies differentiable patterns. A number of factors affect the resolution of the DREAMing assay that should be taken into account when choosing a

locus, as outlined in our previous manuscript [63]. For example, the methylation density of loci that are shorter and have fewer CpGs can be better resolved than longer and denser sequences. The resolution can be tailored by designing primers around the region of interest.

The increased sensitivity, as well as the comprehensive methylation density information realized by HYPER-Melt, provides the opportunity to set more quantitative, multi-parameter threshold values for clinical analysis. Already, DNA methylation has been a subject of some treatment strategies which are clinically available [11], [12]. A facile means of assessing epigenetic heterogeneity, such as the one presented here, might be employed for extending methylation assays from mere detection of the presence of methylation to use as a means of real-time monitoring of tumor progression, evolution and response to therapy. An underlying premise of precision medicine is that most or all cancer cells in a patient share a given targetable genetic (or epigenetic) defect. However, most cancers exhibit significant intratumoral heterogeneity, increasing the likelihood of resistant clones or subclones [94]. Therefore, there is increasing need for genetic and epigenetic profiling of intercellular heterogeneity to identify these resistant clones when applying therapeutic regimens. HYPER-Melt provides a simple means of profiling intermolecular heterogeneity, and, due to its high sensitivity, may thereby enable identification of even rare, potentially-resistant subclones.

HYPER-Melt is readily extendable to many other applications beyond DNA hypermethylation. The ability to fully digitize samples with HYPER-Melt while maintaining considerable dynamic range allows absolute quantification for all methylation

patterns without bias, thereby enabling the assessment of hypomethylation in CpG-sparse loci, which commonly occurs during carcinogenesis [9], [14], [16], [27]. Other applications of fully digital HRM include ultrasensitive detection of rare genetic/epigenetic variants, including mutation and single-nucleotide polymorphism (SNP) detection [95]–[97]. Furthermore, digital melt curve analysis also provides considerable advantages over digital PCR-based approaches by allowing facile verification of PCR products, a critical feature for avoiding false positives in rare target detection and diagnostics. Intermolecular variability is of great interest in other applications such as embryogenesis [98], carcinogenesis [1], [2], [4], and regulatory circuitry [32], [79], for which HYPER-Melt provides a practical and facile means of further investigation.

There are a few drawbacks in the current platform that are of note. One fundamental issue with the microfluidic platform is the potential disparity between sample volume and reaction volume. While our chip was specifically designed to achieve compatibility with existing bisulfite conversion kits, larger samples would likely require incorporation of a concentration method, such as the previously-described, Methylation-On-Beads technique [99]. The reported benefits of the platform are limited to examining a single target in a single sample, which restricts the clinical applications of this platform to those with a well-defined, highly specific locus of interest. Alternatively, multiplexing could be achieved by splitting samples into subarrays, but would require the use of greater sample volumes or additional wells available for digitization to maintain assay performance metrics. Furthermore, the current chip is limited in throughput to the assessment of a single sample per run. Even though eight samples can be run per day, each requires an individual chip, thus the platform has relatively low sample throughput.

However, this limitation is similar to many other digital real-time analysis or sequencing technologies, in which the sensitivity can be increased by dedicating more of the reaction space to a single sample.

In conclusion, HYPER-Melt provides an all-in-one analysis platform of molecular profiling and heterogeneity analysis. The platform allows deep insight at the single copy level of any target of interest. Overall, this platform has the potential to detect intermolecular variability at ultra-high sensitivity even in difficult and highly-heterogeneous samples, allowing more comprehensive investigation of the dynamics and stochasticity of DNA molecular heterogeneity. Furthermore, the practicality and high digitization power of the platform offers a tool for rapid and efficient DNA heterogeneity analysis by rapidly interrogating hundreds to thousands of individual molecules in parallel.

Materials and Methods

Chip Fabrication

Microfluidic chips were fabricated using standard photolithography and soft lithography techniques. To fabricate the reusable master mold, a silicon wafer was dehydrated and oxygen plasma treated (Technics PE-IIA) at 80 W for 1 minute. SPR220-7 photoresist (Microchem) was spun at 2600 rpm for 1 minute and then soft baked at 115ºC for 20 minutes. The wafer was then exposed to the channel pattern using a mask aligner at 1150 J/cm^2 and developed in CD26. After a hard bake at 200ºC for 6 hours, SU-8 3050 was spun on the wafer at 2600 rpm for 1 minute. After a soft bake at 95ºC for 20 minutes,

the wafer was aligned to the well array mask, exposed at 300 J/cm^2, developed, and baked at 200^{o}C for 1 hour.

Each microfluidic chip was fabricated from this mold using soft lithography and our unique ultra-thin ≈80 μm layering technique. The wafer was first silanized to protect the photoresist layers. A 15:1 mixture of poly dimethyl siloxane (PDMS, Ellsworth) was spun on the pattern at 700 rpm, while a 6:1 mixture of PDMS was spun on a blank wafer. Both were baked for 6 minutes at 80^{o}C. The blank, sacrificial PDMS layer was then removed and overlaid on the pattern layer, and baked briefly again. A blank glass slide (Ted Pella) was cleaned with water and dried. 15:1 PDMS was spun on the glass slide at 2100 rpm; then baked at 80^{o}C for 6 minutes. Next, the two partially-bonded PDMS layers on the pattern wafer could be removed jointly. The pattern PDMS layer and the blank PDMS layer on the glass slide were both oxygen plasma treated at 40 W for 45 seconds, then bonded. After bonding, the sacrificial PDMS layer was peeled and removed from the pattern. Finally, a glass coverslip and tubing adapter layer were oxygen plasma bonded to the top surface of the chip. The chip was then baked at 80^{o}C overnight, sealed with a piece of thin adhesive tape over the inlet and outlet, and desiccated for a minimum of two hours before use.

Genomic and Synthetic Control DNA

All synthetic control DNA was obtained from Integrated DNA Technologies (IDT) and used at concentrations based on the manufacturer's specifications. Human male genomic DNA (Promega) and Epitect unmethylated control DNA (Qiagen) were used as unmethylated control genomic DNA. Enzymatically CpG-methylated HeLa genomic DNA (New England BioLabs) was used as a fully-methylated control. Control genomic DNA

was bisulfite converted using the EZ DNA Methylation-Lightning Kit (Zymo Research) according to the manufacturer's protocol and eluted into volumes ranging from 12 – 25 µl. Post-bisulfite treatment yields were quantified by MethyLight using primer and probe sequences for beta-actin recognizing both methylated and unmethylated templates: actin-sense 5'- TAG GGA GTA TAT AGG TTG GGG AAG TT -3'; actin-antisense 5'- AAC ACA CAA TAA CAA ACA CAA ATT CAC -3', spanning a 103-bp region (chr7:5,532,169-5,532,271), and 100nM probe, 5'- \56-FAM\ TGT GGG GTG \ZEN\ GTGATGGAGGAGGTTTAG \3IABkFQ\ -3'. Assays were performed using 10X Master Mix to yield a final volume of 25 µl and final working concentrations of 16.6mM $(NH_4)_2SO_4$, 67mM Tris pH 8.8, 6.7mM $MgCl_2$ 10mM β-mercaptoethanol, 200µM of each deoxynucleotide triphosphate (dNTP) and 0.04 U/µl of Platinum Taq polymerase (ThermoFisher Scientific). Cycling conditions were 95˚C for 5 minutes, followed by 50 cycles of (95˚C for 5 seconds, 60˚C for 30 seconds and 72˚C for 30 seconds). Standards for quantification were created by serial dilution of a 104-bp synthetic target equivalent to the bisulfite-converted locus.

Sample Loading and Digitization

The PCR and HRM master mixes were prepared to yield final working concentrations of 1.66 mM $(NH_4)_2SO_4$, 6.7 mM Tris pH 8.8, 2.7 mM $MgCl_2$, 1 mM β-mercaptoethanol, 300 nM primers (IDT, Table 2), 200 µM dNTPs (Thermofisher), 1X ROX (Thermofisher), 0.04 U/µL Platinum Taq DNA polymerase (Thermofisher), 1 mg/mL BSA (NEB), 0.01% Tween 20 (Sigma Aldrich), and 1X Evagreen (Biotium). This master mix was drawn into microcentrifuge tubing (Cole Parmer) using a syringe. Due to the desiccation, a negative pressure differential existed inside the microfluidic chip seal.

When the needle of the tubing punctured the seal, the sample was drawn into the wells. Partitioning fluid, consisting of 5 g Silicone oil and 1 g PDMS (10:1), was then pressurized through the channels. Due to surface tension, the fluid did not enter the wells, and served to isolate the reaction chambers and digitize the sample throughout the 4096 wells. During PCR, the partitioning fluid was pressurized at one end, and sealed at the other. Furthermore, the PDMS in the oil solidified over the course of the PCR reaction, producing a permanent barrier.

Digital PCR and Digital Melt

The chip was then placed on a flatbed thermal cycler (Proflex). Thermal contact was ensured by use of FC-40 oil between the glass slide and the heating surface. A PCR program then ran for 60 cycles of 95°C, T_A (where T_A is the annealing temperature for the DREAMing primers), and 72°C for 30 seconds each. The annealing temperature, which controls the amplification bias of the primers to methylated vs unmethylated targets as previously described[63], was optimized for reduced bias to provide more uniform amplification of heterogeneously-methylated epialleles (Figure 3.9). The T_A was 63°C for the $p14^{ARF}$ assay and 57°C for the *NDRG4* assay. Next, the chip was removed from the heater, disconnected from the tubing, and taken to the digital melt platform (Figure 3.2A). The chip was secured to a flatbed heater with tape. The wells were illuminated by an expanding blue LED array (Thorlabs). Wide field-of-view imaging captured the fluorescence of all 4096 wells simultaneously by use of a Sony ILCE with a 50mm lens (Canon), coupled to a green filter (Omega Optical). The chip underwent temperature ramping at a rate of 0.1°C/sec from 70°C to 95°C. Images were captured at 1 Hz with a

0.8” exposure. An unmethylated control was run before and after each serial dilution to verify the absence of contamination.

Image Processing and Data Analysis

After collection, the images were aligned to correct for any thermally induced movement via an open-source automated program, Automated Image Registration (AIR) [91]. The remainder of the analysis was performed with a custom-developed Matlab script (Figure 3.5). The user selects the four corners of the chip in order to generate a virtual mask outlining the expected well locations. Once generated, the virtual mask was mapped to the acquired image via a homography transformation to correct for the non-parallel relationship between the signal and imaging surfaces. Finally, well-by-well transformations were performed by locally optimizing the signal over a 5-by-5 pixel neighborhood. The overall image contained 4240 x 2832 pixels, yielding approximately 200 pixels/well.

Once well locations were determined, the virtual mask was propagated throughout all of the collected images and captured the signal intensity of the 200 pixels in each well. Fluorescence intensity values within a well at each time point were checked for outliers and then averaged. Time points were then sorted by temperature, and each signal within 0.3°C was further averaged. Finally, a low-pass and Savitzky-Golay filter was performed on each well to produce a melt curve. The negative derivative of this signal was taken, and then corresponding peak(s) determined the melt temperature of the amplicon in each well. Only the right-most peak is used for discernment in each well to avoid any potential signal from heteroduplex formation. Simple thermal calibration was performed by taking advantage of the DREAMing assay principles [63], namely a known background

population of unmethylated targets, which had a consistent melt temperature and could thus be used for inter-experimental alignment.

MSP/Methylight and ddPCR- MPS/MethyLight

All MethyLight assays were performed using 10X Master Mix to yield a final volume of 25 µl and final working concentrations of 16.6mM $(NH_4)_2SO_4$, 67mM Tris pH 8.8, 6.7mM $MgCl_2$ 10mM β-mercaptoethanol, 200µM of each deoxynucleotide triphosphate (dNTP) and 0.04 U/µl of Platinum Taq polymerase (ThermoFisher Scientific). Each assay was validated by serial dilution to create a percent methylated reference (PMR) standard curve ranging from 0.1% to 100% of bisulfite-converted methylated to unmethylated control genomic DNA (Promega). MethyLight assay validation results are provided in Figure 3.10.

The MSP/MethyLight assay [50] for *NDRG4* was performed with 300nM forward primer, 5'- GCG TAG AAG GCG GAA GTT AC -3', 300nM reverse primer, 5' – TAA ATT TAA CGA ATA TAA ACG CTC GAC C -3', spanning a 123-bp region (chr16:58,463,535-58,63,637), and 100nM probe, 5'- \56-FAM\CGG TTC GTT \ZEN\ CGG GAT TAG TTT TAG GTT CGG \3IABkFQ\ -3'. Cycling conditions were 95˚C for 5 minutes, followed by 50 cycles of (95˚C for 30 seconds, 60˚C for 30 seconds and 72˚C for 30 seconds) using a CFX96 Touch Real-time PCR Detection System (Bio-Rad) and analyzed using the accompanying stock software, CFX Manager.

The MethyLight and corresponding droplet digital assay for *CDKN2A* (p14ARF) was performed with 300nM forward primer, 5'- TTG TTT ATT TTT TCG TGA GTC GC -3', 300nM reverse primer, 5' – ACC CTC CGA ATT CGA CG -3', spanning a 95-bp

region (chr9:21,994,226-21,994,310), and 100nM probe, 5'- \56-FAM\ TAC GAC CCG \ZEN\ CCG CGA AT \3IABkFQ\ -3'. MethyLight cycling conditions were 95˚C for 5 minutes, followed by 50 cycles of (95˚C for 30 seconds, 60˚C for 30 seconds and 72˚C for 30 seconds). MethyLight was performed using a CFX96 Touch Real-time PCR Detection System (Bio-Rad) and analyzed using the accompanying stock software, CFX Manager.

For ddPCR, mastermix was prepared with Bio-Rad Supermix 1X according to Bio-Rad instructions. Mixed epiallelic targets were diluted to 40, 400, and 4000 copies per 20 uL, and background unmethylated targets were diluted to 2000000 copies per 20 uL. ddPCR was performed in for each dilution in duplicate, with and without the background DNA. Droplets were generated with the QX200 Droplet Generator (Bio-Rad), amplified in a 96-well plate (Bio-Rad) thermal cycler (Applied Biosystems), and detected via the QX200 Droplet Reader. Cycling conditions were 95ºC for 10 min, 40 cycles of (94ºC for 30 seconds, 60ºC for 1 minute), 98ºC for 10 min, at a ramp rate of 2ºC/second, as recommended by the manufacturer. Thresholding was performed across all reads by the proprietary Bio-Rad Software to obtain the copy number detected per reaction volume (20 uL) (Figure 3.8).

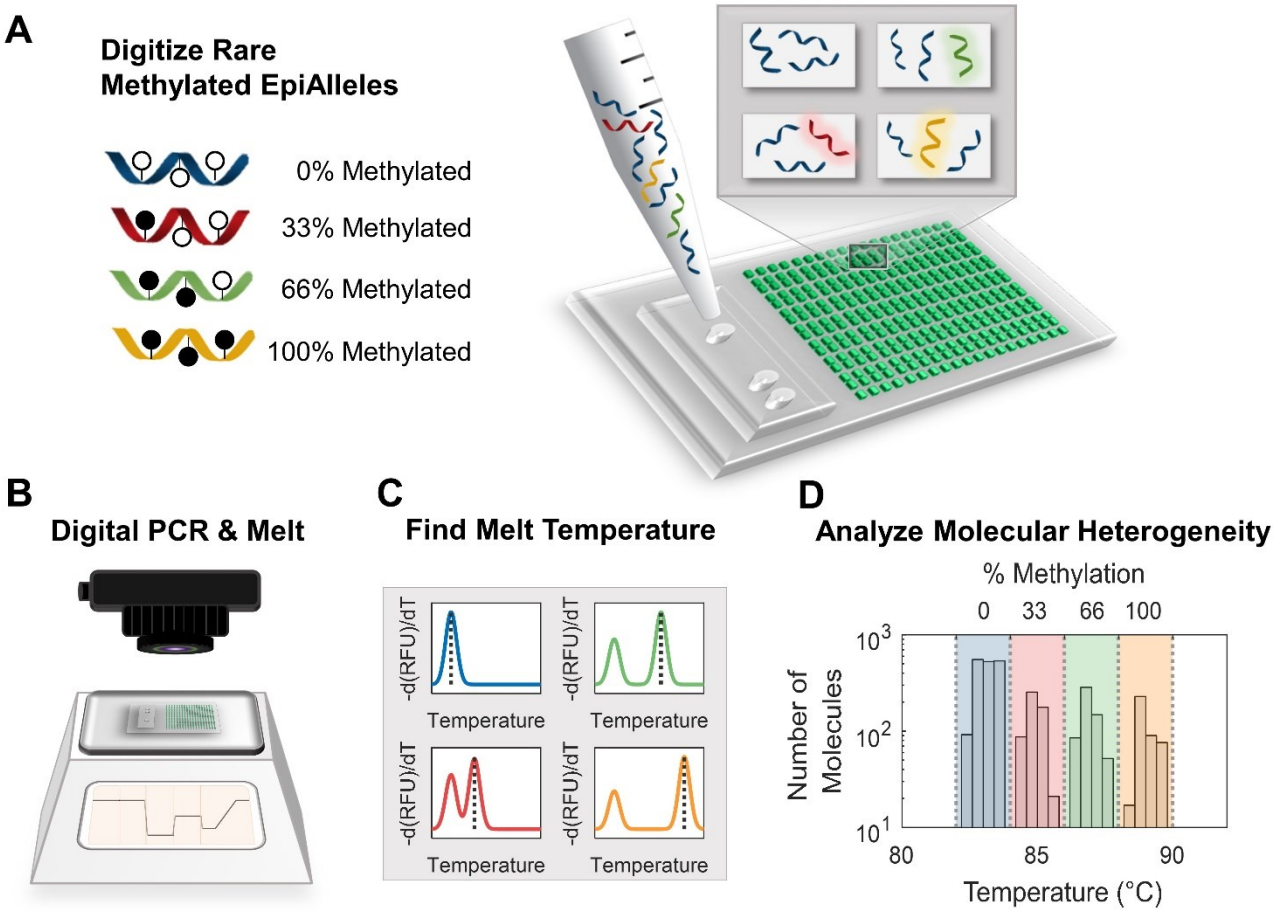

Figure 3.1. HYPER-Melt workflow.

(A) The reaction and target mixture, prepared on benchtop, is loaded into the microfluidic chip where rare methylated epialleles are digitized. (**B**) The chip is then placed on a flatbed heater to undergo PCR amplification followed by the Melt reaction, in which a MILC captures fluorescent images of the array during temperature ramping. (**C**) The images are analyzed to find the melt temperature, which corresponds to the initial template sequence. (**D**) A molecular heterogeneity histogram reveals different populations, which can be separated by thresholding and classified by methylation density, providing a quantitative

analysis of the molecular heterogeneity of the sample. This figure is reprinted with permission from reference [73].

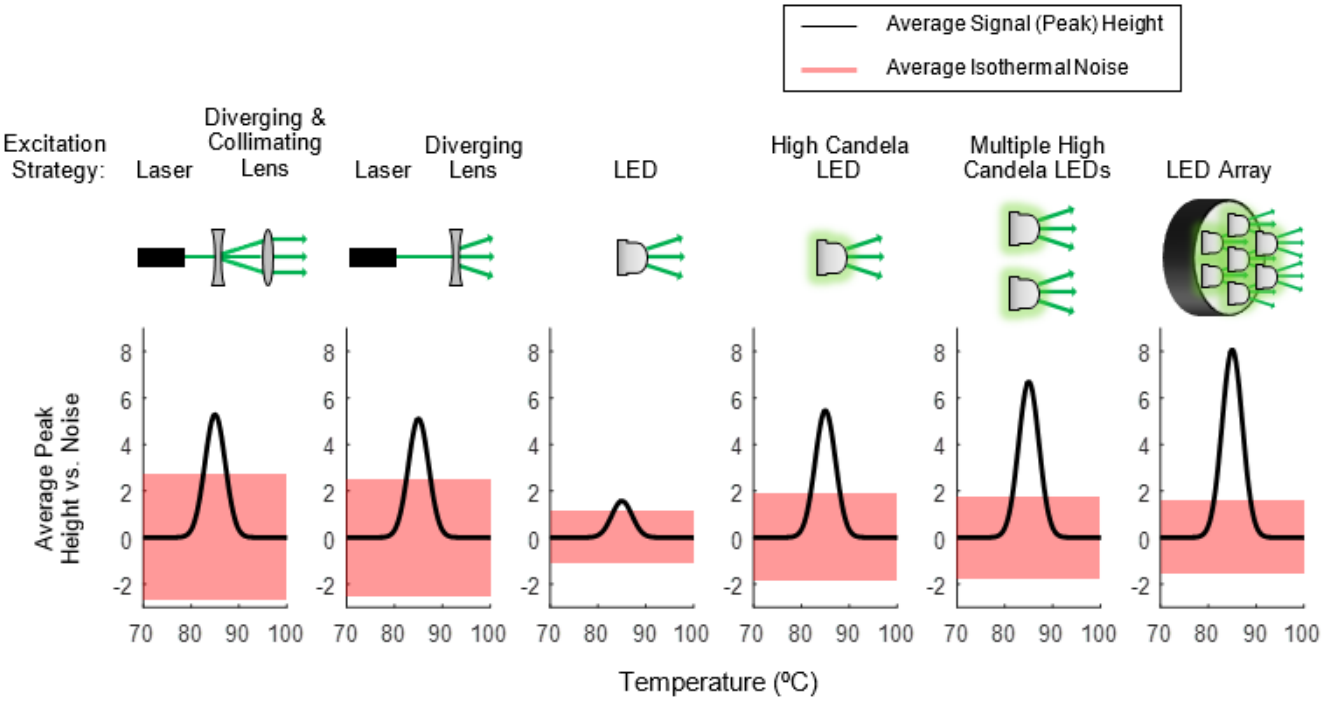

Figure 3.2. Illumination Optimization.

Several illumination strategies were tested in order to maximize the desired signal, i.e. the melt denaturation peak, and minimize isothermal noise. The signal was defined as the average peak height of positive wells throughout the chip. The noise was defined as the average standard deviation of brightness values within each temperature increment before the melt temperature. Counterintuitively, switching from a Laser to LED decreased the intra-temperature-increment noise observed during the melt reaction. The final design utilized an LED array. This figure is reprinted with permission from reference [73].

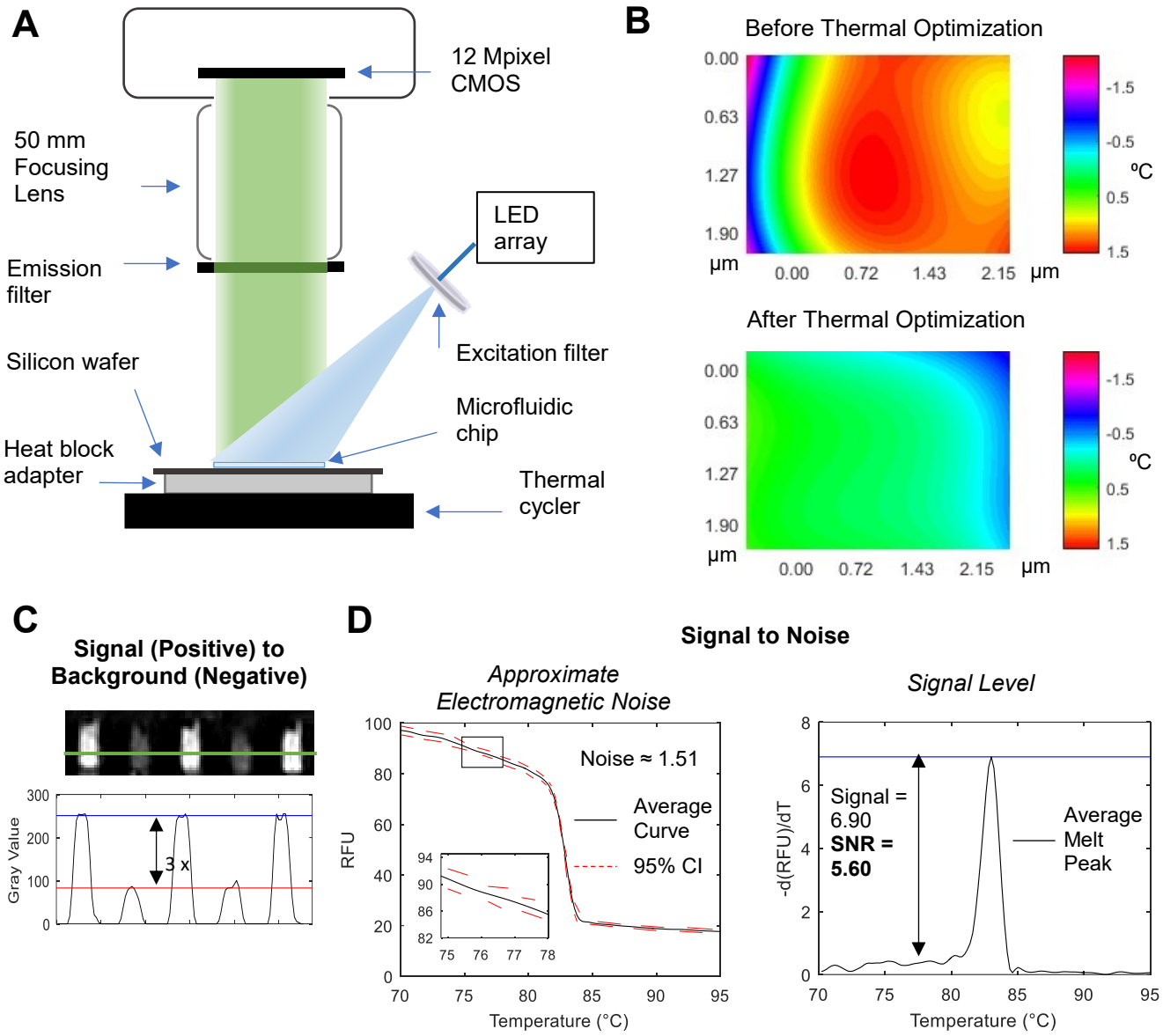

Figure 3.3. Digital Melt Platform

(A) The heating components consisted of a commercial thermal cycler with a 96-well plate to flatbed adapter and a silicon wafer, to which the microfluidic chip was secured. The chip was illuminated by an LED array and filter. Fluorescence detection occurred via a 12 Mpixel CMOS MIL camera coupled to a filter and focusing lens. (B) Melt temperature variation across the chip after loading and digitization with benchtop-amplified PCR

product of a single DNA target. The addition of thermally stabilizing layers and fabrication modification of a thicker glass slide greatly improved thermal stability. (C) The positive vs. negative signal was characterized by digitally amplifying the target on-chip. (D) The signal to noise characterization of the on-chip DREAMing reaction was assessed by comparing the average standard deviation of each temperature interval of the overall average melt curve to the overall average peak height of positive wells. This figure is reprinted with permission from reference [73].

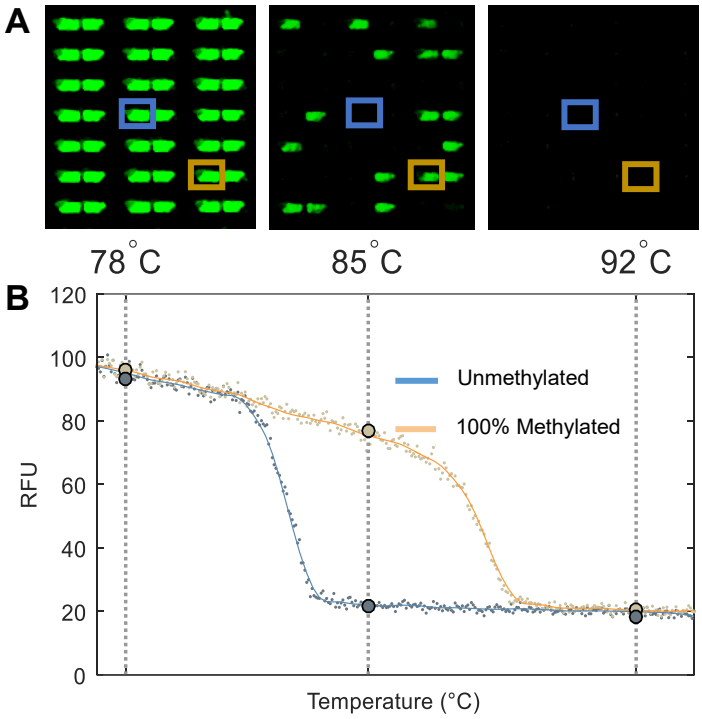

Figure 3.4. Melt curve acquisition and discrimination by melt temperature.

(A) Fluorescent images are acquired of the entire chip at each temperature interval to visualize denaturation of the amplicons (subset shown). (B) The fluorescence data of each well is filtered and plotted against temperature to produce a melt curve. The inflection point of the curve is defined as the melt temperature (T_m) of the template sequence. The T_m is then used to discriminate the methylation density of the original template epiallele. This figure is reprinted with permission from reference [73].

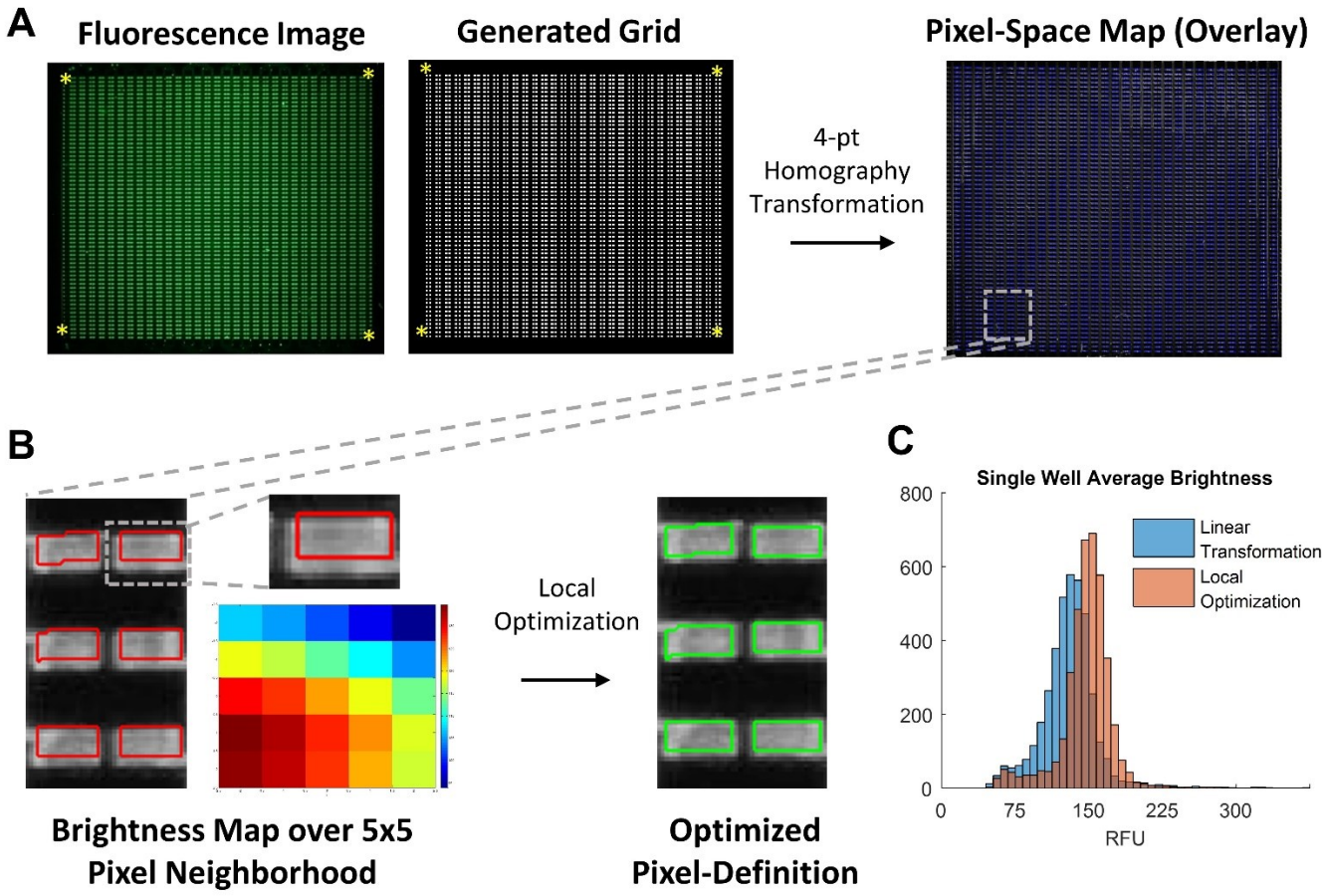

Figure 3.5. Pixel-Space Definition Mapping.

(A) The user selects four control points from the image acquired by the camera and the generated grid image based on the chip mask design which are used to compute the homography transformation of the grid to correct for linear misalignment between imaging and signaling planes. (B) Next, due to nonlinear nonuniformities in the chip, a local optimization of brightness over a 5-by-5 pixel neighborhood is performed to improve alignment. (C) The optimized grid captures more fluorescence information than native transformation. This figure is reprinted with permission from reference [73].

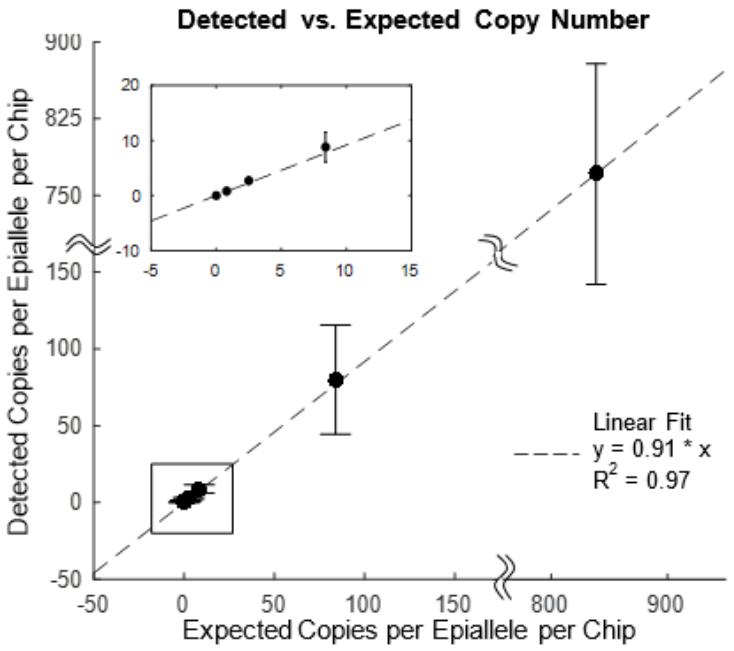

Expected Positive Copies	0	0.8	2.5	8.4	83.9	838.7
Detected Positive Copies	0 ± 0	0.7 ± 0.6	2.3 ± 0.6	7.7 ± 2.7	69.7 ± 35.6	669.3 ± 108.7

Figure 3.6. Detected vs. expected DNA copy number.

Mixed epialleles were diluted into a background of 2 million unmethylated templates. After amplification and HRM-based discrimination, the detected copy number of each epiallele were calculated according to a Poisson distribution. The average epiallelic detected copy number was compared to the expected. The array chip demonstrates linearity from ~1 to 1000 copies. This figure is reprinted with permission from reference [73].

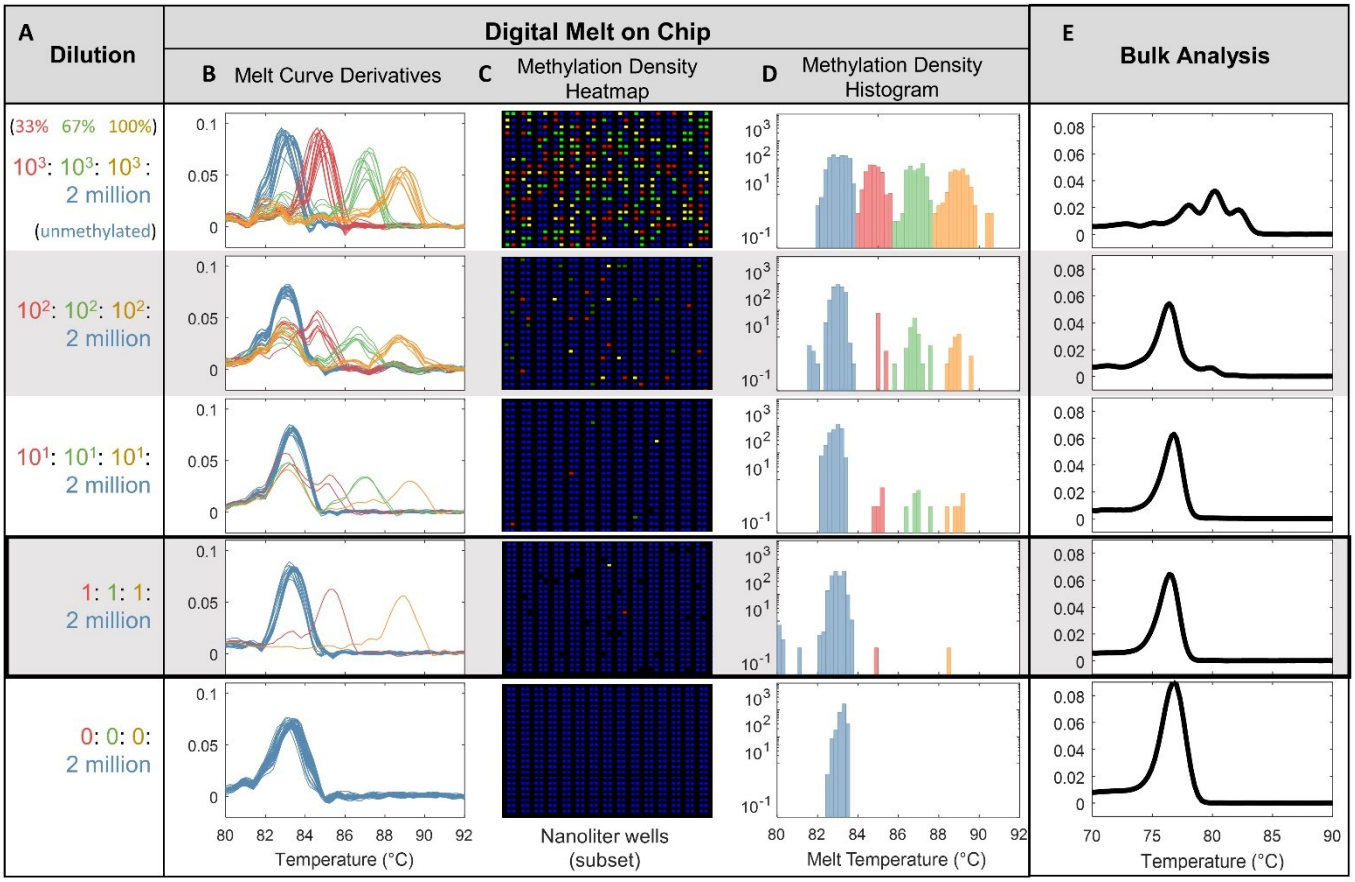

Figure 3.7. HYPER-Melt analysis.

(A) HYPER-Melt was used to analyze $p14^{ARF}$ synthetic sequences ranging in copy numbers of 0 to 1000 of each epiallelic species in 2 million unmethylated background molecules. (B) A subset of melt curve derivatives from each serial dilution, color-coded by melt temperature, demonstrate methylation-density-independent amplification of all species as well as single-copy sensitivity. (C) The digital heatmap reflects the methylation density of the template molecule in each well. (D) The populations of the four epiallelic species can be quantified and assessed upon inspection and thresholding of the DREAM histogram. (E) Corresponding bulk analysis validates amplification, but demonstrates

limited sensitivity due to the low-copy-number methylated peaks being eclipsed by the high background. This figure is reprinted with permission from reference [73].

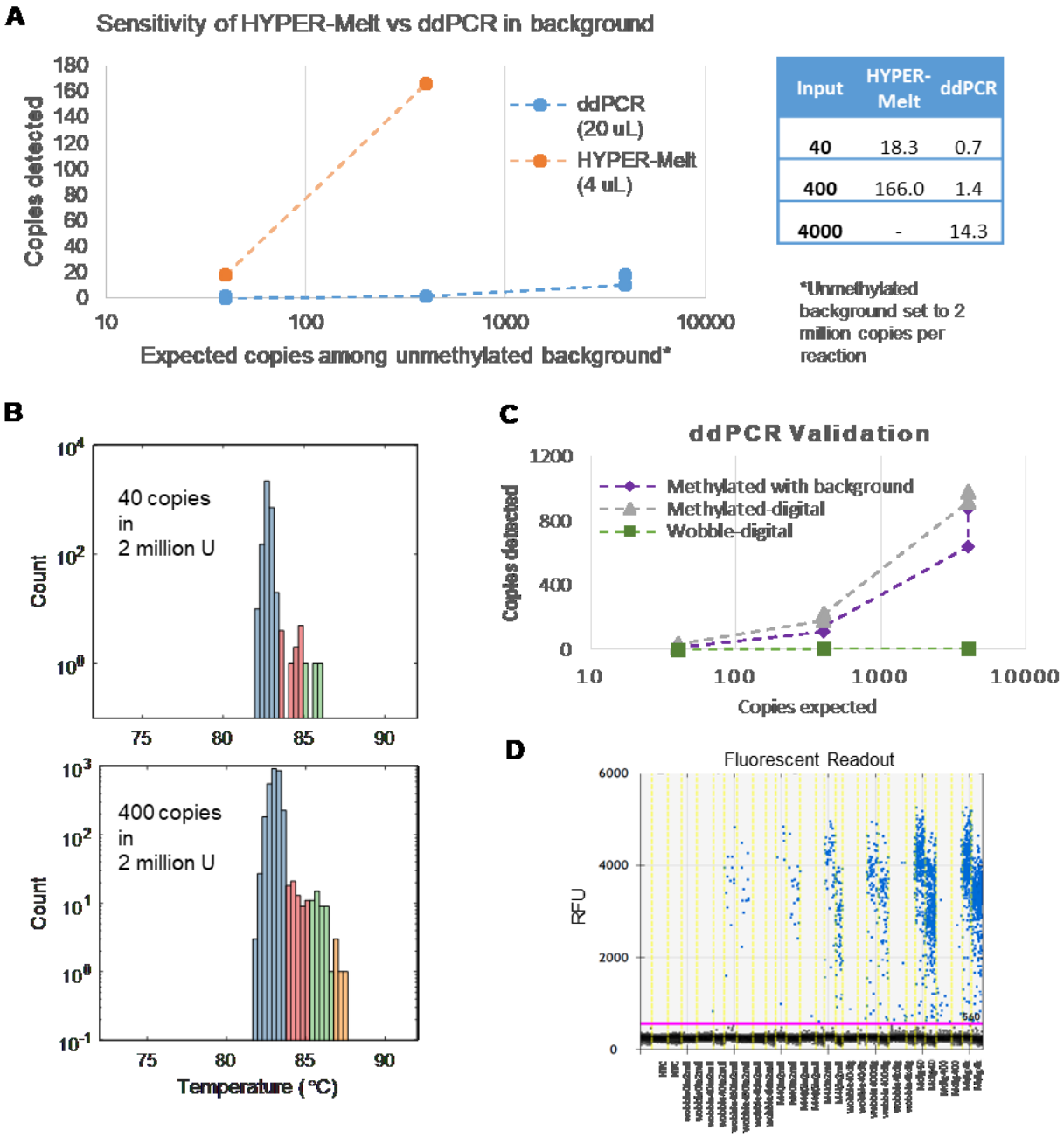

Figure 3.8. Comparison of HYPER-Melt with ddPCR.

To create an unbiased comparison between HYPER-Melt and other sensitive assays such as ddPCR, we designed synthetic targets with degenerate C/T bases in all CpG sites, representative of completely random methylation in the primer and target regions for

$p14^{ARF}$. HYPER-Melt was performed following the same protocol as before at target copy numbers of 40 and 400 per chip in a background of 2 million unmethylated DNA copies. MSP primers were designed for $p14^{ARF}$, and ddPCR was run for target copy numbers of 40, 400, and 4000 per run in a background of 2 million unmethylated. We were unable to perform the 4000-copy reaction in the chip because it exceeds the dynamic range. (A) HYPER-Melt detected ~25-120-fold more copies overall than ddPCR, which is expected due to the low probability of the presence of a fully methylated target in each reaction. Additionally, HYPER-Melt provides sequence information of each copy detected (B). (C) ddPCR was performed for fully methylated targets, both with and without background, to validate the MSP assay. (D) Fluorescent readout information from ddPCR. Each dot represents the fluorescence from a single droplet. This figure is reprinted with permission from reference [73].

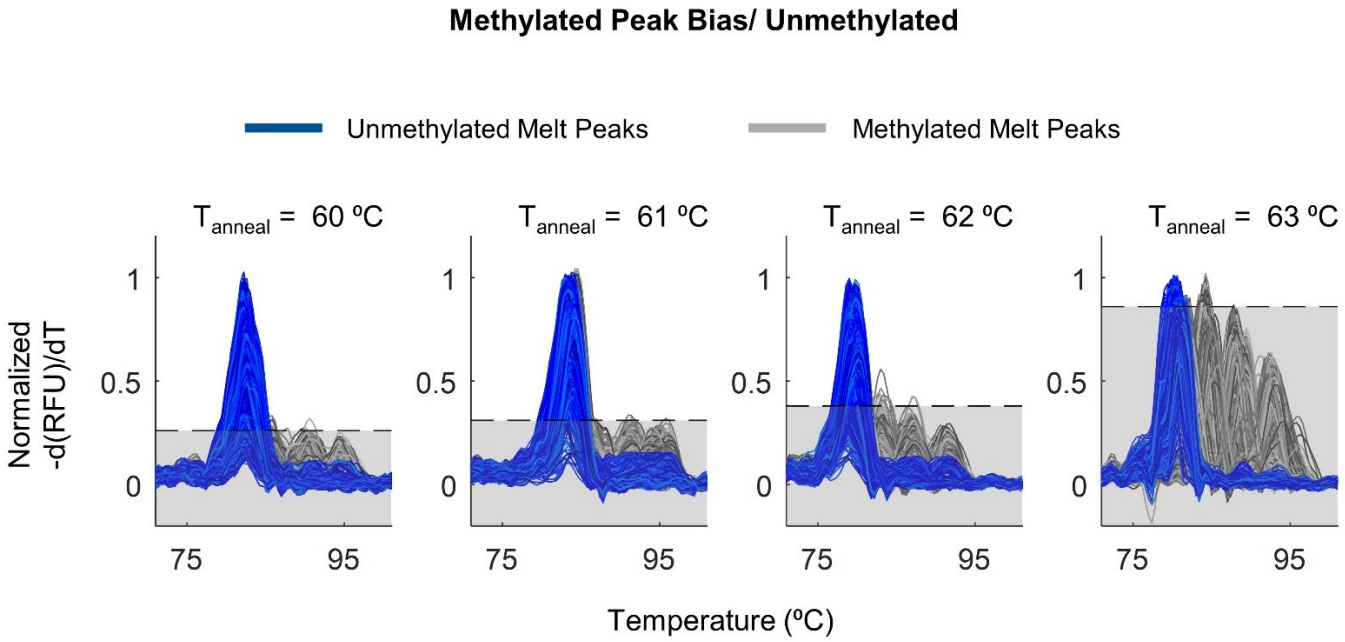

Figure 3.9. Annealing Temperature On-Chip Optimization.

Optimization of the methylation bias, defined here as the relative peak height ratio between methylated and unmethylated targets, was performed by running DREAMing on-chip at multiple annealing temperatures. The optimal bias that still amplified unmethylated DNA occurred at 63 ºC. This figure is reprinted with permission from reference [73].

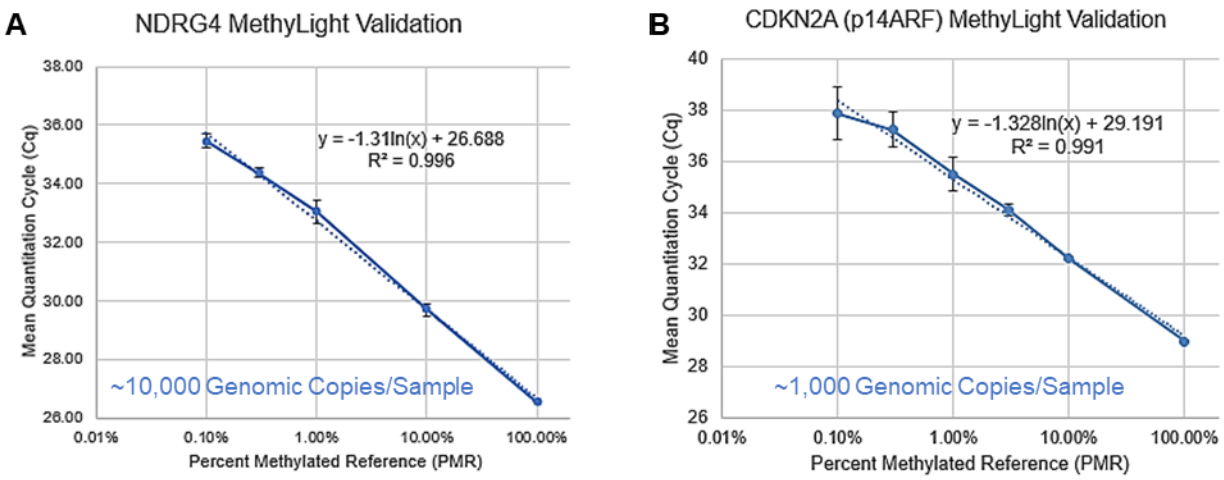

Figure 3.10. Validation of MSP Assay

(A) Validation of *NDRG4* MSP/MethyLight assay. (B) Validation of *CDKN2A* MSP/MethyLight assay.

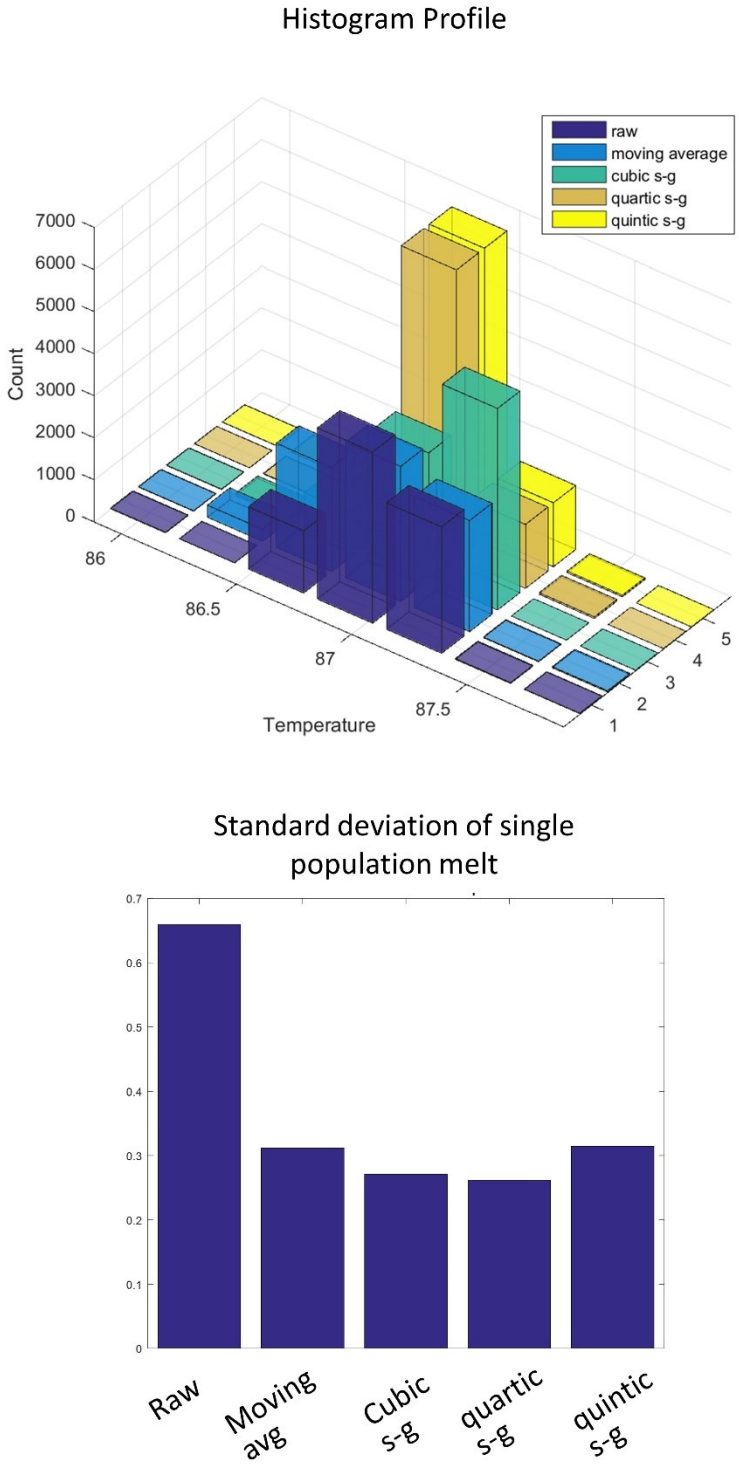

Figure 3.11. Data Processing Filter Optimization

Several filters were analyzed for reduction of noise in the optical signal. Each filter was assessed for (A) maintaining the integrity of the raw data and (B) reducing the melt temperature deviation within a single population on the device. Overall, a quartic savitsky-golay filter proved the best suited for HYPER-Melt.

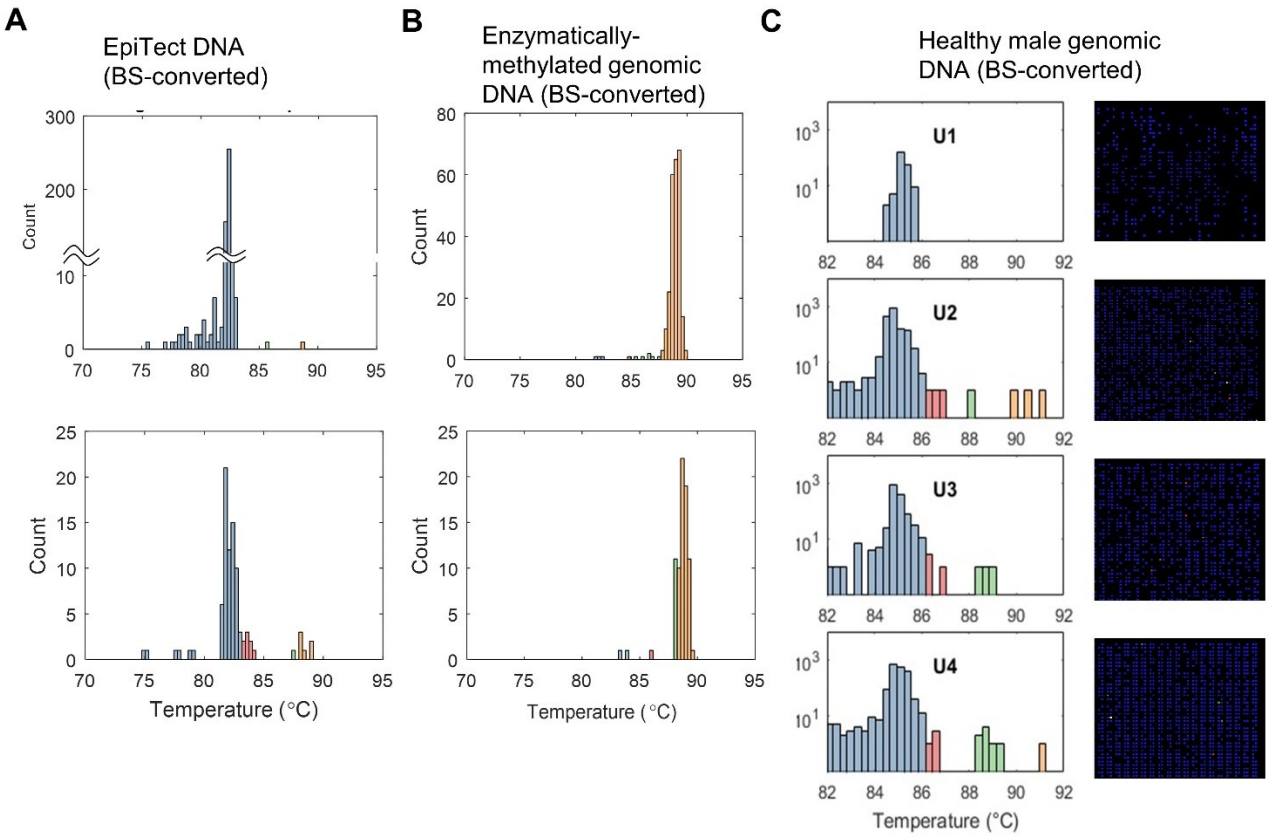

Figure 3.12. Genomic Validation of HYPER-Melt Platform

(A) HYPER-Melt analysis of bisulfite-converted EpiTect DNA (Qiagen). Bisulfite conversions were performed using EZ DNA Methylation-Lightning Kit (Zymo). (B) HYPER-Melt analysis of enzymatically-methylated (Sigma-Aldrich), bisulfite-converted DNA. (C) HYPER-Melt analysis of human male genomic DNA from random donors (Promega). This figure is reprinted with permission from reference [73].

$p14^{ARF}$	**Unmethylated (0/13)**	TGTTTTTGGTGTTGTTTATTTTTTTGTGAGTTGTGGGATGTGAATTATGAA AATTTTTATTTGTGGTGGGTTGTATGTGTGTTGAATTTGGAGGGTTATTA AGAATTTGTGTATTATGT
	4/13 Methylated	**CGTTTTTGGCGTTGTTTATTTTTTTGTGAGTCGTGGGATGTGAATTACGA AAATTTTTATTTGTGGTGGGTCGTATGTGTGTCGAATTTGGAGGGTTATT AAGAATTTGCGTATTATGT**
	9/13 Methylated	CGTTTTTGGCGTTGTTTATTTTTTCGTGAGTCGTGGGATGTGAATTACGA AAATTTTTATTCGTGGCGGGTCGTATGCGTGTCGAATTCGGAGGGTTAT TAAGAATTTGCGTATTATGT
	13/13 Methylated	**CGTTTTTGGCGTTGTTTATTTTTTCGTGAGTCGCGGGATGTGAATTACGA AAATTTTTATTCGCGGCGGGTCGTACGCGCGTCGAATTCGGAGGGTTAT TAAGAATTTGCGTATTATGT**
	Forward Primer	CGTTTTTGGCGTTGTTTATTTT
	Reverse Primer	**ACATAATACGCAAATTCTTAATAACCCTC**
NDRG4	**Forward Primer**	TTCGTTCGTTTATCGGGTATTTTAGT
	Reverse Primer	**CGATACCGAACCTAAAACTAATC**

Table 2. Assay primers and synthetic targets

The $p14^{ARF}$ gene sequence is shown above. Primers were designed previously to achieve methylation-preferred amplification. The region within the primers contains 13 possible methylation sites, of which these 4 were chosen for demonstration of HIPR-Melt analysis. NDRG4 primers sequences are shown for amplification of cell-free DNA from liquid biopsies.

Chapter 4

HIGHLY EFFICIENT DIGITAL MICROFLUIDICS BY PASSIVE GEOMETRIC IMMOBILIZATION

Disparity in sample-to-analysis volumes

Liquid biopsies contain a treasure of genetic and epigenetic biomarkers that contain information for the detection and monitoring of human disease. DNA methylation is an epigenetic modification that is critical to determining cellular phenotype and often becomes altered in many disease states. In cancer, aberrant DNA methylation contributes to carcinogenesis and can profoundly affect tumor evolution, metastatic potential, and resistance to therapeutic intervention. However, current technologies are not well-suited for quantitative assessment of DNA methylation heterogeneity, especially in challenging samples such as liquid biopsies with low DNA input and high background. We present a multilayer microfluidic device for quantitative analysis of DNA methylation by digital PCR and high resolution melt (HRM). The multilayer design facilitates high-density array digitization aimed at maximizing sample loading efficiency. The platform achieves highly parallelized digital PCR-HRM-based discrimination of rare heterogeneous DNA

methylation as low as 0.0001% methylated/unmethylated molecules of a classic tumor suppressor gene, *CDKN2A* ($p14^{ARF}$).

The HYPER-Melt platform offers a novel method of highly sensitive analysis and quantification of methylation heterogeneity suitable for detection of rare biomarkers in liquid biopsies [73]. However, while promising, this method, like most array-based techniques, analyzes a small percentage of the consumed sample, thereby discarding many of the precious disease-derived molecules and their presumed clinical insight [70], [100], [101]. Recently, digital technologies have been used to demonstrate that as few as 7 copies/mL of mutated *PIK3CA* can indicate therapeutic resistance in breast cancer [102], and 2 copies/2 mL of hypermethylated vimentin is present in early stage colon cancer [56], illustrating the scarcity of these biomarkers and the need for thorough inspection of plasma samples.

A limited number of existing designs have attempted to address the issue of sample throughput, but do not demonstrate performance at high temperature [103], [104], cannot guarantee complete digitization [105], or have limited imaging capacity [104]. Therefore, there exists a need for a microfluidic device capable of highly efficient sample compartmentalization and detection of rare molecules.

In this study, we present a multilayer microfluidic device for efficient trapping and parallelized DNA methylation analysis of single molecules in picoliter-sized chambers. The multilayer design facilitates efficient digitization of DNA molecules into 13,000 wells. We demonstrate the utility of this digital PCR- high resolution melt (HRM) platform through discrimination of partially and fully methylated epialleles of a tumor suppressor

gene, *CDKN2A* (*p14*^{ARF}) amongst a high background of unmethylated DNA. The ultrahigh sensitivity of this platform provides a means for quantitative assessment of DNA methylation heterogeneity of rare molecules such as those found in liquid biopsies.

Multilayer geometric manipulation

To achieve high-efficiency and high-density methylation profiling, we developed a multilayer microfluidic chip for digitization and interrogation of individual DNA sequences. The device consists of two PDMS pattern layers oriented such that the features are in contact. The lower PDMS layer, containing 13,000 750 pL-sized chambers or wells, sits below the channel layer, overlapping at the inlets to each chamber (Figure 4.1A). Two glass slides sandwich the device, and PDMS adapters provide the loading interface (Figure 4.1B). The reaction mix rapidly enters the desiccated device through the channels and fills the wells (Figure 4.1C). Next, a partitioning oil flows through the evacuated channels, thus isolating and digitizing the individual molecules.

Most array-based technologies suffer from sample loss during loading or digitization processes [70], [100], [101]. Previously, our device design comprised of parallelized straight channels with perpendicular inlet orientation [73]. During vacuum-assisted loading, the fluid rapidly filled the channels before saturating the wells, disqualifying approximately 89% of the sample for analysis. To minimize loss due to channel bypassing, we sought to implement a design that retards flow through the channels while maintaining or increasing the fill velocity of each well.

The multilayer design promotes efficient loading through two primary mechanisms. First, the curved channel design directs fluid to flow towards the walls of the channels where the inclined inlets for the chambers are located. The presented curved, single-channel design constantly redirects flow, increasing flow resistance in the direction of the channel. Second, the ratio of the well height (h_w) to the channel height (h_c) can be tuned to adjust the relative force of the vacuum in the direction of the wells ($F_{vacuum,w}$) with respect to the channel ($F_{vacuum,c}$).

Modeling and simulation of 2-dimensional device geometries

To model the effects of the channel and inlet device geometries on the flow profile, two-dimensional multiphase fluid simulations of the sample loading into different channel and inlet geometries were conducted with COMSOL Multiphysics. First, we compared the curved channel to a straight channel under conditions simulating vacuum-assisted loading. Initially, the inlet of the main channel was filled with water (aqueous phase) and the rest of the geometry was occupied by low pressure air (gas phase). The modeled curved channel is a 180° semi-circle. Both channels were 10 mm in overall length and 0.1 mm wide.

Two physical models were involved in the models: First, the laminar two-phase flow, level set model was used to track the interface between two immiscible fluids. It solved Navier-Stokes equations for the conservation of momentum and a continuity equation for the conservation of mass. The interface position was tracked by solving a transport equation for the level-set function in COMSOL:

$$\rho\frac{\partial \boldsymbol{u}}{\partial t} + \rho(\boldsymbol{u}\cdot\nabla)\boldsymbol{u} = \nabla\cdot[-\rho\boldsymbol{I} + \mu(\nabla\mathbf{u} + \nabla\mathbf{u})^T] + \rho\boldsymbol{g} + \boldsymbol{F}_{st} + \boldsymbol{F}$$

$$\nabla\cdot\boldsymbol{u} = 0$$

$$\frac{\partial\phi}{\partial t} + \boldsymbol{u}\cdot\nabla\phi = \gamma\nabla\cdot\left[\epsilon_{ls}\nabla\phi - \phi(1-\phi)\frac{\nabla\phi}{|\nabla\phi|}\right], \phi = \text{phils}$$

Second was the two-phase Darcy's law model which simulated the air permeation to the interstices in a porous PDMS substrate medium surrounding the chamber. It solved Darcy's law for the total pressure and the transport of the fluid content for one fluid phase in COMSOL:

$$\frac{\partial\rho\epsilon_p}{\partial t} + \nabla\cdot(\rho\boldsymbol{u}) = 0$$

$$\frac{\partial c_1\epsilon_p}{\partial t} + \nabla\cdot(c_1\boldsymbol{u}) = \nabla\cdot(D_c\nabla\mathrm{c}_1)$$

The simulation results showed an approximately 5-fold retardation in travel through the curved channel with respect to the straight channel over the 10 mm path (Figure 4.2A). Furthermore, the curved channel demonstrates a more parabolic velocity profile than the straight channel (Figure 4.2B). Although the geometry was simplified for the purpose of the model, the relationship is expected to be maintained when scaled to larger volumes. This result matches our experimental observation that curved channels experience slower flow rates.

Next, we simulated the aqueous sample loading into the chambers at both perpendicular and inclined inlet geometries (Figure 4.2C,D). According to the model, sample loading from the channel into the chamber took 0.27 seconds and 0.17 seconds for 90° and 45° inlets, respectively. The relative loading speeds match our observation that an angled inlet loaded faster than a perpendicular inlet. However, in the on-chip experiment

we observed that loading could take as long as 5-15 seconds. This deviation can be attributed to the driving force variation in the sample digitization process. Specifically, absolute pressure within the air phase of the chip increases as the sample loads, resulting in a reduction in the pressure differential driving the liquid as it moves from the sample inlet to outlet. Thus, it takes a shorter time to fill a chamber close to the inlet when compared to those located near the outlet. Nonetheless, the essential features of the sample loading and digitization presented by the simulation were in good agreement with our experimental observations.

Loading efficiency in 2D vs. 3D device

Experimentally, we sought to quantitatively assess the loading efficiency of the multilayer curved channel device ($h_w = 2*h_c$) as compared to the identical pattern in a single layer ($h_w = h_c$). Images were acquired of each device during loading. A single, fixed well was chosen for the time course study, beginning at the point the liquid first passes the well inlet. At each subsequent time point, the filled area of the well was compared to the volume of fluid that had continued along the channel, which we termed the "waste volume" (Figure 4.3A). The single layer device had a waste volume of 0.93 µL, 12% of the input volume (8 µL), whereas the multilayer produced only 0.34 µL, 4% (Figure 4.3B). Furthermore, the multilayer device filled each well ~3 times faster than the single layer, resulting in significantly higher loading efficiency of the sample.

The multilayer architecture also offers several advantages for partitioning and assay performance. The device utilizes a vertical compartmentalization strategy that complements the densities of the entrapped materials, namely the reaction fluid ($\rho_{fl} \approx 1$ g/mL), the partitioning oil (100 cst silicone oil [Sigma-Aldrich], $\rho_{oil} = 0.967$ g/mL), and air ($\rho_{air} = 0.001$ g/mL). Since $\rho_{fl} > \rho_{oil} >> \rho_{air}$, the partitioning oil drives any remaining reaction fluid from the channels down into the wells. Air, which notoriously prevents successful high-temperature reactions in enclosed devices, rises up to the channels, and is ejected by the partitioning oil (Figure 4.4). The environment is thus robust to amplification via high temperature assays such as PCR.

Reducing PDMS distortion and misalignment

Despite the advantages of the multilayer device, achieving reliable and repeatable fabrication was nontrivial. PDMS distortion with respect to its mold is a well-known challenge in multilayer soft lithography. Several attempts have been made to address the issue, namely by characterizing the distortion ratio [106], developing intricate fabrication techniques [107], and including tolerances into the design [108]. The presented multilayer design requires strict alignment of two peeled PDMS layers, which eliminates simple scaling as an option. In order to maintain high efficiency in loading and a high-density array footprint, large error tolerances were also not a viable option. Therefore, we investigated the relationship between distortion and PDMS height.

PDMS patterns of various heights were aligned and compared to the pattern mask using a laser microscope (Keyence VK-X100) (Figure 4.5A). For both mold heights, we observed a clear trend that smaller PDMS heights led to more predictable and less overall distortion (Figure 4.5B). By reducing the PDMS height to 26 μm, the distortion could be reduced to ≈0.32%, with a standard deviation of 0.015%. To achieve consistent results across layers and thereby minimize misalignment, an ultra-thin soft lithography fabrication technique was implemented (Figure 4.6). This ultra-thin technique is simple and obviates the need for any additional materials during fabrication. The evaporation potential is minimized by reducing the volume of porous hydrogel above the wells. Although alignment of the two layers requires a trained user, misalignment can be effectively reduced by minimizing the PDMS distortion from the mold.

Highly efficient detection of DNA methylation

To demonstrate the overall detection efficiency of the device, fixed amounts of synthetic DNA representative of fully methylated *CDKN2A* ($p14^{ARF}$), a well-established methylation biomarker for various cancer types [109], were digitized on the device. 8 μL of reaction mix were prepared containing a serial dilution of methylated $p14^{ARF}$ from ≈1000 to 100 copies. Fluorescent images were acquired after PCR amplification to quantify the number of detected methylated targets on the multilayer device (Figure 4.7A). The absolute copy number detected closely matched the expected amount loaded into the chip for each dilution.

The results demonstrate an ultimate detection efficiency of 70-80%, and detection of as few as 100 copies in 8 μL (Figure 4.7A). The reference channel was used to calculate the DNA concentration from the filled wells. The results demonstrate the high accuracy of the digital system at 93% (Figure 4.7B). The 7% loss is considered inherent to the system, and may occur due to sample preparation or the material properties of the device. Therefore, the average loading efficiency of the multilayer device is 80% (Figure 4.7C), which is 7 times higher than our previous work.

The high detection efficiency of this system qualifies it as a suitable method for detection of rare molecules in liquid biopsies. The reported average detection efficiency of 73% includes all potential sources of loss or variability. No system can be expected to be 100% efficient, as single copies of DNA can be lost in preparation steps, pipetting, freeze-thaw cycle, etc. Nevertheless, these improvements on loading and detection efficiency are important steps in advancing the clinical utility of this digital melt platform.

Epiallelic discrimination by digital melt

A key benefit of the HYPER-Melt platform is the ability to not only detect and enumerate target molecules, but also to enable genotyping of a target locus. As shown previously [63], in the case of DNA methylation, HRM can be used to readily determine the methylation density of each detected epiallele. We used this paradigm to demonstrate epiallelic discrimination in the present device by loading and digitizing samples containing synthetic oligonucleotide targets representative of bisulfite-converted sequences of

heterogeneously-methylated $p14^{ARF}$ epialleles at methylation densities of 33%, 67% and 100%, as well as an unmethylated (0%) population representing background DNA from ostensibly healthy, noncancerous cells.

Following amplification, the device was taken to the digital melt platform for parallelized melt curve acquisition. The negative derivative of the curve was taken to determine the melt temperature ("peak") of each amplicon. Amplification and HRM of the unmethylated control DNA at a concentration of 500 copies/nL, or 4 million copies resulted in an even distribution of positive wells containing a homogenous population of amplicons exhibiting melt centered at 83˚C (Figure 4.8A). Next, 400 copies of each methylated epiallele were digitized amongst the 8 million copy background. The melt temperature was calculated for each amplicon, and the corresponding methylation density was distinguished by thresholding. A methylation heatmap was then generated to provide a quantitative metric of the methylation heterogeneity of the sample (Figure 4.8B). Representative traces of each epiallelic population demonstrate the high sensitivity of this digital melt platform, and a sequence resolution of ≈4 CpG sites.

The ability to perform HRM-based discrimination enables rare and heterogeneous population analysis in an all-in-one platform, for which this is no current commercially available alternative. The impact of methylation heterogeneity in cancer and development is only just beginning to be elucidated. Several models have predicted that differential methylation occurs very early in carcinogenesis [29], [110]. This platform provides a simple, low-cost tool for quantification of rare DNA methylation heterogeneity.

In conclusion, we presented a multilayer microfluidic device that achieves efficient and highly sensitive detection and discrimination of DNA methylation heterogeneity of rare molecular populations. The curved channels and multilayer architecture improved loading efficiency up to 7x more than our previous design. The digital melt platform provides a rapid and facile technique for parallelized sequence interrogation at the single-copy level, allowing a comprehensive analysis of DNA methylation heterogeneity, especially in challenging samples such as liquid biopsies. We hope this technology can be applied to potentially improve sensitivity in cancer detection and therapeutic monitoring, and to provide insight into molecular mechanisms of tumor evolution.

Methods

Device Fabrication

Molds were fabricated with SU-8 photoresist (MicroChem) via standard photolithography. Silicon wafers were dehydrated for at least 4 hours at 200°C, then oxygen-plasma treated at 80 W for 1 minute (Technics PE-IIA). For the well layer, SU-8 3050 was spin-coated at 1800 rpm for 1 min, soft-baked at 95°C for 27 min, and exposed at 175 J/cm^2. For the channel layer, SU-8 3025 was spin-coated at 1800 rpm for 1 min, soft-baked at 95°C for 14 min, and exposed at 150 J/cm^2. Both molds were then baked at 95°C for 5 min, developed with SU-8 developer (MicroChem), and baked at 200°C for 1 hr.

PDMS devices were fabricated with an adapted ultra-thin soft lithography technique (Fig. S1). PDMS (Ellsworth) at a ratio of 15:1 elastomer base to curing agent

was spin-coated on the well and channel pattern layers at 700 and 900 rpm respectively. A sacrificial layer of 6:1 PDMS was spin-coated on a blank wafer at 100 rpm. All were baked for 6 min at 80°C. The sacrificial layer was then removed, placed on the pattern layer, and temporarily bonded by baking at 80°C for 6 min. Both joint layers were then removed from the mold. The well layer was bonded to the glass slide by oxygen-plasma bonding at 80 W for 1 min. Next the wells and channel layers were oxygen- plasma treated, aligned, and bonded. Finally, the sacrificial layer was removed, and coverglass and adapters were oxygen-plasma bonded to the top surface.

Modeling and Simulation

Two-dimensional multiphase fluid simulations of the sample loading into a single side chamber were conducted with a CFD package (COMSOL Multiphysics® v. 5.2. COMSOL AB, Stockholm, Sweden). The model comprised of a laminar two-phase flow level set and two-phase Darcy's law models. Additional parameters and a detailed model description are given in the supplementary information (Table 3).The geometric parameters, chamber inlet angle and channel curvature, were varied to assess loading speed of a single well and fluid velocity along the channel (Fig. S2).

Digital PCR and Melt

The reaction mix was prepared off-chip to yield final working concentrations of 1.66 mM $(NH_4)_2SO_4$, 6.7 mM Tris pH 8.8, 2.7 mM $MgCl_2$, 1 mM β- mercaptoethanol, 300 nM primers (IDT), 200 µM dNTPs (Thermofisher Scientific), 1X ROX (Thermofisher Scientific), 1.2 U/µL Platinum Taq DNA polymerase (Thermofisher Scientific), 1 mg/mL BSA (NEB), 0.01% Tween 20 (Sigma Aldrich), and 1X Evagreen (Biotium). The device

was sealed with adhesive and desiccated for a minimum of 2 hours to produce an internal vacuum. Upon puncturing the inlet, the 8 μL of reaction mix was loaded into the device. Next, a partitioning oil, comprised of 5 g of 100 cst silicon oil and 1 g of 10:1 PDMS was pressurized through the channels to digitize the chambers. The device was placed on a flatbed heater (ThermoFisher Scientific) to undergo dPCR (5 min at 95°C, followed by 60 cycles of 30 s at 95°C, 30 s at 61°C, and 30 s at 72°C). Digital melt curves were acquired on our previously described digital melt platform[73], in which fluorescent images were captured by a Sony ILCE MILC at 1 s intervals during a thermal ramping at 0.1 K/s.

Imaging

End-point fluorescent images were captured by a Typhoon Scanner (ge Amersham). Two channels were detected: excitation and emission of 488 nm and 526 nm for the Evagreen signal as well as 532 nm and 610 nm for the ROX reference signal. Post-processing of the images was performed in Matlab. RGB fluorescent images from melt acquisition were converted to grayscale. A binary mask image was aligned with the reference image to identify the pixel-space definition of each well following our previously outlined procedure[73]. Positive wells were identified by thresholding of the Evagreen signal of each well within its neighborhood.

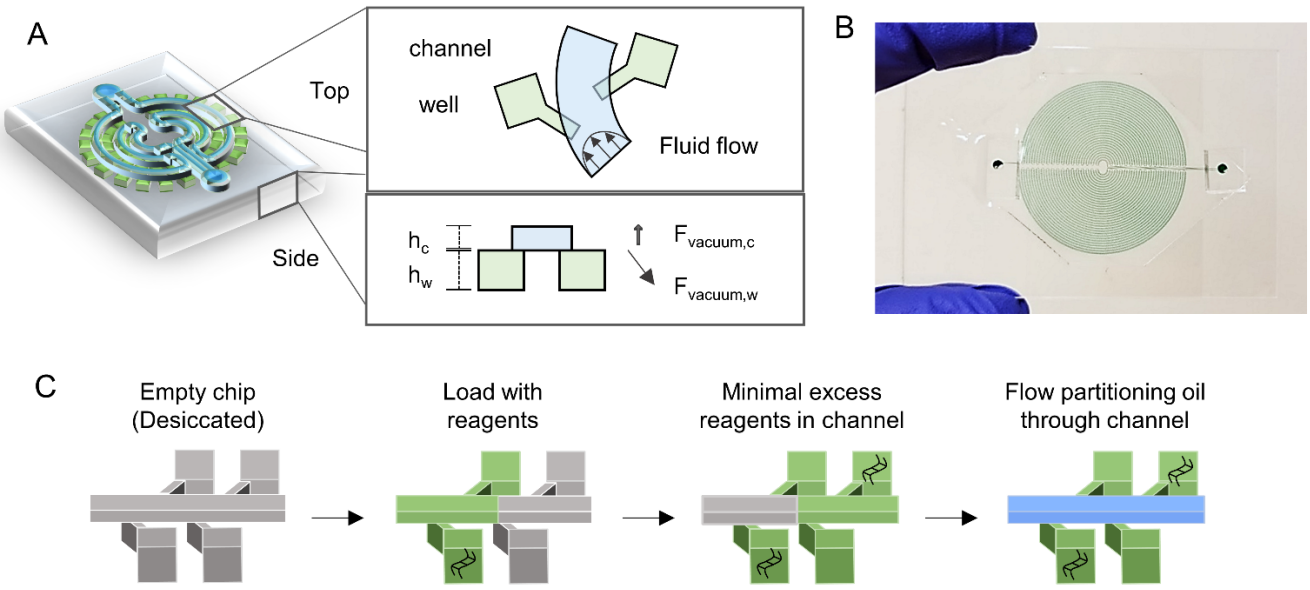

Figure 4.1. Multilayer Device Geometry

(A) The device consists of 2 PDMS layers sandwiched between glass slides. The curved channel sits above the wells. (B) The device is fully loaded with dye from a single inlet and semi-circle bifurcation. (C) Reagents are loaded into a vacuumed device, filling the wells. Oil is pressurized through the channel for partitioning and to eject excess air. This figure is reprinted with permission from reference [111].

	Channel-chamber with straight conjunction	Channel-chamber with 45° conjunction	Straight main channel	180° curved main channel
Geometry	Channel: w=100µm, h=50µm. Chamber: w=h=80µm	Channel: w=100µm, h=50µm. Chamber: w=h=80µm	Channel: w=20mm, h = 0.1mm	Channel: l=20mm, h = 0.1mm, d_1 =6.42mm, d_2=6.32mm
Physical model 1	Laminar Two-Phase Flow, Level Set	Laminar Two-Phase Flow, Level Set	Laminar Two-Phase Flow, Level Set	Laminar Two-Phase Flow, Level Set
Fluid properties	Fluid 1: air. Fluid 2: water. T=293.15K, built-in density and dynamic viscosity	Fluid 1: air. Fluid 2: water. T=293.15K, built-in density and dynamic viscosity	Fluid 1: air. Fluid 2: water. T=293.15K, built-in density and dynamic viscosity	Fluid 1: air. Fluid 2: water. T=293.15K, built-in density and dynamic viscosity
Inlet condition	Laminar inflow V=0.05m/s	Laminar inflow V=0.05m/s	Laminar inflow V=0.001m/s	Laminar inflow V=0.001m/s
Outlet condition	Pressure P_0= 0, Suppress backflow	Pressure P_0= 0, Suppress backflow	Pressure P_0= 0, Suppress backflow	Pressure P_0= 0, Suppress backflow
Wall condition	Wetted wall: θ_w=90°, β=5µm	Wetted wall: θ_w=90°, β=5µm	No slip	No slip
Physical model 2	Two-phase Darcy's law	Two-phase Darcy's law	N/A	N/A
Porous media properties	D_c=500µm^2/s, K_{r1}=0.2, K_{r2}= 0.01	D_c=500µm^2/s, K_{r1}=0.2, K_{r2}= 0.01	N/A	N/A
Inlet condition	Normal inflow V=0.5mm/s	Normal inflow V=0.5mm/s	N/A	N/A
Outlet condition	Pressure P_2= -0.01atm	Pressure P_2= -0.01atm	N/A	N/A
Mesh	1849 domain & 207 boundary elements	2144 domain & 219 boundary elements	7256 domain & 1458 boundary elements	3046 domain & 1010 boundary elements
Time stepping method	generalized-alpha	generalized-alpha	generalized-alpha	generalized-alpha
Time step size	0.01s	0.01s	0.1s	0.1s
Time	10s	10s	10s	10s

Table 3. Parameters involved in the two-dimensional multiphase fluid model of the sample digitization in COMSOL

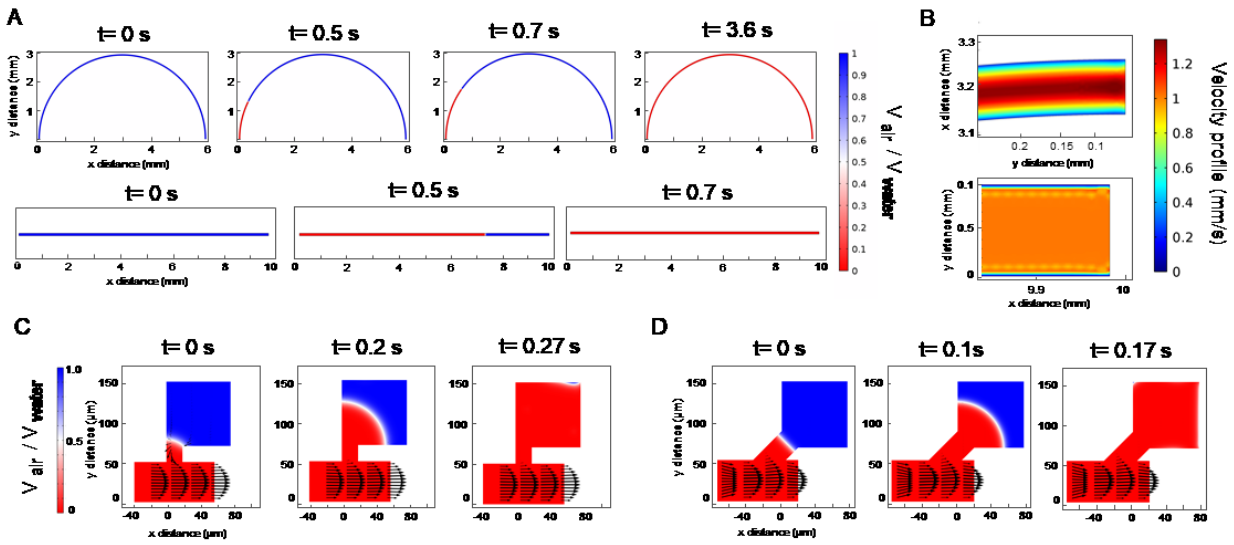

Figure 4.2. Simulation Results

(A) COMSOL simulation results of sample loading in 180° curved vs. linear main channels with same length by two-dimensional water-air multiphase flow CFD analysis. (B) Aqueous sample velocity profiles of each channel geometry after the channel was filled with the aqueous sample. COMSOL simulation results of sample digitization by two-dimensional water-air multiphase flow CFD analysis before (t_0), (C) Straight (D) 45° inclined chamber filling; shown are the color contours of the water volume fraction ranging from blue = air to red = water (refer to the color legend) and the water/air interface. The vectors show the flow velocity in the whole geometry. This figure is reprinted with permission from reference [111].

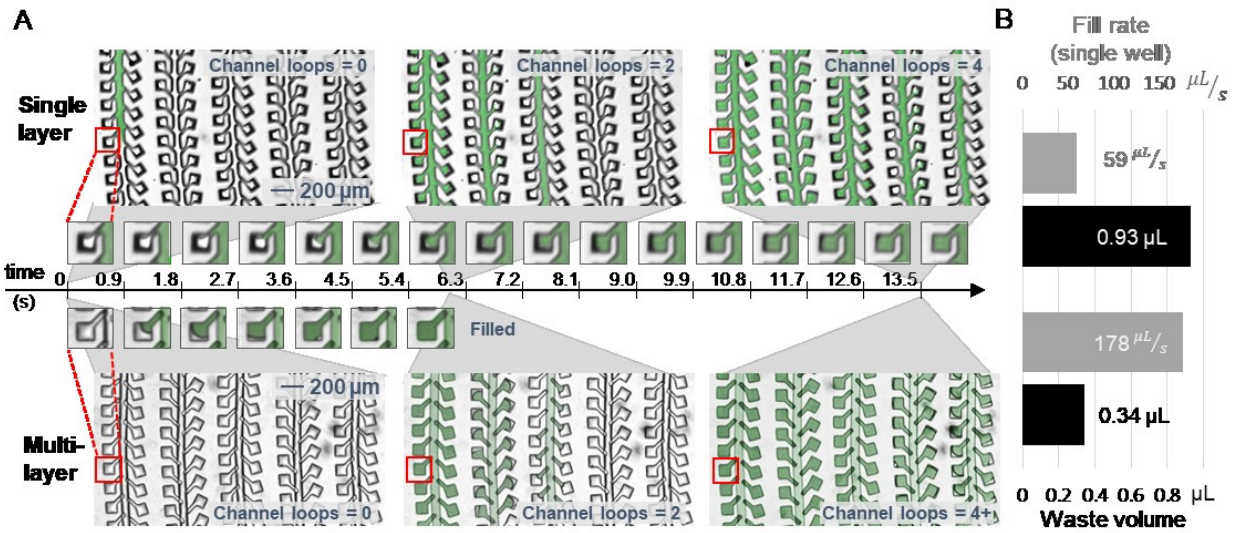

Figure 4.3. 2D vs. 3D Comparison of Fill Rate and Waste Vlume

(A) Continuous images were acquired during loading of dye into a single layer and multilayer device. A timer starts when the dye first passes the single observation well, and ends when the well is fully filled. (B) The fill rate, time to fill a single 750 pL well, is much faster for the multilayer device. The waste volume, volume of liquid that is in the channels past the observation well at the time of fully filled, is lower for the multilayer device than the single layer. This figure is reprinted with permission from reference [111].

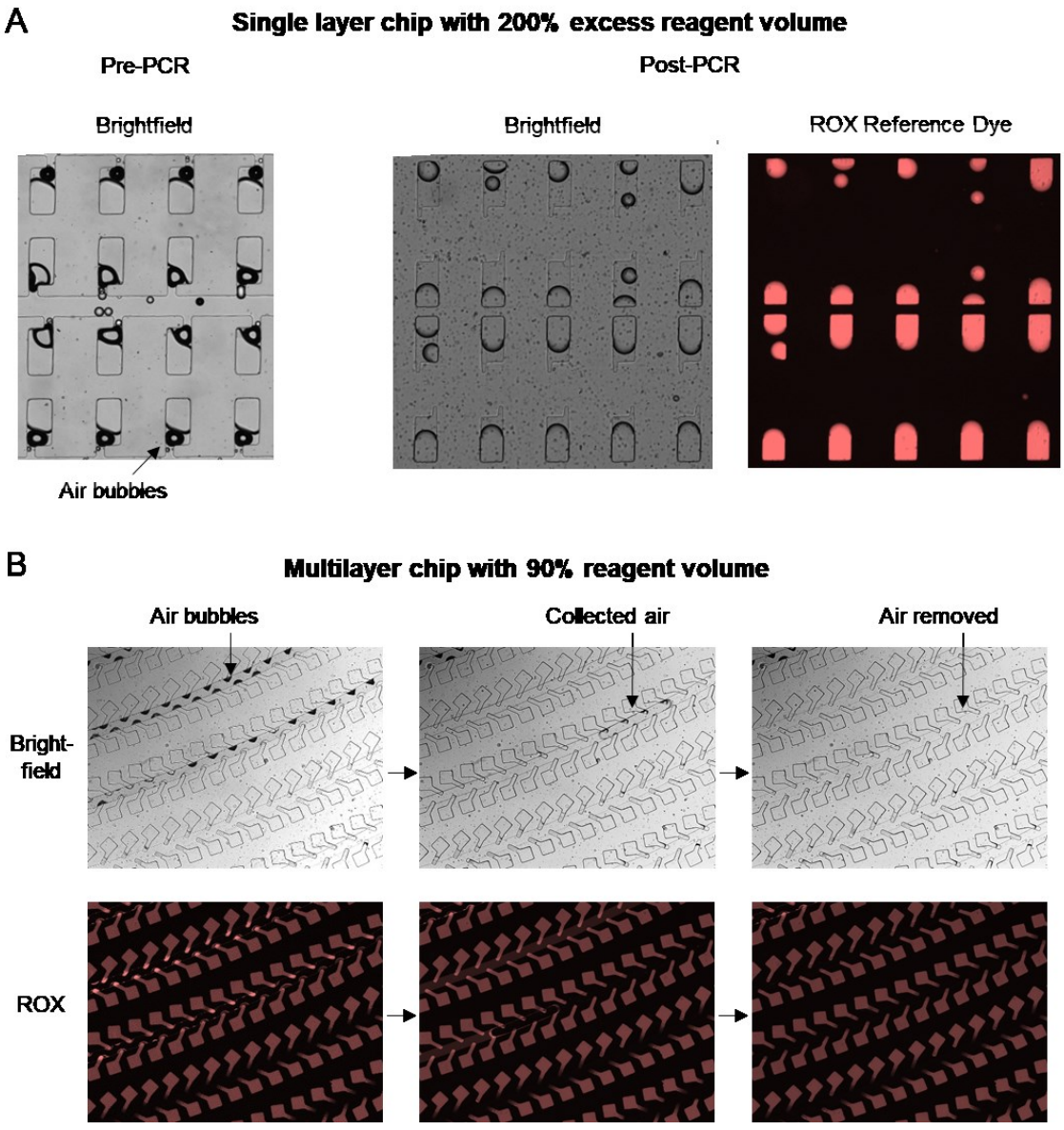

Figure 4.4. Loading volume vs. Reaction Success

Loading and partitioning of single-layer microfluidic device. The device has a capacity of 4 µL and was loaded with 8 µL. Air entered the chip after loading and resides in the wells after partitioning. This air caused significant evaporation and sample loss during heating steps. (B) Loading and partitioning of multilayer device. The device was loaded at less

than full capacity to minimize loss. Air collects in the channels and is removed by oil partitioning. This figure is reprinted with permission from reference [111].

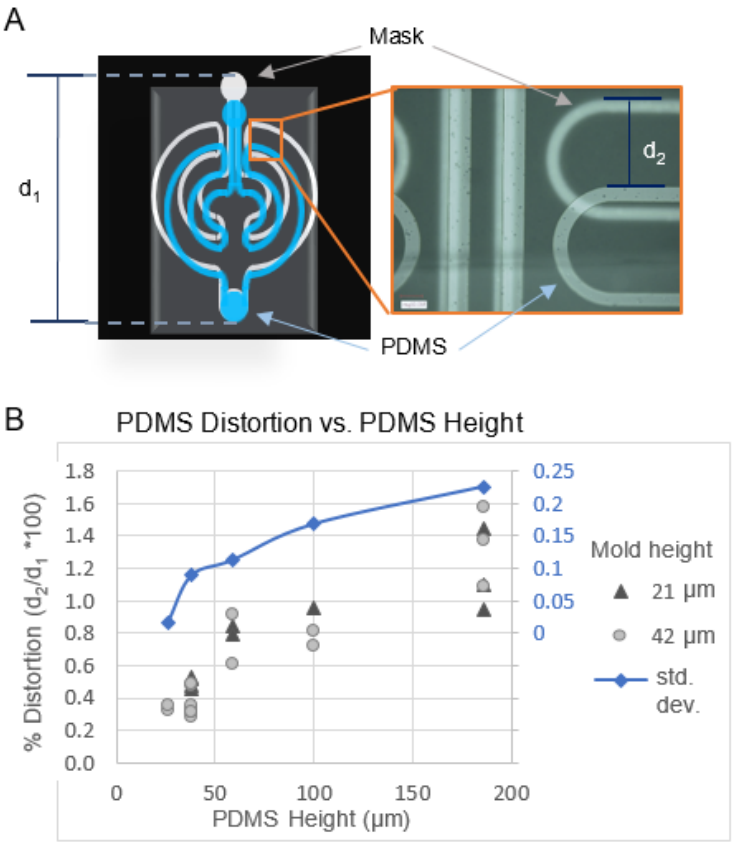

Figure 4.5. PDMS Warping vs. Thickness

(A) The PDMS pattern was aligned against the mask to measure the percent distortion. (B) The distortion was compared at different PDMS thicknesses for molds of two different resist heights. This figure is reprinted with permission from reference [111].

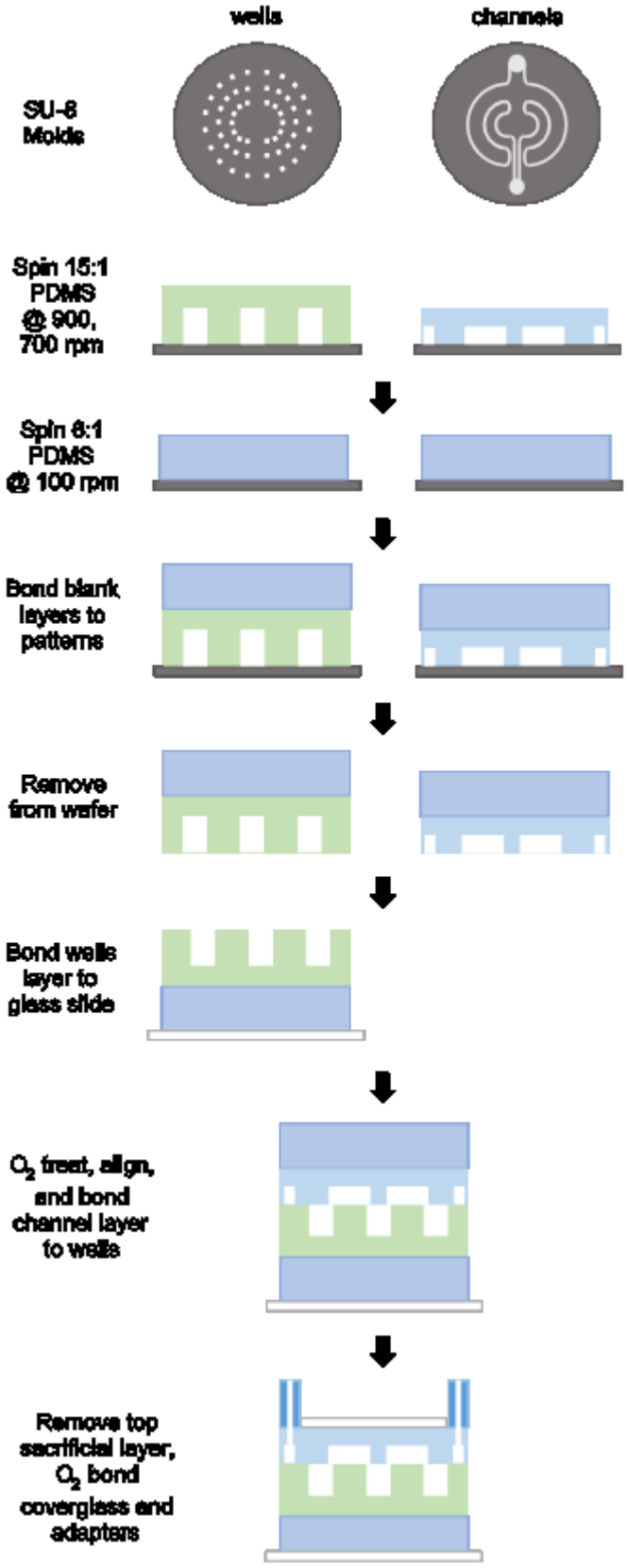
wells
channels
SU-8 Molds
Spin 15:1 PDMS @ 900, 700 rpm
Spin 6:1 PDMS @ 100 rpm
Bond blank layers to patterns
Remove from wafer
Bond wells layer to glass slide
O_2 treat, align, and bond channel layer to wells
Remove top sacrificial layer, O_2 bond coverglass and adapters

Figure 4.6. Multilayer Fabrication Protocol

Ultra-thin layers of PDMS were spun on each pattern mold, and removed by temporary bonding of a sacrificial layer. The two patterns were then oxygen-plasma treated, aligned, and bonded. Finally, a coverglass and adapters where oxygen-plasma bonded. This figure is reprinted with permission from reference [111].

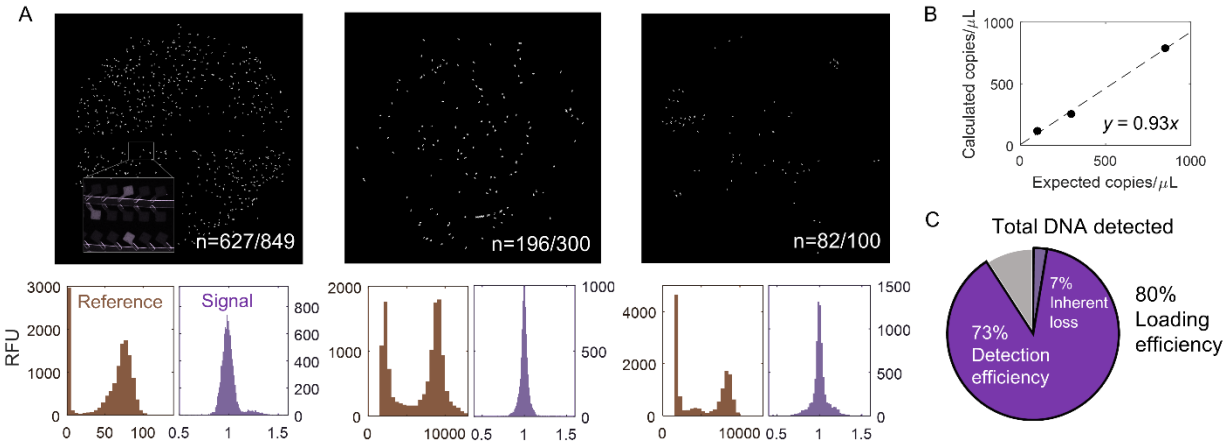

Figure 4.7. Loading and Detection Efficiency

(A) Fluorescent images were captured of the positive wells for a dilution of methylated $p14^{ARF}$. The reference dye was used to detect loaded wells, and a threshold was applied to calculate the total number of amplified DNA copies. (B) After accounting for the unloaded wells, the calculated copies per µL was compared to the expected. The relationship is linear with a slope of 0.93. (C) On average, 73% of the template molecules are detected. 7% of the sample is lost during preparation or storage, resulting in an estimated loading efficiency of 80%. This figure is reprinted with permission from reference [111].

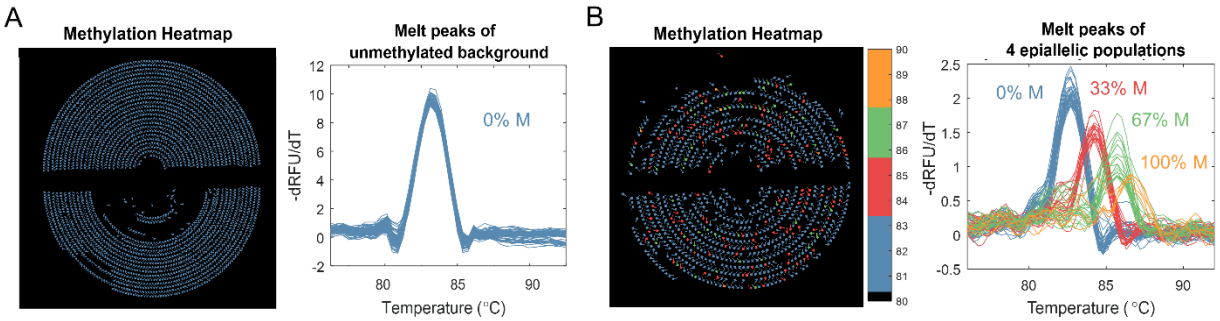

Figure 4.8. Epiallelic Discrimination

(A) Unmethylated sequences of $p14^{ARF}$ were amplified and discriminated by melt. (B) Epialleles at three defined methylation densities were loaded into the device along with the unmethylated background. All patterns were then amplified and discriminated by melt temperature. This figure is reprinted with permission from reference [111].

Chapter 5

DROPLET DIGITAL HIGH RESOLUTION MELT

Overview of Droplet technologies

Clinical adoption of new technologies requires both strong analytical capabilities as well as sufficient throughput for patient or sample load, a factor that is often overlooked in development of microfluidic platforms. Despite advances in microchamber real-time analysis platforms, such static arrays will always be limited in throughput compared to droplet technologies. The ability to serially generate as many droplets as needed provides for fundamentally unlimited sensitivity and much higher throughput. Thus, many laboratories are realizing widespread adoption of commercial droplet digital PCR (ddPCR) platforms.

Droplet microfluidic platforms have greatly enhanced the throughput and sensitivity of single-molecule and single-cell analyses. However, real-time analyses of individual droplets remain challenging. Most droplet microfluidic platforms have

fundamental drawbacks that undermine their utility toward applications that rely on real-time monitoring to identify rare variants, such as bacterial persistence, drug discovery, antibody production, epigenetic biomarker analyses, etc. We present a platform for high-density droplet trapping and real-time analysis with 100% loading and trapping efficiency at a packing density of 110,000 droplets per in^2. To demonstrate real-time analysis capabilities, we perform digital PCR and parallelized digital high-resolution melt curve acquisition on droplets to discriminate methylation levels of a tumor suppressor gene, *CDO1*, on a molecule-by-molecule basis. We hope that this platform, which is compatible with a large range of droplet sizes and generation technologies, may facilitate high-throughput real-time analyses on a molecule-by-molecule or cell-by-cell basis of heterogeneous populations.

Droplet platforms have been used to detect and analyze nucleic acid and protein biomarkers as well as single cells with drastically higher sensitivities than bulk methods [64], [112]–[116]. Furthermore, with advances in droplet microfluidic technologies, commercial platforms like BioRad QX200 ddPCR and RainDance RainDrop have become turnkey tools for a wide range of clinical applications, such as copy number variation [117]–[119], biomarker detection [120]–[123], gene expression analysis [124]–[126], and pathogen detection [127], [128].

Despite their tremendous advantages in sensitivity and throughput, most existing droplet platforms rely on sequential measurements of each droplet and its assay reactants at a single predetermined time point ("endpoint analysis") [129]–[132]. This limitation precludes their utility in biological assays that rely on or benefit from time-resolved

measurements of reactants ("real-time analysis"), such as molecular profiling using melting curve analysis [60], [63], [73], [111], [133]–[135], cell growth monitoring [136], [137], and enzyme kinetics observations [58], [138]–[140].

For effective real-time analysis of individual droplets, it is advantageous to immobilize the droplets such that they can be easily monitored over the course of the assay. However, previous attempts at developing such a real-time droplet analysis platform have resulted in a tradeoff, in which there is a reduction in either throughput or droplet capture efficiency. To ensure trapping of many or most of the droplets in a reaction, some methods directly generate droplets into a chamber or reservoir for reaction and analysis [59], [103], [141]–[143]. However, once loaded, these devices are sealed and droplet generation halted while all required reaction steps are performed in the chamber. Therefore, these "on-chip" methods are inherently limited in throughput, as the entire device is restricted to a single run of a single condition or sample, especially for multistep assays that contain time-consuming reaction or incubation steps. Even with multiple devices, the number of reactions or samples that may be parallelized is constrained by the two-dimensional surface area of commercial heaters. Moreover, the footprint of these chambers may be inefficiently utilized, as they retain the immiscible oil phase used in droplet generation.

In contrast, trapping strategies that are fundamentally compatible with "off-chip" droplet production allow high-throughput parallelization of time-limiting reaction steps on conventional 96- or 384-well plates before subsequently attempting to capture the droplets in an array/chip for analysis. These methods potentially enable simultaneous assessment of

multiple reactions, a range of reaction conditions, or large patient/sample cohorts for time-limiting reaction steps in a high-throughput manner that is favorable for translational potential. In addition, the throughput of subsequent real-time analyses can be further enhanced by incorporating multiple trapping units on a single device. However, current "off-chip" trapping designs have poor capture efficiencies, only capturing and analyzing a small percentage of overall droplets [58], [136], [144]–[146], as a large number of droplets tend to bypass the storage chambers and are lost when loading the array.

Ultimately, loss in either throughput or droplet capture efficiency undermines the utility of current platforms towards clinical analyses of rare molecules or biomarkers and applications that require real-time monitoring to identify extremely rare variants, such as bacterial persistence [147], drug discovery [148], directed evolution [149], antibiotic resistance [150], and circulating biomarker analysis [63], [73], [110], [111], [133]. To overcome this tradeoff, we have developed a real-time droplet platform that enhances the overall throughput of droplet real-time analyses by maximizing space utilization, operational flexibility, and capture efficiency.

Herein we present a microfluidic platform with 100% loading efficiency for high-density droplet trapping and real-time monitoring that is universally compatible with other droplet systems. The platform consists of a microfluidic droplet trapping device and a thermal-optical platform for parallelized real-time analyses across a wide range of temperatures. The trapping device employs a simple, passive immobilization strategy that is fundamentally compatible with any droplet size, and therefore is congruent with existing commercial droplet platforms.

Highly efficient loading and capturing of droplets via pseudo-sieve

The presented platform enables high-density trapping and immobilization of droplets for real-time monitoring and detection of rare molecules or variants. The platform consists of two main components: (1) the droplet trapping and immobilization device, which loads and immobilizes droplets at 100% efficiency by means of a sieve-like floor, and (2) the thermal-optical imaging platform, which acquires fluorescent images of all droplets within the device at specified temperatures. We implement this platform to perform high resolution melt (HRM) analysis for detection and discrimination of rare methylated biomarkers.

We previously developed a technique termed DREAMing, Discrimination of Rare EpiAlleles by Melt, as a facile means of detecting various methylation patterns on a molecule-by-molecule basis amongst high background [63]. Briefly, the technique utilizes methylation-preferred or methylation-agnostic primers to amplify all bisulfite-converted methylation patterns of a given locus at single-copy sensitivity. Next, the sequences are discriminated by HRM by observing the sequence-dependent release of a DNA intercalating dye during thermal ramping. However, this technique performs quasi-digital analysis via conventional multiwell plates with limited dynamic range of detection and sensitivity, thereby undermining its practicality for clinical use. To address this, we developed a microfluidic digital array platform called HYPER-Melt in which we implement this technique in a high density array of nanowells [73]. This microfluidic digital array platform enables detection and discrimination of methylated variants at

frequencies as low as 0.00005%. We then further improved the platform by increasing the loading efficiency from 12% to 80% [111]. However, this on-chip integrated system suffers from low throughput due to minimal parallelization of the time-consuming PCR step (three hours) required before dHRM analysis (five minutes).

Therefore, we sought to implement this technique on a digital droplet platform in order to significantly improve performance in terms of sensitivity and throughput. Whereas the array-based device is limited to performing ~4 to 6 PCR reactions in parallel on a single thermocycler, a commercial ddPCR system such as the BioRad QX200 may digitize as many as 8 samples into droplets at once, and can perform the time-limiting PCR step on as many as 96 samples simultaneously. By incorporating off-chip PCR thermocycling with a multi-module droplet trapping device and HRM platform, the system can realize both higher loading efficiency and much higher throughput.

To perform droplet digital HRM (ddHRM), we compartmentalized the reaction mix into droplets by flow-focusing. Droplets for each sample to be analyzed were loaded into a well of a 96-well plate and amplified by PCR in parallel on a thermal cycler. Next, droplets were loaded into the trapping device, and melt curves were acquired from each amplicon via the thermal-optical platform. After analysis, a population profile of various methylation levels was generated for each sample.

Device Architecture

100% Efficient Loading and Trapping Mechanism

The high-density packing device consists of a glass microscope slide at the base and two PDMS layers, an upper droplet chamber and a lower pseudo-sieve floor (Figure 5.1A). Up to five modules may be assembled in parallel onto a single glass slide as needed. Within each module, the pseudo-sieve layer is comprised of tightly spaced eight-sided polygonal posts (Figure 5.1B). The intermittent top surfaces of each post are defined as the "floor" of the droplet chamber. The continuous surface at the bottom, between each post, is considered the "basement" of the device. A "highway", or space without posts, runs between columns at approximately each third of the device to evenly space the droplets and relieve pressure.

The grid-like arrangement of the posts creates an array of gaps in the floor of diameter d_g between the corners of each post. Upon entering the chamber, the height of the ceiling (h_c) is less than the spherical height of each droplet, such that droplets are under slight compression between the ceiling and the floor (Figure 5.1C). Droplets favor placement over the gaps due to the decrease in surface tension [145]. The tight spacing between posts prevents droplets from escaping below the chamber into the basement of the device, whereas any excess oil between droplets may pass between the posts, through the basement, to the outlet of the device (Figure 5.1D).

Droplets are pressure-loaded into the device inlet with a syringe pump (Figure 5.1E). Upon reaching the droplet chamber, droplets self-assemble into a grid-like arrangement over the posts. Once reaching the end or side walls of the chamber, droplets are unable to escape, thereby demonstrating 100% efficiency in loading. Excess space

occupied by oil in the droplet chamber can be removed through the basement to achieve 100% efficiency in trapping at a packing density of 110,000 droplets per in^2 (Figure 5.1F).

Scalable Droplet Capacity

In most single-point disseminating loading mechanisms, wherein droplets are propelled by pressure-driven flow, a pressure gradient develops as more droplets accumulate downstream and offer resistance. Since the pressure is greatest at the inlet, this limitation is known as "back-pressure." Excess back-pressure is a common problem in many microfluidic trapping systems which limits the total amount of droplets that can be loaded while maintaining droplet stability [139]. In earlier generations of the device design, we observed increased compression of droplets due to pressure during filling of the final corners of the device, especially at the center regions on each end (Figure 5.2A), which could compromise droplet integrity.

To address this, we implemented "highways" to reduce back-pressure and to facilitate even distribution of droplets throughout the device chamber during loading. The highways run through the initial 75% of the device, whereupon they cease to ensure trapping at the distal end. After implementing highways between each third of the device, droplets were observed to exhibit uniform, minimal compression throughout the device (Figure 5.2B, Figure 5.3). Therefore, the device design is fundamentally scalable to higher droplet capacities.

High-throughput real-time melt curve methylation profiling from droplets

Although the key goal in developing this device was to provide real-time monitoring capabilities, the device and imaging platform may also be utilized for highly accurate quantification and detection of rare molecules. While current commercial platforms may include separate fluorescent readout instrumentation, they provide no means of visual inspection and droplets are irrecoverable after analysis. Droplets in the high-density packing device may be quantified with any fluorescence platform as well as bright-field microscopy to allow for visual inspection of the droplets.

To validate the accuracy of the system, a serial dilution of synthetic DNA, representative of bisulfite-converted 100% methylated *CDO1*, was partitioned into 500 pL droplets, amplified in a 96-well plate, and then loaded onto the trapping device. The device was placed on the thermal-optical platform to acquire a single wide-field fluorescent image. The droplets were segmented in ImageJ, whereupon the number of positive droplets was calculated from the Poissonian occupancy equation. The assay was also cross-validated by performing the same protocol in bulk and with the Biorad QX200 system (Figure 5.4).

The expected occupancy of the synthetic target ranged from 11% to 0.04%. The calculated vs. expected occupancies are shown in Figure 5.5 (log-log). The lower occupancies were repeated thrice while the higher occupancies were tested once. A linear regression curve was fit in Matlab, producing a slope of 0.98 with an R^2 of 0.99. These results demonstrate the utility of this platform for highly accurate droplet quantification, and provide a simple alternative to complex commercial droplet readers.

System Versatility

Due to the wide range of applications utilizing droplet technology, a fundamental aspect of the device design was versatility in droplet generation platforms and in droplet size. Therefore, we assessed the loading performance of our device across a range of common droplet volumes. Devices capable of producing 100 pL, 600 pL, and 1000 pL droplets using flow-focusing discretization were designed. The devices included geometric modifications of the flow-focusing nozzle used in devices we have previously developed [151]–[153]. Droplets were also generated using the BioRad QX200 platform and assessed for compatibility with the trapping device and real-time system. The device demonstrated 100% efficiency in loading of droplets ranging from 100 pL to 1 nL (Figure 5.6).

The increasing number of applications of droplet technology may be attributed to the increased availability and reliability of commercial droplet platforms [154], such as BioRad's QX200 droplet system and RainDance's RainDrop Plus platform. In addition, increased research into surfactants and other droplet stabilizers [65], [100], [149], [155] has propelled the development of microfabricated droplet generation systems [65]–[67], [156]–[158]. With this device, we demonstrate loading and analysis of droplets generated by both our microfluidic droplet generation device as well as droplets generated by the Biorad QX200 system. By integrating this device with other droplet systems, real-time analysis of droplets can be achieved without compromising throughput.

Droplet Immobilization and Real-time Imaging

For time-lapse analyses of densely-packed systems, droplet immobilization is critical to reduce the computational burden of droplet identification and ensure analytical

confidence. We demonstrate droplet immobilization on the device by evaluating the position of post-PCR droplets in time-lapse fluorescent images during thermal ramping. A mastermix was prepared with synthetic DNA representative of bisulfite-converted methylated *CDO1*, from which 600 pL droplets were generated in a flow-focusing device. After ddPCR in a 96-well plate, the droplets were loaded into the trapping device. The device was sealed on both ends and placed on the thermal-optical platform.

Fluorescent images were acquired of the droplet trapping chamber during thermal ramping (Figure 5.7). A grid is superimposed over a sub-region of the device to illustrate the relative position of droplets between frames. Even at high temperatures, droplets remain immobilized and stable, validating the robustness of the trapping mechanism. This simple immobilization technique does not require any external equipment, and provides a facile means to maintain discretization of signals from adjacent droplets in densely-packed high-throughput systems.

Parallelized Droplet Digital High Resolution Melt (ddHRM)

We illustrate the potential utility of this platform towards analysis of heterogeneous populations by performing droplet digital High Resolution Melt (ddHRM) to discriminate molecule-by-molecule methylation patterns of bisulfite-converted DNA. Synthetic DNA molecules representative of bisulfite-converted 0%, 50%, and 100% methylated *CDO1* were digitized into 600 pL droplets. Droplets were then aliquoted into a 96-well plate and amplified in a thermal cycler following a standard PCR protocol with methylation-

preferred primers as previously described [63]. Next, droplets were loaded onto the droplet trapping device and placed on the thermal-optical platform for HRM analysis.

Wide-field fluorescent images of the droplet trapping region were acquired at 0.3°C intervals during temperature ramping. To extract information from each individual droplet, the images were first segmented in ImageJ (Figure 5.8) to identify the position of each droplet (Figure 5.9A). Next, an automated Matlab script extracts the fluorescent information from each droplet at each temperature interval to generate melt curves (Figure 5.9B). The peak of the negative derivative of each curve defines the melt temperature (T_m) of each sequence. A digital melt histogram then displays the T_m of each amplicon, which clearly depicts three distinct populations. The methylation density of each droplet can then be classified by its T_m, providing a quantitative population profile of methylation heterogeneity.

The system exhibits a high signal-to-background ratio of 1.9, and analysis of surrounding negative droplets shows minimal change over the course of HRM acquisition (Figure 5.10). Fluorescence leakage or diffusion between droplets was not observed, however, these system characteristics should be assessed for each application, as different assays, reaction mixes, or oil compositions may result in different behavior.

DNA methylation is one of the most-commonly studied epigenetic alterations in cancer progression [8], [11], [15], [16]. Recent studies have shown that variable methylation levels within a locus correlate with disease progression [27], [28]. Furthermore, many models predict that methylation levels are highly variable early in

carcinogenesis [29], [31], [110]. We hope that this device and platform will enable further study into the effects of variable methylation on cancer etiology.

We developed a high-density droplet trapping device and thermal-optical platform for time-lapse analyses of up to 30,000 droplets in parallel. Single molecules of DNA were compartmentalized, amplified, and quantified at high accuracy across three orders of magnitude at concentrations as low as 0.8 copies per μL. We demonstrated the utility of this platform by profiling variable methylation levels of a tumor suppressor gene (*CDO1*) with ddHRM. To our knowledge, this represents the first demonstration of ddHRM.

The pseudo-sieve functionality of the droplet chamber enables 100% loading and trapping efficiency, thus the device is highly suitable for analysis of rare molecules or variants. The simple, passive immobilization strategy is compatible with droplets of different sizes and many readily-available imaging modalities. We demonstrated effective mitigation of back-pressure, indicating that the design is readily-scalable to higher droplet capacities and throughput.

There are aspects of the device design that could see readily-achievable improvements. First, droplets have the potential to be recovered by reversing the direction of flow in the device. Second, the throughput may be further increased in both sample number and droplet capacity. Within a chamber, although the scaling potential is not expected to be limited by back-pressure, a larger droplet chamber with a high aspect ratio (w/h) may experience sagging during fabrication. This could be simply addressed by incorporating support posts throughout the larger device. Finally, higher resolution photolithography techniques may be utilized to produce finer spacing in the pseudo-sieve

layer. This would permit even smaller droplets to be captured and analyzed in the trapping region. Incorporating this improvement may also lead to increased dynamic range and sensitivity of the platform. We hope that researchers may utilize this technique to develop better understanding of population heterogeneity and improve detection of rare biomarkers.

Methods

Device Fabrication

Two photomasks were designed in L-Edit v16.0 (Tanner EDA, Wilsonville, OR, USA) for the upper chamber and for the pseudo-sieve post array and were printed onto high-quality transparency (CAD/Art Services, Bandon, OR, USA). To fabricate the molds, two silicon wafers were dehydrated for at least 6 hours, and oxygen-plasma treated at 85 W for 1 min (Technics PE-II, San Jose, CA, USA). For the upper chamber, SU-8 3050 (MicroChem, Woburn, MA, USA) was spun at 3000 rpm for 30 s, baked at 65°C for 1 min and 95°C for 15 min, and exposed at 180 mJ/cm2. For the pseudo-sieve layer, the SU-8 3025 (MicroChem, Woburn, MA, USA) was spun at 1800 rpm for 30 s, baked at 65°C for 1 min and 95°C for 14 min, and then exposed at 175 mJ/cm2. Following exposure, both wafers were baked for 1 min at 65°C and 5 min at 95°C, developed with SU-8 developer, and baked at 200°C for 1 hr.

The devices were fabricated from the master molds through soft lithography with 30 g of PDMS (Ellsworth Adhesives, Germantown, WI, USA), mixed at a ratio of 10:1 (w/w) with curing agent. The two layers were oxygen-plasma treated at 40 W for 45 s for bonding. A glass microscope slide (#26007, TedPella, Redding, CA, USA) and a

coverglass slip (#260340, TedPell, Redding, CA, USA) were then oxygen-plasma treated at 40 W for 45 s and bonded to the bottom and top of the device, respectively. The devices were baked overnight at 80°C, and desiccated for 2 hours. Prior to use, FC-40 oil was vacuum-loaded into the device.

Droplet Generation and ddPCR

The aqueous phase was first drawn into a 100-cm-long section of Tygon tubing (#EW-06419-01, Cole-Parmer, Vernon Hills, IL, USA) with an inner diameter of 500 μm. The Tygon tubing section was then connected to a Hamilton 1000 glass syringe (SKU#20998, Sigma-Aldrich, St. Louis, MO, USA) containing FC-40 oil (SKU#F9755, Sigma-Aldrich, St. Louis, MO, USA), which served as the displacement fluid for injecting the aqueous phase into the device using a syringe pump (Harvard Apparatus, Holliston, MA, USA) at a flow rate of 640 μL/h. Droplet generation oil was injected into the device using a separate syringe pump at 2400 μL/h. Generated droplets were collected from the device's outlet into a 1.5 mL DNA LoBind Tube (#022431021, Eppendorf, Hauppauge, NY, USA).

Device loading was observed using a custom microscope with a 4 x objective lens (UPlanFl 4×/0.13 NA, Olympus, Tokyo, Japan) and a CMOS camera (#DCC1545M, ThorLabs, Newton, NJ, USA).

Image analysis

To perform droplet segmentation and identification, the first 10 images were loaded into ImageJ and averaged56. The resulting image underwent morphological opening, followed by a morphological segmentation of radius gradient 1 to segment and identify each droplet57. The droplet mask was then exported to Matlab for analysis along with the subsequent images. An automated script MATLAB (MathWorks, Natick, MA, USA) extracted the average raw fluorescence for each droplet at each temperature point and binned the values in 0.3°C intervals to generate a melt curve for each droplet. After Savitzky-Golay filtering of each curve, the negative derivative was taken to identify the peak, or melt temperature (Tm) of the droplet amplicon. The methylation density of the amplicon in each droplet was identified by thresholding.

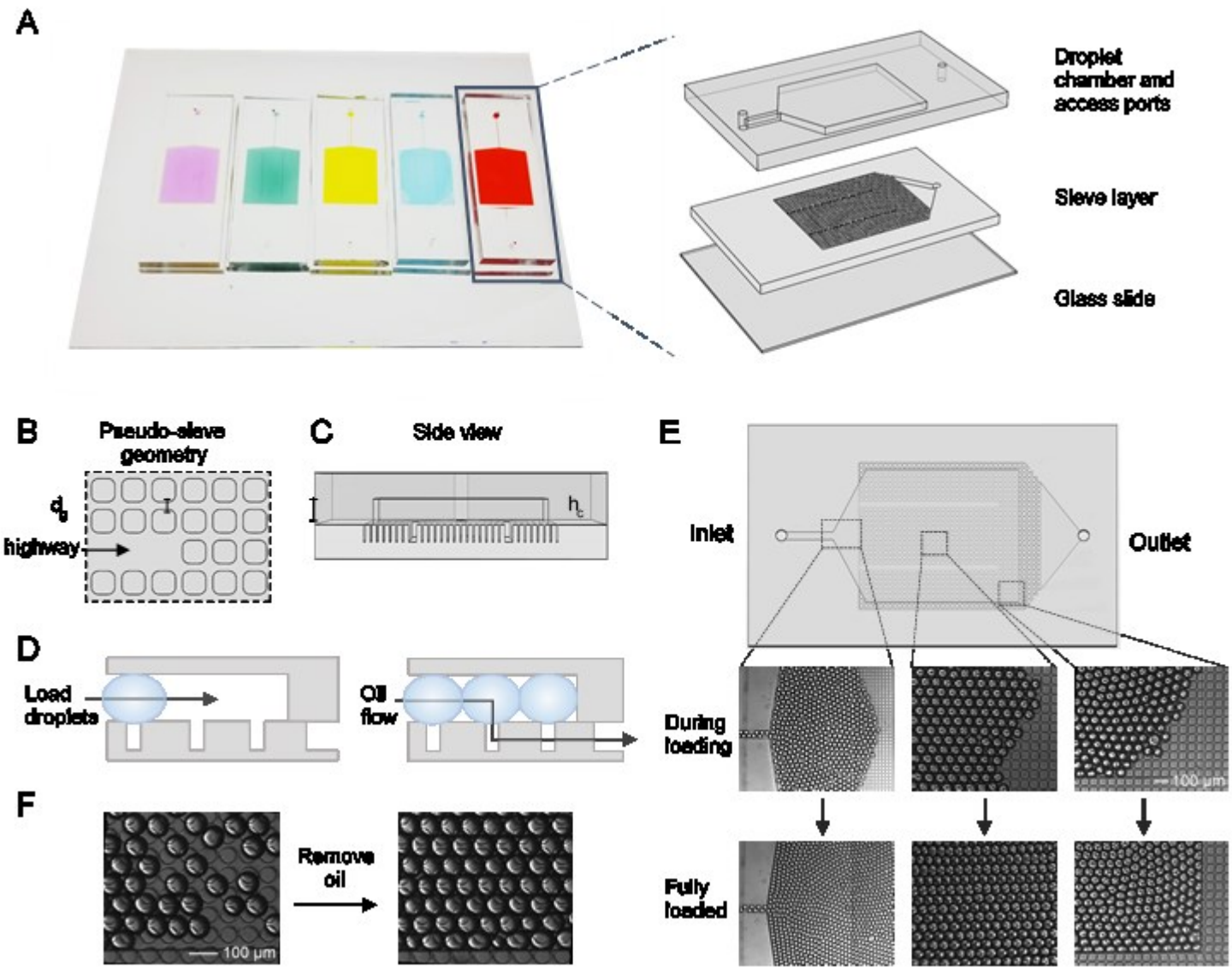

Figure 5.1. Droplet Trapping Device Architecture

(A) The high-density trapping device may incorporate up to five modules as needed. Each module consists of a glass slide, PDMS sieve layer, and PDMS chamber layer with access ports. (B) A top view of the pseudo-sieve geometry shows the tightly spaced posts. Two highways run through each third of the device. (C) Droplets sit in the chamber above the posts. (D) Droplets are loaded until the chamber is full. Excess oil may pass through the

posts to the outlet. (E) Droplets are pressure loaded into the inlet, and self-assemble into a grid while loading. Droplets are trapped against the walls and immobilized. Since no droplets may escape, the device exhibits 100% loading efficiency. (F) The removal of excess oil removes wasted space between droplets, such that they may be packed in a high-density array for highly efficient loading. This figure is reprinted with permission from reference [159].

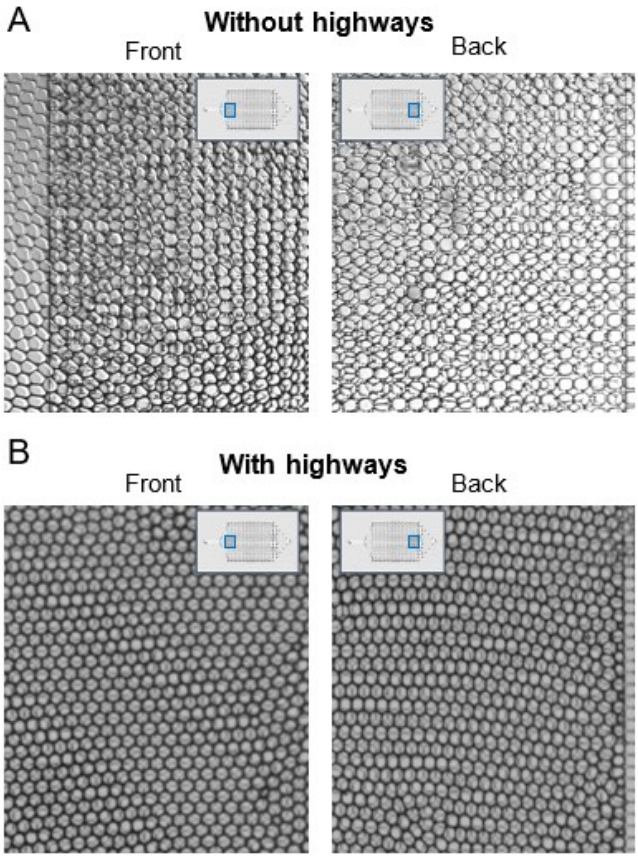

Figure 5.2. Back-Pressure Relief

(A) Droplets loaded into previous versions of the device (without highways) experience compression. Compression was most significant in the central lanes of the device. Snapshots are shown of the proximal and distal areas. (B) With highways to help spread the flow of droplets evenly, droplets remain uniform throughout the device and experience only minimal compression due to high-density packing. This figure is reprinted with permission from reference [159].

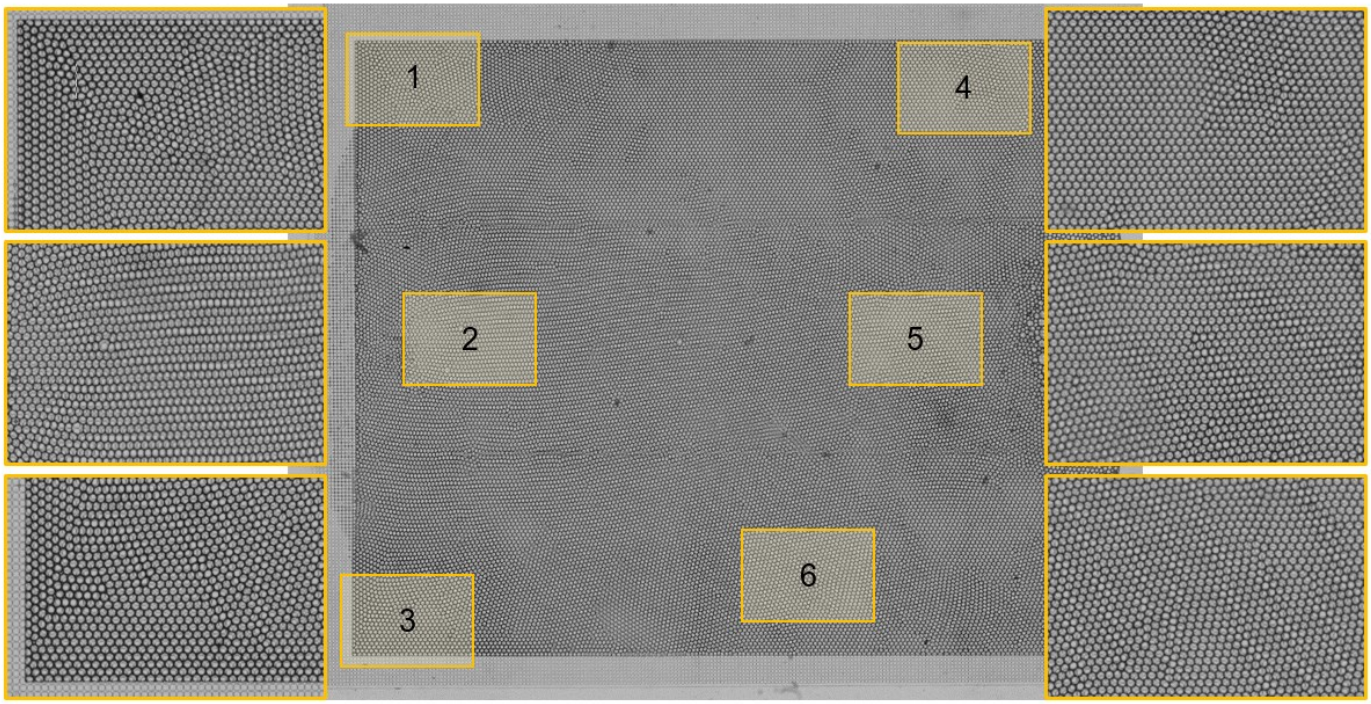

Figure 5.3. Fully loaded device with 500pL droplets

Droplets were generated by flow-focusing, and underwent ddPCR in a BioRad C1000 Touch Cycler. Droplets were then loaded into the trapping device with a syringe pump. Once, loaded, the device was sealed on both ends. Images were taken under an Olympus microscope with a 4X objective and stitched together using ImageJ. This figure is reprinted with permission from reference [159].

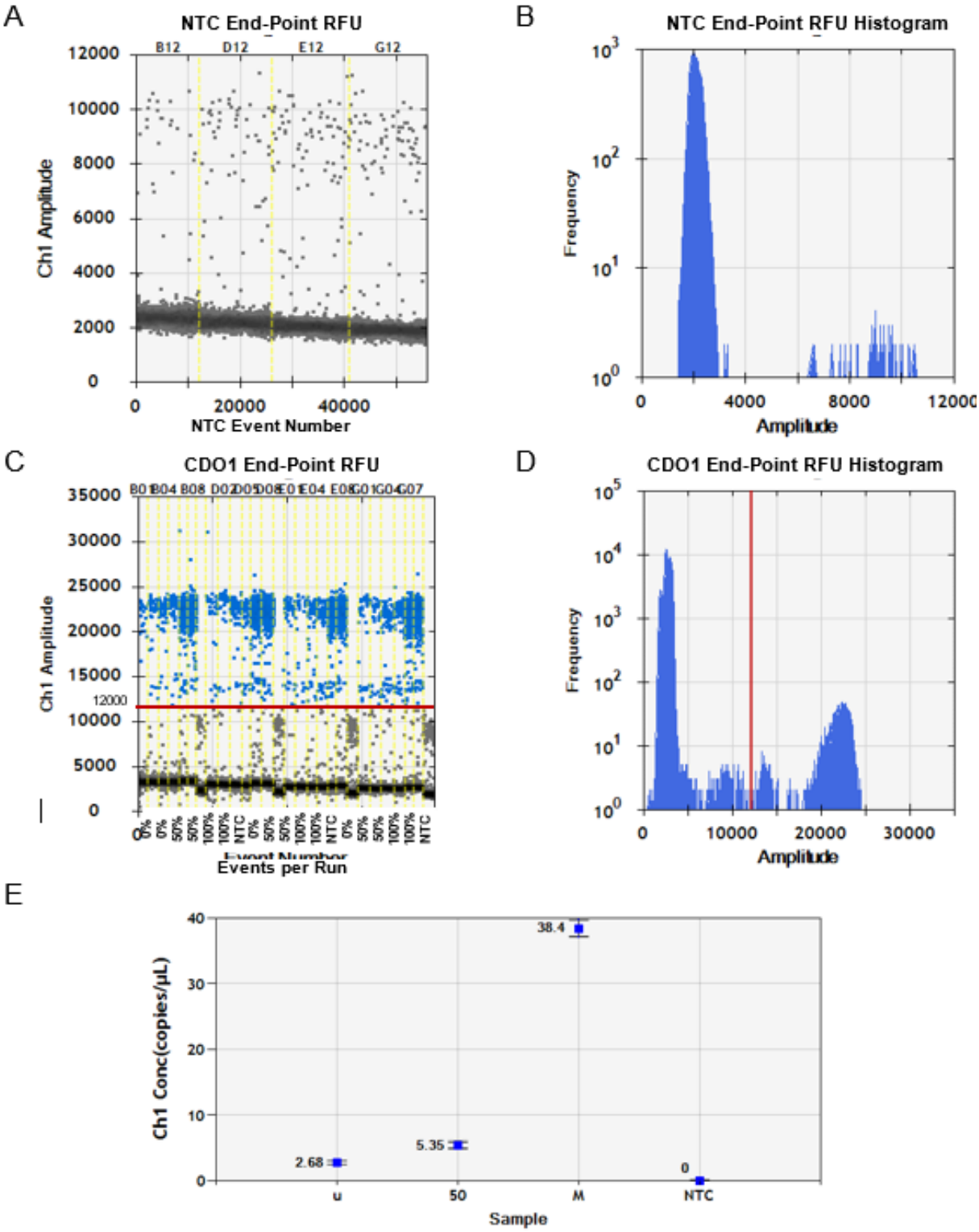
A
NTC End-Point RFU
B12
D12
E12
G12
Ch1 Amplitude
NTC Event Number
B
NTC End-Point RFU Histogram
Frequency
Amplitude
C
CDO1 End-Point RFU
Ch1 Amplitude
Events per Run
D
CDO1 End-Point RFU Histogram
Frequency
Amplitude
E
Ch1 Conc(copies/µL)
38.4
5.35
2.68
0
u
50
M
NTC
Sample

Figure 5.4. CDO1 DREAMing with QX200 System

Droplets were generated following the BioRad QX200 protocol containing target of 0%, 50%, and 100% methylated CDO1 as well as a no-template control. The data was analyzed by BioRad QuantSoft software program. (A,B) The end-point fluorescent readout of the NTC was used to set a threshold of 12000. (C,D) The NTC threshold was used to identify the number of positive droplets for each target epiallele. (E) The concentration of each target was calculated by the number of events with BioRad QuantSoft. Each epiallele was repeated 8 times and showed very consistent results that closely matched the expected concentration. This figure is reprinted with permission from reference [159].

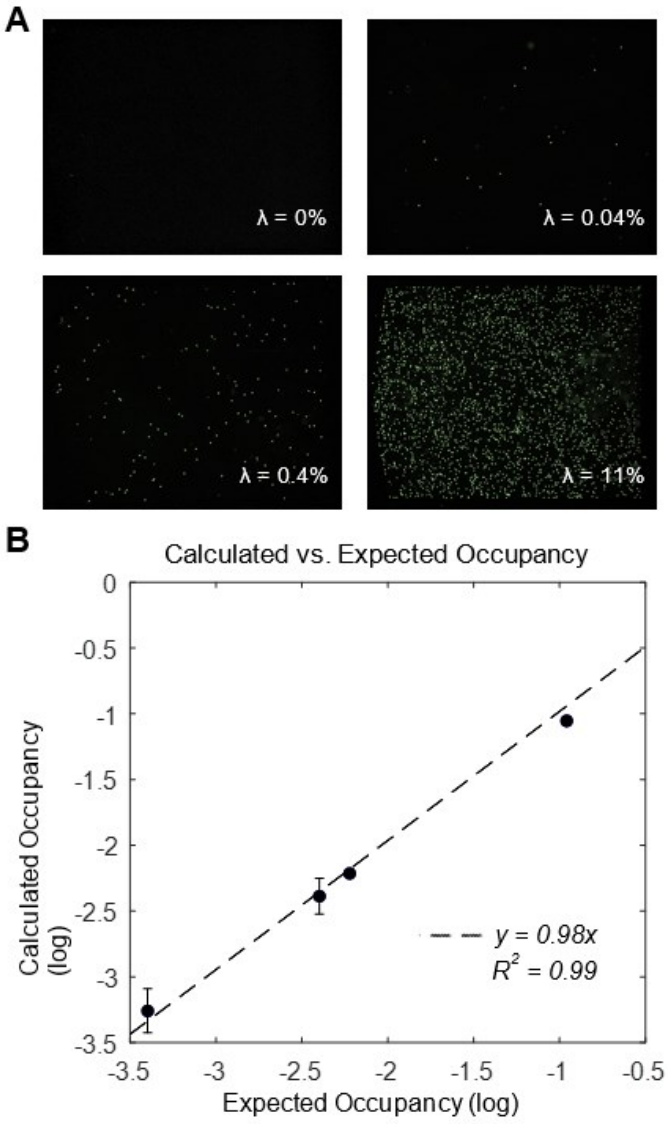

Figure 5.5. Quantification Accuracy

(A) Droplets were generated with target copies of bisulfite-converted methylated CDO1 at occupancies (λ) spanning 4 order of magnitude, from 0.04% to 11%. After PCR, the droplets were loaded into the trapping device and their fluorescence imaged with a wide-field camera. Droplets were identified and counted in ImageJ. (B) The occupancy was calculated from the Poissonian occupancy based on the ratio of negative to total droplets and compared to the expected occupancy. The lower two and highest occupancies were

repeated twice. A linear fit was applied to the log-log curve of expected vs. calculated over the serial dilution. The slope of 0.98 is within 2% of the ideal slope of 1, and a R^2 value of 0.99 indicates an excellent fit. This figure is reprinted with permission from reference [159].

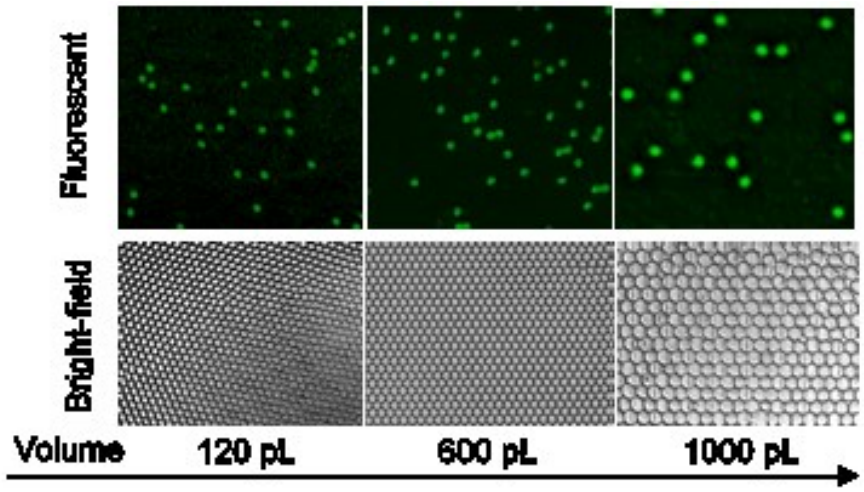

Figure 5.6. Size Versatility

120 pL and 600 pL droplets were generated with our flow-focusing device. 1000 pL droplets were generated by the QX200 ddPCR system. Each droplet size underwent the same PCR protocol in a 96-well plate, and were subsequently loaded into the trapping device for imaging. Fluorescence images were acquired with the same wide-field camera and macro lens and the same working distance. Bright-field images were all acquired under an Olympus microscope at 4X magnification. All systems were compatible with the range of droplet sizes. This figure is reprinted with permission from reference [159].

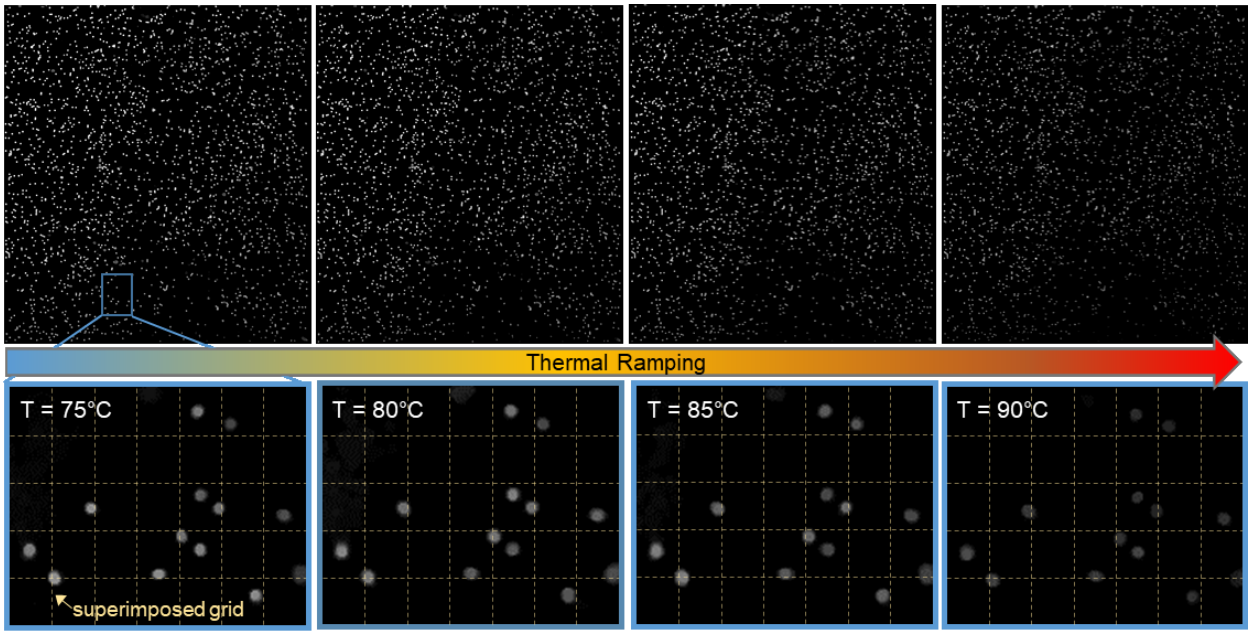

Figure 5.7. High-Temperature Immobilization

After loading, the device was sealed on both ends and placed on the thermal-optical system for real-time analysis. To demonstrate immobilization even at high, challenging temperatures, fluorescence images of the droplet capture region were acquired during thermal ramping from room temperature to 90°C, shown here in 5° intervals. A superimposed grid over a sub-region of the device pinpoints the position of each droplet from frame-to-frame. Droplets remain immobilized throughout in order to facilitate analysis of individual droplets. This figure is reprinted with permission from reference [159].

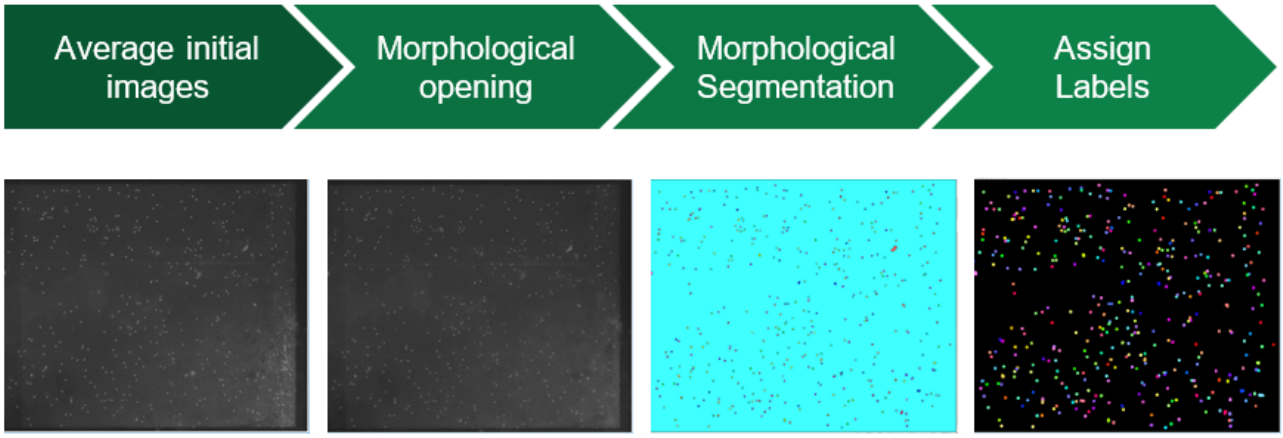

Figure 5.8. Image Processing and Droplet Segmentation

Droplet segmentation was performed in ImageJ. The first ten fluorescent images were averaged together to increase the signal to background ratio. A morphological opening filter was applied to the resultant image using MorphoLibJ. Morphological segmentation then identified each droplet. A numeric label was assigned to each droplet, and a labeled mask was generated and exported to Matlab for quantification and melt curve analysis. This figure is reprinted with permission from reference [159].

Target	Sequence
CDO1 Unmethylated	GGACGAGGCGGAGAGTTATTTAAGAAAGGTGGTGGAGGTGG GGAGATTTTGTGGGTATGGTTTATGTGTATATTTTTGGTTTTTT TGGGTTTTGTGTTTTTTTTAAGAGTTTCGTTGTTTTCGG
CDO1 50% Methylated	GGACGAGGCGGAGAGTTATTTAAGAAAGGTGGCGGAGGTG GGGAGATTTTGCGGGTATGGTTTACGTGTATATTTTTGGTTTT TTCGGGTTTTGCGTTTTTTTTAAGAGTTTCGTTGTTTTCGG
CDO1 100% Methylated	GGACGAGGCGGAGAGTTATTTAAGAAAGGTGGCGGAGGCG GGGAGATTTTGCGGGTACGGTTTACGCGTATATTTTCGGTTTT TTCGGGTTTCGCGTTTTTTTTAAGAGTTTCGTTGTTTTCGG
CDO1 Fwd Primer	GGACGAGGCGGAGAGTTATTT
CDO1 Rev Primer	CCGAAAACAACGAAACTCTTAAA

Table 4. Synthetic Sequences of CDO1

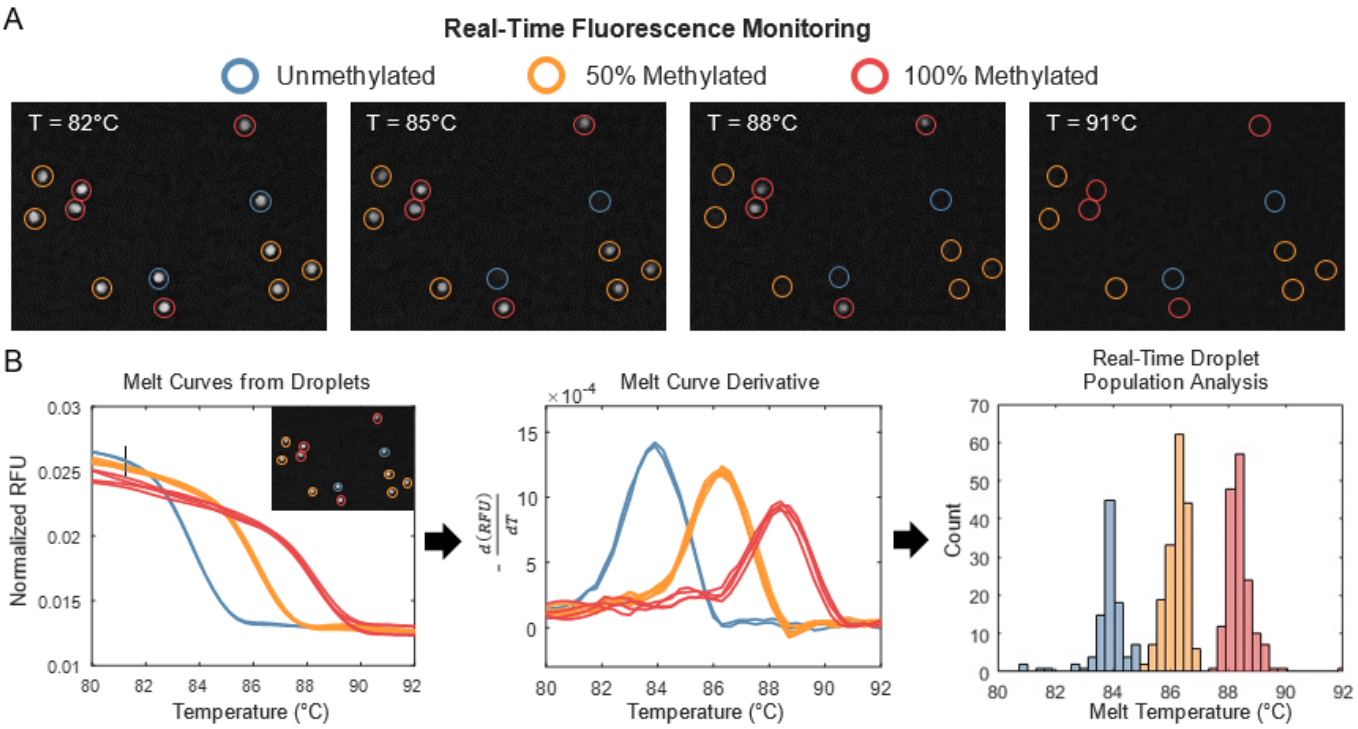

Figure 5.9. Droplet Digital High Resolution Melt

(A) Fluorescence images of droplets containing amplicons of mixed epialleles were acquired during temperature ramping. Each epiallele denatures at distinct temperatures, measured as a loss of fluorescence of the dsDNA intercalating dye (Evagreen). (B) The average fluorescence of each droplet is plotted against temperature to obtain a melt curve. The negative derivation of the curve contains a peak, which is identified as the melt temperature (T_m) of the sequence. By identifying the T_m of each amplicon, a profile of the methylation heterogeneity within the sample may be obtained and analyzed. This figure is reprinted with permission from reference [159].

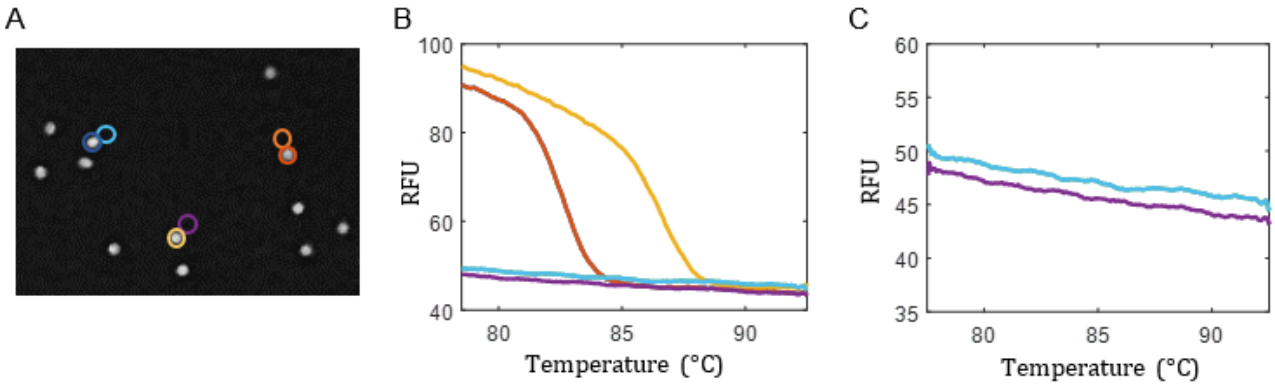

Figure 5.10. SNR and Fluorescence Leakage Analysis

(A) Negative droplets surrounding the positive amplicons were identified to analyze the background signal. (B) The system demonstrates a signal-to-background of 1.9 at 80°C. (C) Closer inspection of background droplet fluorescence shows a slight decrease over the course of the experiment, indicating no decrease of the overall SNR and no observable fluorescence leakage between droplets. This figure is reprinted with permission from reference [159].

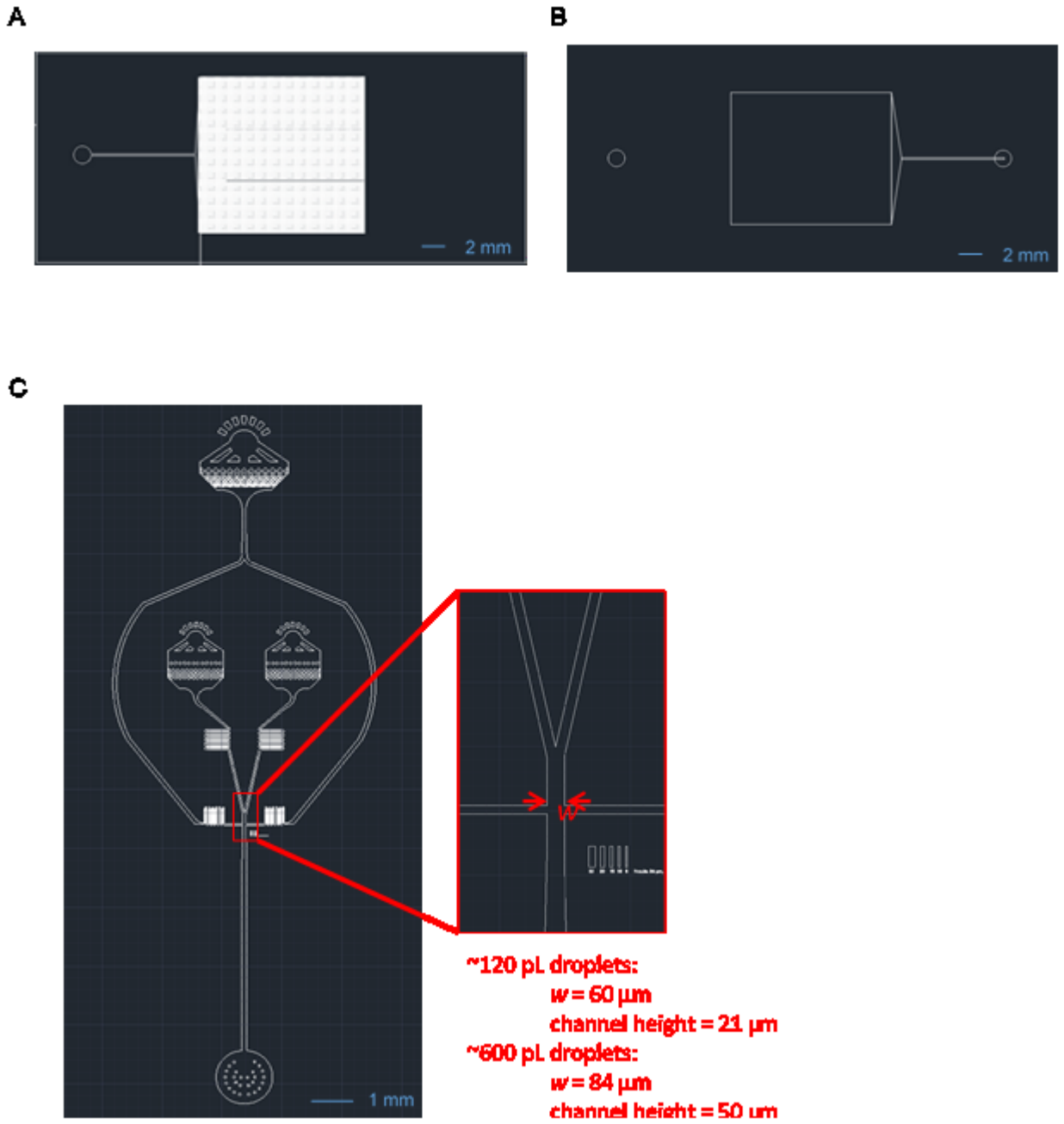

Figure 5.11. Droplet Generation Devices

Two masks were designed for the high-density droplet packing device, including a (A) post layer mask, where polarity is positive, and a (B) chamber layer mask, where polarity is negative. (C) A flow-focusing droplet generator was used for generating 120 pL and 600

pL droplets. The nozzle width and channel height were custom-tuned in order to achieve the desired droplet volume. This figure is reprinted with permission from reference [159].

Chapter 6

ASSESSMENT OF BIOMARKER PANELS

Diagnostic advantages of biomarker panel assessment

Diagnostic tests for a given disease are scored by two metrics: (1) The percentage of positive test results from a truly positive sample set. This is known as the "True Positive Rate" (TPR), and is also referred to as the sensitivity of a test or biomarker. (2) The percentage of positive test results from a negative or healthy sample set. This is known as the "False Positive Rate" (FPR), and is referred to as the specificity of an assay. A perfect diagnostic test will score a perfect TPR of 1 and a perfect FPR of 0. A TPR of less than 1 indicates that either test cannot detect low levels of a biomarker or that the particular biomarker is not present in all of the disease instances. A FPR be above zero indicates that the biomarker can also be found naturally in the healthy population. Most diagnostic tests are not ideal, in that there is some overlap between the cancerous and healthy populations. Thus, a threshold must be determined that defines both the TPR and FPR. To visualize the

performance of a test, researchers most often use what is known as the "Receiver Operating Characteristics" curve, a plot of 1-FPR vs. TPR. The area under the curve (AUC) determines the probability that a test with be able to distinguish between disease and healthy.

Cancers express large amounts of both intra- and inter- tumor heterogeneity, leading most scientists to believe that pathogenesis may occur via a variety of different pathways. Thus when aiming for early detection, a single biomarker is likely to be insufficient for much of the population. Cancers have also been shown to express both epigenetic intra-tumor heterogeneity, that is epigenetic differences between patients, as well as inter-tumor heterogeneity, that is epigenetic differences within clones of a single tumor. For example, lung cancer exhibits significant genetic and epigenetic heterogeneity, which presents a challenge for development of a successful screening technique [160]. Several groups have investigated screening for lunch cancer methylation biomarkers in noninvasive bodily fluids such as plasma and sputum [161]–[163]; these studies have illustrated that detection of biomarker panels from at least 3-5 genes is required for clinically actionable sensitivity and specificity, although there is still room for improvement. Furthermore, studies have shown that early in carcinogenesis, but before malignancy, methylation levels may be highly variable in tumors levels [20], [30], [31]. This suggests that quantification of methylation variability within these panels may further improve diagnostic accuracy.

Perhaps one factor contributing to the imperfect sensitivity of these techniques is the low levels of methylation in these fluids. Current technologies are ill-suited to quantify

methylation variability in complex solutions where the target molecules may be rare and infrequent. Sequencing, although comprehensive, is limited in sensitivity and is unpractical for routine use. Digital PCR technologies, such as droplet digital PCR, are limited to binary assessments of known target sequences, and thus are not suited for detection of variably modified loci. Thus there is a need for a more sensitive technique that can simultaneously assess a panel of methylation biomarkers.

To satisfy the requirement for simultaneous biomarker assessment, some researchers have proposed spatial separation as a simple means to enable multiplex analysis with PCR-based methods, but this comes at a sacrifice of efficiency. Spatial separation inherently requires more reaction volume and therefore intrinsic waste, as only minor percentages of the sample input are interrogated for a single marker. Due to the scarcity of biomarkers in noninvasive fluids, this method is unsuitable for early detection of large panels of rare molecules in complex fluids such sputum and plasma.

The most common and straightforward method of multiplex analysis within a single PCR-based assay is to use different color probes for each target. Typically, taq-man probes are used, which include a fluorophore and quencher at either end of a DNA sequence corresponding to its target, such that the fluorescence emission cannot be detected in its natural state. The probe anneals to its single-stranded DNA target sequence during the PCR reaction. As the Taq polymerase performs extension over that region, the probe sequence is cleaved, enabling the fluorescence emission to be detected.

Single color-per-target multiplexing is limited by the spectral overlap of known fluorophores within the visible electromagnetic spectrum. Even with advanced optical

setups, typically this method is limited to the detection of 4-5 targets, which may not be sufficient for diagnostic confidence. In commercial digital PCR (dPCR) systems such as the BioRad QX200 and Fluidigm BioMark HD, only up to 2 or 3 fluorescent channels are available for detection.

Several attempts have been made to expand the multiplexing capacity of digital PCR systems, but none are capable of simultaneous quantification of methylation heterogeneity. For example, several methods of multiplexing by detecting melt profiles of taq-man probes or molecular beacons have been proposed, but these methods require an abundance of single-stranded DNA, produced by asymmetric PCR, and thus are incompatible with intercalating dye-based HRM, which requires double-stranded DNA [125], [164], [165]. Alternatively, it has been proposed that using different concentrations of probe permits identification of different targets in the same color by detecting different fluorescent intensities, however this technique has only been demonstrated for detection of known sequences [66], [166].

Previously, we developed a facile molecule-by-molecule sequence analysis platform called HYPER-Melt [73]. Through digitization of single molecules into individual microchambers, methylation patterns could be interrogated by digital melt curve acquisition. This technique demonstrated very high sensitivity, 0.00005% methylated/unmethylated, but was limited to a single target locus. Herein, we expand this technique to simultaneously detect multiple target loci, thereby improving its potential clinical utility.

We present a methylation-agnostic ratiometric multiplexing scheme to enable high-degree multiplexing of different targets as well as sequence profiling with HYPER-Melt within a single assay. This simple technique can be prepared as an all-in-one reaction, requires no additional reaction steps, and includes straightforward analysis. Methylation-agnostic probes were developed to identify their loci independent of its methylation pattern. Bisulfite-converted sample was loaded into a microfluidic array to digitize each target locus (Figure 6.1A). Using a dual-fluorophore ratiometric analysis scheme enables a high-degree of multiplexing, which grows exponentially with each additional color (Figure 6.1B). Finally, the methylation profile of each loci can be determined simultaneously through discrimination by HYPER-Melt (Figure 6.1C).

Variable Sequence (Methylation-agnostic) Probe Scheme

In order to identify a panel of loci with unknown methylation patterns, we first sought to overcome the challenge of designing probes specific to variable sequences. After bisulfite conversion, potential methylation sites in a sequence (CpG sites) may be either converted to uracil, replaced by thymine during PCR, or remain as a cytosine. Therefore, any sequence with n possible methylation sites may result in 2^n sequences after bisulfite conversion. In many cases, finding a suitably long template without these variable sites is impossible, thus it is necessary to identify multiple patterns.

To address this, we developed fluorescent probes with so-called “wobble bases” incorporated at each methylation-dependent base in the target locus (Figure 6.2). These “wobble bases” are equimolar mixtures of either cytosine or thymine. Ultimately this

results in equimolar probe amounts for each possible bisulfite-converted sequence. The resulting probe solution is thus "agnostic" to target epiallele methylation status, allowing its identification regardless of template methylation pattern.

Ratiometric Multiplexing Scheme

We next coupled this agnostic probe design to a ratiometric fluorescence multiplexing scheme to achieve a solution that provides high multiplexing capability while maintaining compatibility with dsDNA binding dyes, thereby allowing both simultaneous identification and HYPER-Melt analysis of many epiallelic gene targets (Figure 6.3A). For each target, two probes comprising identical sequences are designed but are differentially labeled with two different fluorophore-quencher pairs, such as yellow and red. This allows the probes to be mixed at a distinct red-to-yellow (R:Y) molar ratio to create a specific fluorescence signature for each target locus. Multiplexing can thus be achieved by assigning probe-pairs with a distinct R:Y ratio to target each of the genes in a panel (Figure 6.3B).

This technique is simple in analysis, as it only requires two-color detection, but scalable to high degrees of multiplexing. There is no fundamental limit to the number of ratios that can be designed, thus the actual limit of multiplex capacity per probe-pair will depend on the resolution and dynamic range of the detector. Furthermore, for each additional probe color, the multiplexing capacity of this system will increase exponentially.

Digital Ratiometric Multiplex PCR

To perform an initial proof-of-concept of this technique, we selected three targets from a promising methylation biomarker panel for non-small cell lung cancer (NSCLC), *HOXa7*, *TAC1*, and *SOX17*, which has previously demonstrated an AUC of 0.89 and 0.77 for lung cancer detection in sputum and plasma respectively [167]. Methylation-agnostic probes were designed for each locus. After experimental optimization of multiple fluorophores, HEX and ROX minor-groove-binding (MGB) probes were chosen for identification.

We prepared reactions with different molar ratios of HEX and ROX probes for two targets, *HOXa7* and *TAC1*, ranging from 4:0 ROX:HEX (R:H) to 0:4. Synthetic sequences representative of bisulfite-converted methylated and unmethylated *HOXa7* and *TAC1* were designed and purchased. Each probe ratio was assessed for detection of a single-copy of the respective methylated and unmethylated template sequences. End-point fluorescence was acquired using the default HEX and ROX channels of a BioRad CFX. After background subtraction, the end-point RFU for each fluorophore of each well was normalized to the RFU a calibration curve consisting of the 1:0 ratio of the respective probe.

After calibration, the resulting molar ratios were calculated, which demonstrate excellent correlation with the expected probe ratio for each reaction (Figure 6.4). With this proof-of-concept, we demonstrate robust 5-plex detection by ratiometric probes with just two colors. Even though 5-plex detection may be sufficient for many biomarker panels, the technique is also readily scalable to higher degrees of multiplexing.

Microfluidic Digital N-plex Panel Identification

Next we validated the use of different probe ratios for multiplex target identification in a highly parallelized microfluidic array. A single module of the microfluidic array consists of 10,000 nano-liter sized chambers arranged in a single-layer grid. A single device may hold up to 4 modules in parallel for high-throughput testing. The devices were fabricated via ultra-thin soft lithography, vacuum-loaded, and partitioned following our previously reported techniques [73].

First, each target was interrogated independently among mixed probes to establish a reference standard. The devices underwent dPCR on a standard flatbed thermal cycler. Afterwards, the devices were imaged for end-point probe fluorescence by a typhoon scanner for two channels, Cy3 and Cy3-FRET. The negative wells for each device served as the background, and were used to correct for any module-to-module variability and for normalization of the positive wells.

A grid mask was mapped to the resultant fluorescence image to identify each well. A semi-automated program using four-corner selection was utilized to perform a homography transformation to align the mask to the image, as we have described previously [73]. Due to the intrinsic warping that occurs during soft lithography, this technique initially resulted in many wells with poor alignment. To address this, an interpolative algorithm was developed to predict the variable warping across the device. The vectorized fluorescent gradient for each predicted well position was acquired, and used for a two-step warping correction in both the horizontal and vertical directions. For

correction in the vertical direction, the vectorized y-gradient of each row was averaged and plotted against horizontal row number. A 4th-degree polynomial was fit to these points and the roots identified. Each row of wells was then translated up or down depending on the calculated magnitude of the average gradient at that point. Finally, neighborhood optimization was then used to correct for any nonlinear warping effects.

The central pixels of each well were averaged together to provide the end-point RFU per well. This process was repeated for the second fluorescence image. To determine if either the HEX or ROX channel were susceptible to spectral overlap from the intercalating dye (Evagreen), reactions were prepared with and without Evagreen and imaged under both probe channels after amplification. Neither channel appeared to exhibit nonspecific fluorescence emission from the Evagreen intercalating dye (Figure 6.5A). Finally, ROX RFU vs. HEX RFU scatterplots were generated to determine the confidence bounds of each probe ratio (Figure 6.5B). Each probe ratio is distinct and without overlap.

Next, mixed target loci were digitized in a single module with probe ratios of 1:3 for *TAC1* and 5:1 for *HOXa7*. Following dPCR, the module was imaged under HEX and ROX fluorescent channels, and the probe ratio for each amplicon was calculated. Comparison of the mixed loci demonstrates excellent agreement with the individually acquired probe results, validating the proof-of-principle that this method is suitable for multiplex identification (Figure 6.5B).

Microfluidic Digital N-plex assessment of methylation heterogeneity

Besides having a high degree of multiplexing capacity, the distinct advantage of this ratiometric probe technique is its compatibility with HYPER-Melt discrimination of locus-specific epialleles. After amplification, the device is placed on a thermal-optical platform for simultaneous melt curve acquisition from each amplicon as described previously [73]. Briefly, fluorescent images are acquired at 0.3°C temperature intervals from 75°C to 95°C. The average fluorescence of each well is extracted and plotted against temperature to produce a melt curve. The negative derivation of this curve contains a peak, which defines the melt temperature (Tm) of the template molecule. This Tm correlates with the original methylation density of the locus. For each amplicon, aggregating the Tm-methylation pattern and the probe-ratio-ID thereby enables methylation profiling for multiple targets.

To validate the performance of this device, synthetic sequences representative of bisulfite-converted fully methylated epialleles of two loci, *HOXa7* and *TAC1*, were synthesized and assessed. Each epiallele was digitized in the microfluidic array and amplified. Following amplification, melt curves were acquired for each amplicon, and a Tm histogram depicts the methylation profile of each sample (Figure 6.5C). The template methylation pattern of each amplicon can readily be identified by thresholding. The platform demonstrates high melt temperature uniformity for each epiallele.

Discussion

The report represents the first platform to demonstrate digital multiplexed molecule-by-molecule analysis of methylation heterogeneity. This platform enables

parallelized in-depth analysis into the mechanisms of two well-established phenomena of early disease progression: increasing epigenetic variability as well as the accumulation of aberrant regulation among several loci. Studying the methylation heterogeneity of multiple loci in parallel can provide greater insights into disease progression as well as increase the fidelity of molecular diagnostic techniques.

Genetic and epigenetic variability is an integral part of disease progression [1], [16]. Several models have predicted that increasing variability in DNA methylation occurs in precursor regions, before the onset of disease [29], [30], [110], [168]. The precise effects of this variability are only just beginning to be scrutinized. The paucity of current studies may be due to insufficient technology for quantitative, multidimensional analysis.

Assessment of methylation heterogeneity of rare molecules is challenging and unpractical with current commercial techniques. Targeted bisulfite sequencing could detect variability of multiple loci, however its high cost and complexity are often deterrents. Furthermore, its limited sensitivity would restrict its use to abundant samples such as tissue biopsies, which is ill-suited towards early detection of disease. A simpler, more sensitive technology that is becoming routine in research laboratories is ddPCR. However, detection of variable sequences with ddPCR would require probes for each sequence. Although feasible, each assay would be complex, and each variable-sequence probe would reduce the capability for multiplex analysis of different loci.

The ultimate goal of this work is to facilitate early detection of disease. Due to the myriad of possible tumorigenesis pathways and heterogeneity of disease, a single biomarker is unlikely to provide diagnostic utility in a large population. Especially in early

phases of disease, before malignancy, a diagnostic panel should assess the regulation of several pathways, as natural redundancies require several pathways to be disrupted before malignancy [169]. However, multiplex biomarker detection of rare molecules is challenging.

In noninvasive sampling techniques, such as plasma or cell-free DNA, tumor-derived molecules can be very infrequent, requiring larger than usual volumes of sample to be collected in order to capture these molecules. In such a case, the efficient use of the sample is critical to ensure that biomarkers are not excluded from analysis. Multiplex techniques that require physical partitioning of the sample are susceptible to lost information due to inefficient interrogation of the entire sample. The microfluidic multiplex digital melt platform presented here uses ratiometric probes to overcome that hurdle, enabling sensitive interrogation of all designated biomarkers.

Recent studies have shown promising results using methylation as a biomarker for early-stage NSCLC [161]–[163]. Our platform offers orders of magnitude higher sensitivity over traditional techniques as well as multidimensional analysis of n-plex gene panels. Ultimately, we hope that the capabilities of this platform manifest in improved diagnostic performance and thus improved clinical outcomes.

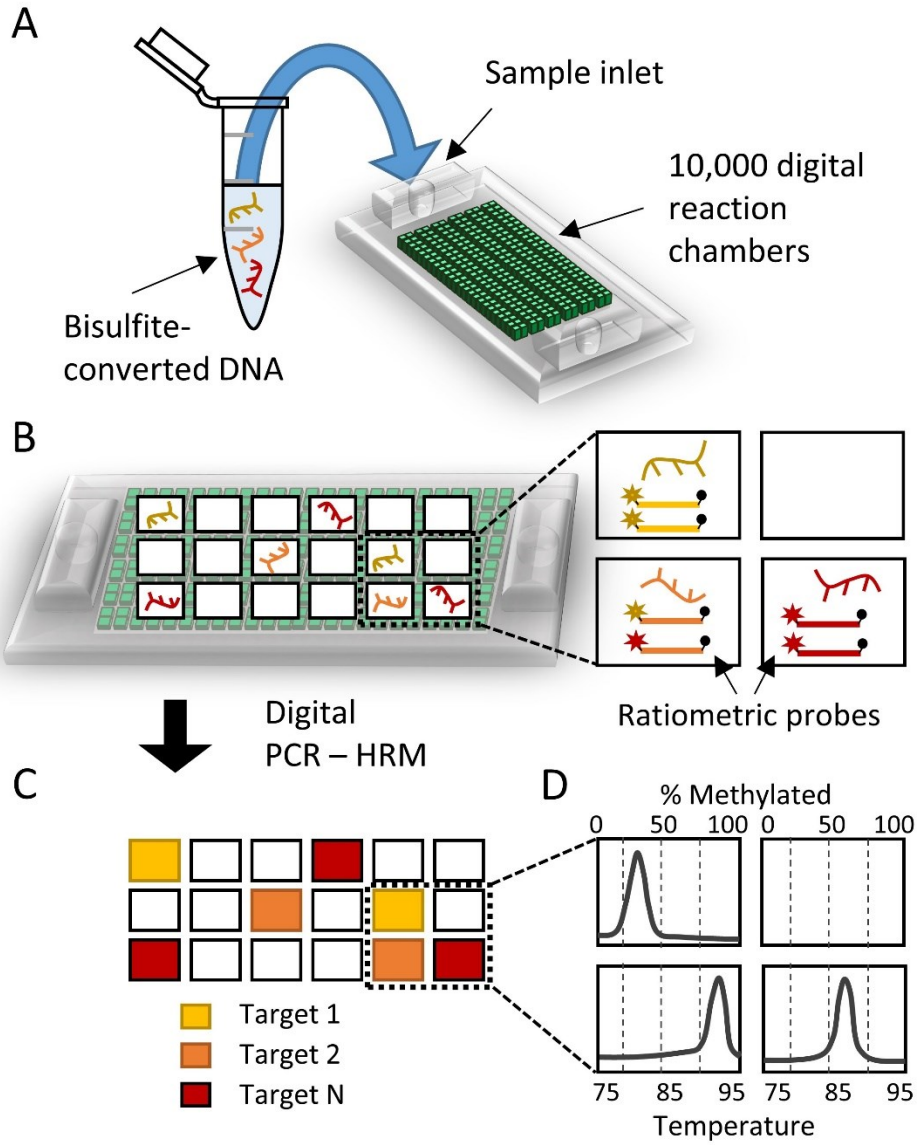
A
Sample inlet
10,000 digital
reaction
chambers
Bisulfite-
converted DNA
B
Ratiometric probes
Digital
PCR – HRM
C
Target 1
Target 2
Target N
D
% Methylated
0
50
100
0
50
100
75
85
95
75
85
95
Temperature

Figure 6.1. Overview of Multiplex HYPER-Melt Profiling

Bisulfite-converted DNA is loaded into the device and the fragmented DNA is digitized into microchambers (A). (B) For each target, probes with two fluorophores are mixed in distinct ratios to identify the locus. (C) After ratiometric probe-based identification, the methylation profile of each target is identified by parallelized digital HRM.

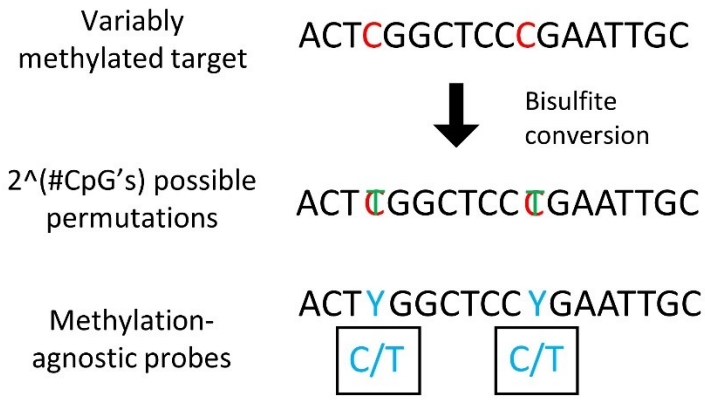

Figure 6.2. Methylation-agnostic probes

After bisulfite conversion, many possible sequences exist per locus. Wobble bases at potential methylation sites enable methylation-agnostic probe detection.

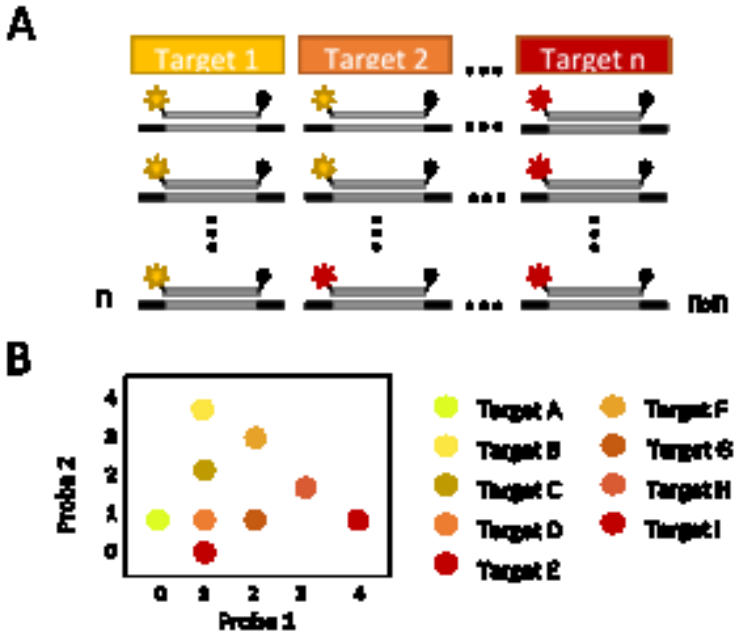

Figure 6.3. Highly multiplexed ratiometric probe scheme

For each target a distinct ratio of Yellow:Red probes are prepared (A), enabling high degrees of multiplexing with just two fluorophores (B).

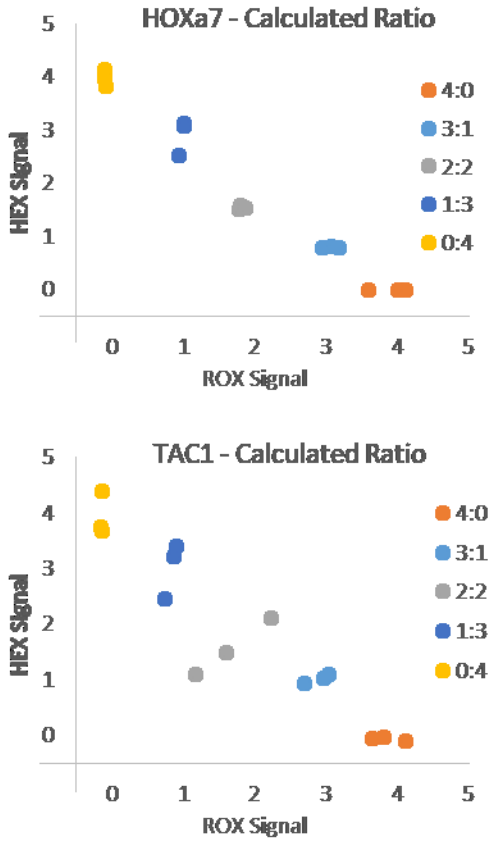

Figure 6.4. Ratiometric Identification principle

Five different ratios were prepared for each of two targets to demonstrate the ratiometric principle of identification. The calculated ratios closely match the target ratio, and cluster closely to enable ready identification.

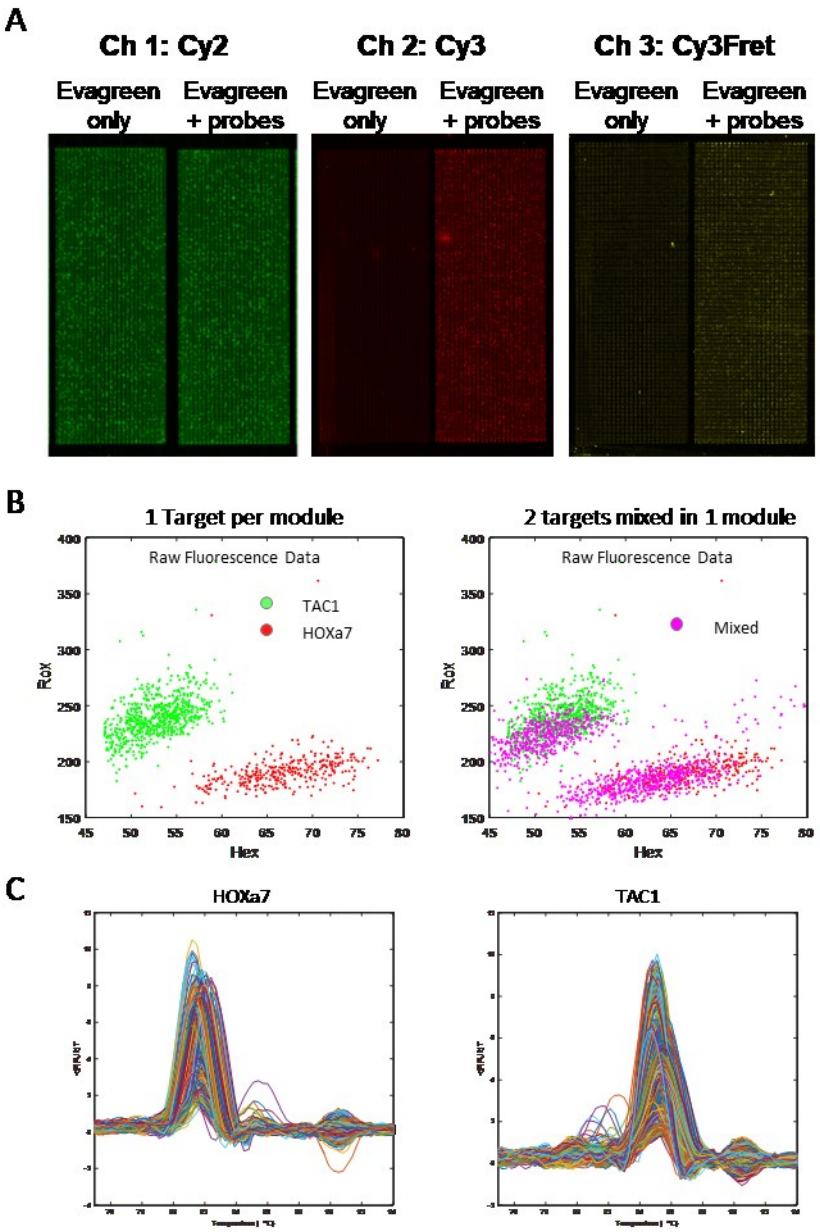

Figure 6.5. Simultaneous Locus Identification and Profiling

(A) Targets were digitized in the microfluidic device. In the first module, only Evagreen intercalating dye was used. In the second module, evagreen and specific probes were combined. The images of Cy3 and Cy3Fret channels demonstrate negligible background

fluorescence overlap with the Evagreen dye. (B) Two targets were digitized at differing fluorescence ratios, first separately, and then combined. The calculated ratio of the multitarget assay matches that of the references. (C) Melt curves acquired from the two targets enable epiallelic profiling.

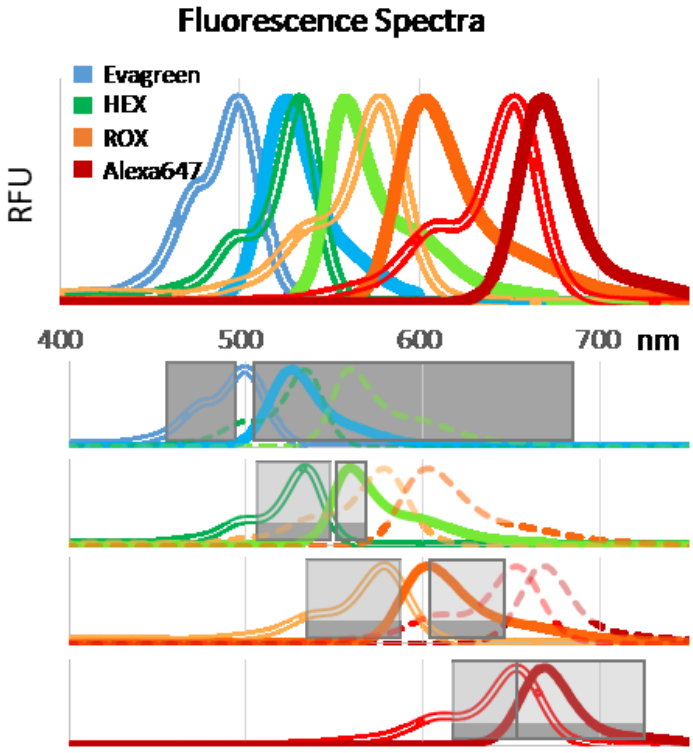

Figure 6.6. 4-Color Imaging Platform

An optical platform was designed to accommodate four non-interfering fluorophores for multiplexed identification. The optimal fluorophores were determined to be Evagreen, HEX, ROX, and Alexa647. Imaging components were designed for minimal fluorescence overlap.

Chapter 7

ANALYSIS OF METHYLATION HETEROGENEITY IN COMPLEX SAMPLES

Challenges and Advances in screening techniques

For almost all cancers, earlier detection leads to a higher chance of survival. To this end, routine screening is highly recommended for cancers that can be detected early, before symptoms arise. For example, the 5-year survival rate of colorectal cancer is 90% when detected in early stages [170]. However, this rate drops to 15-70% if the cancer is diagnosed at a later stage when the cancer has started to spread.

The most sensitive screening test for colorectal cancer is an optical colonoscopy, which detects 95% of colorectal cancers [171]. The US Preventative Services Task Force (USPSTF) recommends that persons over age 50 receive a colonoscopy every 5-10 years. However, adherence to this screening method is hindered by the invasiveness of the

procedure, timeliness, and cost. To address this, many other noninvasive screening methods for colorectal cancer have been proposed and analyzed [171].

Two of the most prominent noninvasive screening tests are the Fecal Immunochemical Test (FIT) and multi-target testing [171], [172]. Both methods involve detection of proteins or genetic and epigenetic markers in noninvasive fluid samples. The multi-target testing, now marketed as Cologuard ®, includes two methylation biomarkers [172]. Such a noninvasive screening method could encourage stronger adherence to routine screening, and, if positive, could serve as an early warning that warrants further tests, such as a colonoscopy. Therefore, there is a need for sensitive technologies to detect rare biomarkers within noninvasive fluids to facilitate routine screening.

One noninvasively collectable sample media that traverses the most surface area and through most other tissues throughout the body is blood. Recently, it has been discovered that all cells release cell-free DNA into the plasma, which retains the characteristics of its source tissue [33]–[35], [42], [173]. Since then, there has been an explosion of research into identifying biomarkers in the blood plasma for many types of cancer, including colorectal cancer [92], [173]–[177]. Of the promising biomarkers that have been identified, many include hypermethylated regions of DNA such as tumor suppressor genes [17], [56], [175]–[181]. We believe that the HYPER-Melt technology could offer improved sensitivity over current techniques. Therefore, we sought to validate the HYPER-Melt technology in complex biological fluids to assess its potential utility for early detection and screening.

Methylation heterogeneity in plasma samples from liquid biopsy

We sought to demonstrate the potential clinical utility of the platform by employing HYPER-Melt for the analysis of methylation heterogeneity of a cfDNA biomarker of colorectal cancer (CRC) from liquid biopsies of cancer-free volunteers compared with patients diagnosed with metastatic CRC (mCRC).We chose to interrogate the methylation patterns of N-Myc downstream-regulated gene 4 (*NDRG4*), which has been implicated in neurite outgrowth and cellular differentiation via the regulation of transcription factors [182], and whose in-tissue clinical sensitivity for CRC is 86% [183], [184]. DREAMing primers for *NDRG4* were designed and optimized to achieve single-copy sensitivity, as previously described [63].

cfDNA from the blood of four cancer-positive patients and four ostensibly healthy volunteers was extracted, purified and underwent bisulfite conversion (Figure 7.1), as detailed elsewhere [63]. Each sample was amplified, melted, and analyzed using the same protocol as described previously [73]. Methylation patterns from each sample are found in Figure 7.2. For comparison, each sample was also assessed for *NDRG4* methylation using quantitative methylation specific PCR (qMSP) [49], [50]. Of the four CRC-positive patients, three of four were clearly positive for *NDRG4* methylation by HYPER-Melt, only one of which showed clear positivity with the *NDRG4* qMSP assay (Figure 7.3). Interestingly, of the four samples from healthy volunteers, one was positive for *NDRG4* methylation by HYPER-Melt, albeit at very low levels of low to intermediate methylation.

From these data, it is readily apparent that HYPER-Melt exhibits both considerably higher analytical sensitivity when compared to qMSP. This is not unexpected, as MSP is

designed to ostensibly only detect fully or very heavily methylated epialleles. In practice, however, most MSP-based assays can still amplify heterogeneously-methylated epialleles, albeit at much lower sensitivity and efficiency. Hence, samples such as CRC 1, that exhibit significant copy numbers of low and medium-density methylation by HYPER-Melt, exhibit weak, non-quantitative positivity by qMSP [185]. In all, HYPER-Melt demonstrated 20-300X or more analytical sensitivity than the qMSP assay in all methylation-positive samples. The greater analytical sensitivity of HYPER-Melt resulted in detection of *NDRG4* methylation in two additional CRC-positive patients (CRC1 and CRC2) that are negative or nearly negative by qMSP. While clearly beneficial in the case of the CRC-positive patients, HYPER-Melt also detected methylation in one of the healthy controls. The presence of very low copy numbers of heterogeneously-methylated *NDRG4* epialleles in sample N1, a 50-year-old male, may be due to natural methylation heterogeneity resulting from early-stage epigenetic drift [110].

In terms of potential clinical use, one of the highly-touted advantages of liquid biopsies is the ability to ostensibly sample overall tumor heterogeneity using a simple blood draw. However, the extremely low copy numbers of circulating tumor DNA (ctDNA) within the overall cfDNA samples, make assessment of this heterogeneity extremely challenging. As a proof of concept, the potential power of our platform was demonstrated by using such liquid biopsy samples. Overall, the considerable dynamic range of the platform allowed ultra-sensitive detection of heterogeneous *NDRG4* epialleles down to 1 in 2 million unmethylated epialleles and in clinical plasma samples at concentrations of less than 150 copies per mL of plasma. HYPER-Melt also demonstrates robustness against multiple samples and targets, providing more information about cfDNA

epiallelic fractions than either MSP or traditional DREAMing while achieving over 100-fold greater sensitivity.

Challenges and Advances in Ovarian Cancer Screening

The most common form of ovarian cancer is high-grade serous carcinoma (HGSOC), which accounts for about ¾ of all ovarian cancers [186], [187]. HGSOC is very aggressive and most often diagnosed in the advanced stages, which may contribute to the low survival rate of 31% [186], [188], [189]. Ultrasound analysis in conjunction with detection of the protein CA-125 has been investigated as a biomarker for early cancer detection; however, the poor specificity of the test resulted in no increased survival probability from screening [188]. Therefore, the USPSTF recommends against this screening method, hence there is currently no screening method available.

In recent studies on the etiology of HGSOC, it has been shown that most carcinomas originate in the fallopian tube as serous tubal intraepithelial carcinomas (STICs) [187], [190]–[192]. However, unlike cancers arising in readily accessible tissues, such as the colon, breast, cervix, and lung, which are amenable to biopsy screening, the fallopian tubes and ovaries are not readily accessible for screening by optical or biopsy methods. The high mortality and incidence rate of this disease have thus prompted many investigations into molecular biomarkers for ovarian and other gynecological cancers.

Cellular migration from the ovary to the uterus is a naturally occurring process during ovulation. Observations of routine Pap specimens have shown that some women

present with abnormal glandular cells. Of these abnormal specimens, more than a third were also shown to have pre-invasive disease as well as invasive carcinomas of nearby tissues such as the ovary, endometrium, and cervix [193]. This has led investigators to hypothesize that tumor-derived cells or DNA could be found in the cells and cervical-vaginal fluid routinely collected in a Pap specimen.

Recently, a new deep sequencing method called "PapSEEK" has been used to interrogate DNA in Pap specimens for mutations specific to ovarian and endometrial cancer [194], [195]. Using a mutation panel, researchers were able to identify tumor-specific mutations in 33-45% of ovarian cancer specimens and 81-93% of endometrial cancers with extremely high sensitivity (>99%) in late stage as well as early stage disease [194], [195]. These promising results indicate routine Pap specimen analysis could be a new avenue for ovarian cancer detection and screening.

Despite the exciting results, the sensitivity toward ovarian cancer remains low, and could benefit from more sensitive detection techniques or biomarkers. Tumor-derived or STIC-derived cells in Pap specimens may be eclipsed by the high background from healthy epithelia, necessitating an extremely sensitive detection technique. Furthermore, many studies have investigated the utility of methylation biomarkers for ovarian cancer detection [196]–[200], and have found much higher prevalence of hypermethylation in tumor suppressor gene panels, even up to 90% sensitivity and 100% specificity in limited cohorts [201]. Recent studies indicate that locus-specific hypermethylation can be identified in HGSOC precursor lesions, STICs [202], indicating the potential for early detection. Moreover, variable methylation could be an even earlier indication of disease

gynecological disease [30], and epigenetic reprogramming is an integral part of ovarian cancer progression [203].

To this end, we applied the HYPER-Melt platform for detection of rare methylated epialleles in DNA acquired from Pap specimens. We identified target loci that were previously reported to demonstrate 100% specificity towards ovarian cancer tissue in a methylation EPIC BeadArray cohort [204]. DREAMing assays were developed for the top performing loci. Finally, the assays were validated on the HYPER-Melt platform, and the clinical utility was validated with Pap specimens from both ovarian cancer and healthy patients, outperforming the gold standard, MSP, in diagnostic performance.

Methylation heterogeneity in Pap Specimens

To identify promising target loci, our collaborators previously performed genome-wide methylation analysis of ovarian cancer using the latest-generation Methylation EPIC BeadArray platform in a cohort of 60 malignant and 36 healthy gynecological mucosal samples [202]. After selecting for 100% specificity, DREAMing assays were developed for the top performing loci and validated for detection of ovarian cancer in a 90-patient tissue cohort, demonstrating 100% sensitivity and specificity. Furthermore, methylation within these loci were detectable in 9 of 9 laser capture microdissected (LCM) ovarian cancer precursor serous tubal intraepithelial carcinoma (STIC) lesions and 0 of 12 LCM cancer-free fallopian tube, suggesting that they are very early events in HGSOC development.

As a proof-of-concept for this project, we developed a DREAMing as well as a qMSP assay for *IRX2*, one of the top performing biomarkers in our initial panel. The DREAMing assay was validated on the HYPER-Melt platform. The platform itself was expanded to accommodate high-throughput sample analysis. Each device consisted of 3 modules, each containing 20,000 1 nanoliter-sized microchambers. Sample preparation, loading, dPCR and dHRM procedures followed those in our previous report [73].

To validate the robustness of the platform to DNA extracted from Pap specimens, we analyzed the methylation heterogeneity of *IRX2* in 3 specimens from HGSOC patients and 6 specimens from matched healthy patients. Heterogeneously methylated DNA was detected and quantified in all of the ovarian cancer patients (Figure 7.4). DNA from the healthy patients was also detected and the patterns identified on the HYPER-Melt platform. To assess the potential clinical utility of the system, we compared the normalized amount of highly methylated DNA per μL for each sample. The HYPER-Melt platform detected overall higher amounts of methylated DNA in the cancer specimens than the healthy for all samples (Figure 7.5). By setting a threshold of 8 copies/ μL, the results demonstrate 100% sensitivity and 100% specificity.

The samples were also asses by the gold standard, qMSP, for fully methylated epialleles. Comparing the results from the two platforms, qMSP identified 1 of 3 samples as positive, and was negative for all of the healthy samples, resulting in 33% sensitivity and 100% specificity (Figure 7.5). The HYPER-Melt platform clearly demonstrates higher sensitivity and more comprehensive analysis than qMSP. These results suggest that

utilization of the HYPER-Melt platform with Pap specimens could greatly improve diagnostic performance over traditional techniques.

Although promising, these results are from a limited sample cohort. Further assessment of the HYPER-Melt platform towards detection of HGSOC from Pap specimen methylation markers is ongoing with a larger patient cohort. The results presented here include data from only one epigenetic marker. If the specificity or sensitivity is challenged in the larger cohort, additional markers could readily be interrogated in the platform to improve clinical performance. Furthermore, the feature-space available within the HYPER-Melt datasets is only just beginning to be explored. Future work may uncover new insights from epiallelic heterogeneity within samples.

Methods

Plasma Samples

All blood samples from patients diagnosed with metastatic colorectal cancer (mCRC) were obtained through a study with approval by the MD Anderson Institutional Review Board, and all participants provided written informed consent (NCT01730586). Blood samples were collected at baseline from mCRC patients prior to clinical trial treatment. Blood samples of cancer-free individuals were obtained from outpatients of Johns Hopkins Community Physicians, with approval by the Johns Hopkins Medicine Institutional Review Board. All participants provided written informed consent. mCRC and cancer-free patient characteristics are provided in Figure 7.1. All blood samples were collected in Cell Preparation Tubes (BD, Franklin Lakes, NJ) and processed within one

hour with centrifugation (3000 g) for 30 minutes and then plasma was aliquoted to 1.8 mL cryovials and stored at -80°C until analysis.

All cfDNA was extracted using 2 ml NeoGeneStar Circulating Cell Free DNA Kit (NeoGeneStar, Somerset, NJ) according to the manufacturer's instructions. Briefly, 2.0 mL of plasma was stabilized with Pretreatment Buffer and then digested in a solution containing 1X Protease Buffer and 100 µl of Proteinase K (Invitrogen). DNA was then extracted with supplied chaotropic salts and washed by a series of magnetic decantation steps and eluted into 20 µl of DNA elution buffer (Zymo Research, Irvine, CA). Extracted cfDNA was quantified by quantitative PCR (qPCR) using primers recognizing β-Globin, Forward Primer: 5'- TGA AGG CTC ATG GCA AGA AAG – 3', Reverse Primer: 5' – GAG GTT GTC CAG GTG AGC CA – 3'. PCR performed using 10X PCR Buffer (ThermoFisher Scientific) to yield a final volume of 25 µl and final working concentration 3.5mM $MgCl_2$, 200µM of each deoxynucleotide triphosphate (dNTP) and 0.04 U/µl of Platinum Taq polymerase (ThermoFisher Scientific). Cycling conditions were 95˚C for 5 minutes, followed by 50 cycles of (95˚C for 5 seconds, 65˚C for 30 seconds and 72˚C for 30 seconds). Standards for quantification were created by serial dilution of human male genomic DNA (Promega). The resulting DNA was bisulfite converted using the EZ DNA Methylation-Lightning Kit (Zymo Research) according to the manufacturer's protocol and eluted into a final volume of 12 µL. Final BST-cfDNA yields were quantified by β-Actin PCR, as described for control DNA above.

Pap Specimens

Pap specimens were collected by collaborators at Johns Hopkins hospital. The specimens were fixated in methanol upon collection. DNA was extracted from the cell

pellet following the NeoGeneStar extraction kit protocol. Next, the samples were bisulfite-converted using the EZ DNA Methylation-Lightning Kit (Zymo Research) according to the manufacturer's protocol and eluted into a final volume of 25 µL. 1-2 µL were used for analysis in MSP, while 7-10 µL were used for analysis on the HYPER-Melt platform.

A

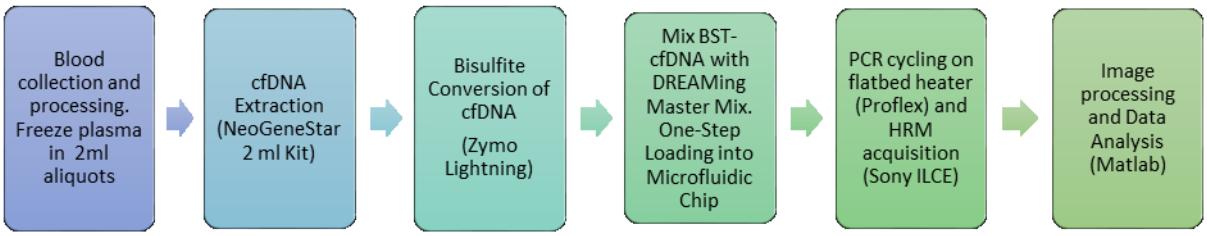

B

Clinical Sample Patient Characteristics

	Normal Patients				CRC Patients			
	N1	N2	N3	N4	CRC 1	CRC 2	CRC 3	CRC 4
Sex	M	M	F	F	M	M	M	M
Age (Mean)	50	34	56	64	76	72	54	65
Race*	C	C	C	AA	C	C	C	C
Cancer Stage					IV	IV	IV	IV
Plasma Volume (ml)	2	2	2	2	2	2	2	2
Plasma DNA concentration (ng/ml)	295	8	5	9	78	670	6.5	275
BST DNA yield (BST Actin Copies)	9.3E+04	2.2E+03	1.5E+03	1.8E+03	5.4E+04	6.9E+05	1.0E+03	8.6E+04

*Race (C-Caucasian, AA-African American, A-Asian, H-Hispanic, O-Other)

Figure 7.1. Clinical Sample Workflow and Patient Characteristics

(A) Workflow from sample collection to HYPER-Melt analysis. (B) Biological information for each patient from whom plasma samples were extracted and analyzed. The plasma volume for each sample collected was 2 mL. Concentration was estimated from BST Actin results.

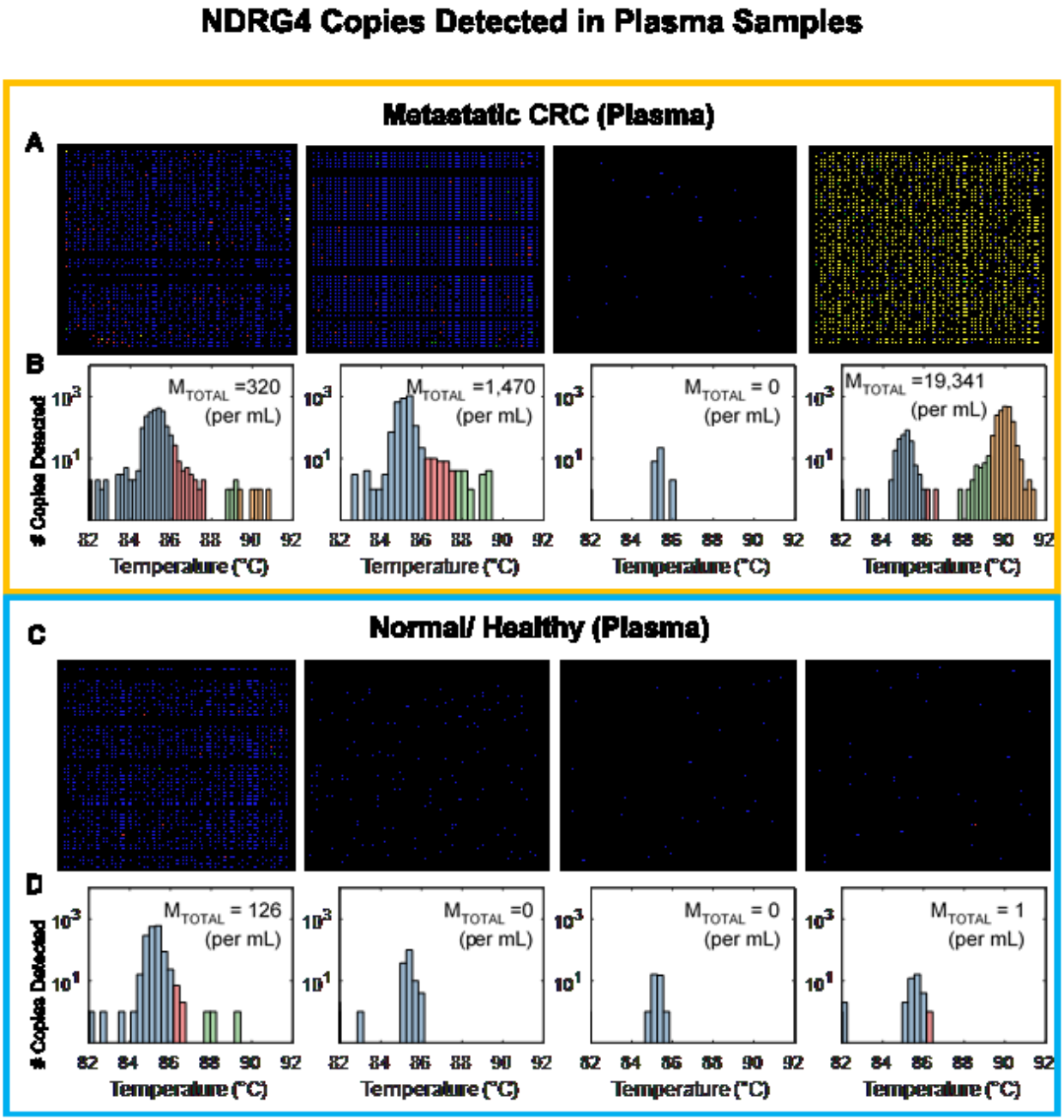

Figure 7.2. NDRG4 Copies Detected in Plasma Samples

HYPER-Melt was performed on plasma from colorectal cancer patients and normal/ healthy samples for the NDRG4 gene. The methylation density of each molecule was classified by melt temperature. (A, B) HYPER-Melt heatmaps and heterogeneity analysis

of copies detected from plasma of colorectal patients (D, E) as wells as healthy volunteers. This figure is reprinted with permission from reference [73].

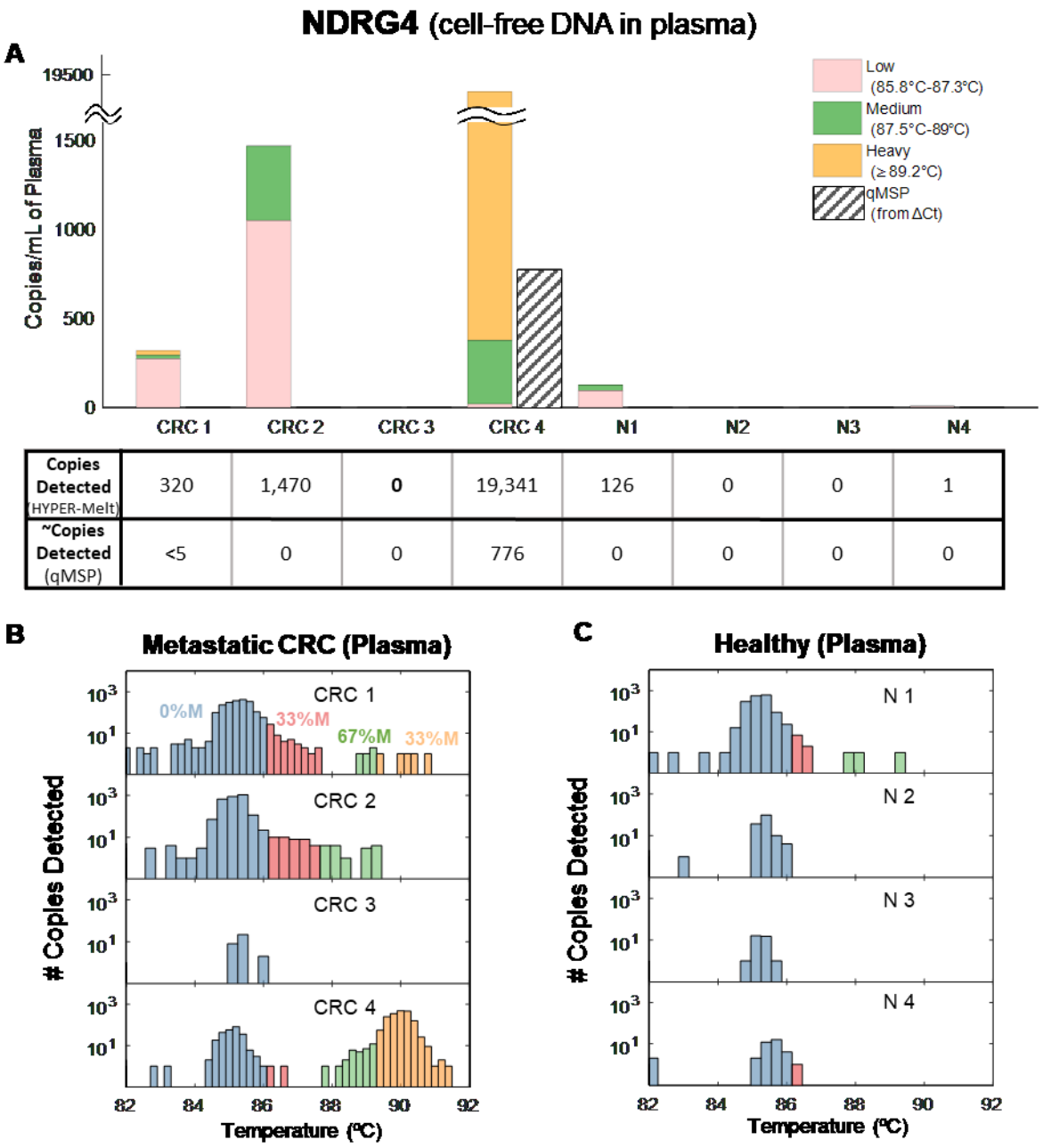

	CRC 1	CRC 2	CRC 3	CRC 4	N1	N2	N3	N4
Copies Detected (HYPER-Melt)	320	1,470	**0**	19,341	126	0	0	1
~Copies Detected (qMSP)	<5	0	0	776	0	0	0	0

Figure 7.3. Liquid Biopsy (cell-free DNA) biomarker detection and analysis via HYPER-Melt.

Methylation data acquired for the NDRG4 locus from DNA extracted from plasma samples from both metastatic colorectal cancer and normal patients. (**A**) Three different levels of methylation density (Low, Medium, Heavy) were identified for each patient via the HYPER-Melt platform. The total number of methylated epialleles detected from each

patient sample was compared to that of the gold standard, MSP. HYPER-Melt histograms show the number of copies detected at each epiallelic fraction from plasma from (**B**) CRC patients and (**C**) healthy volunteers. This figure is reprinted with permission from reference [73].

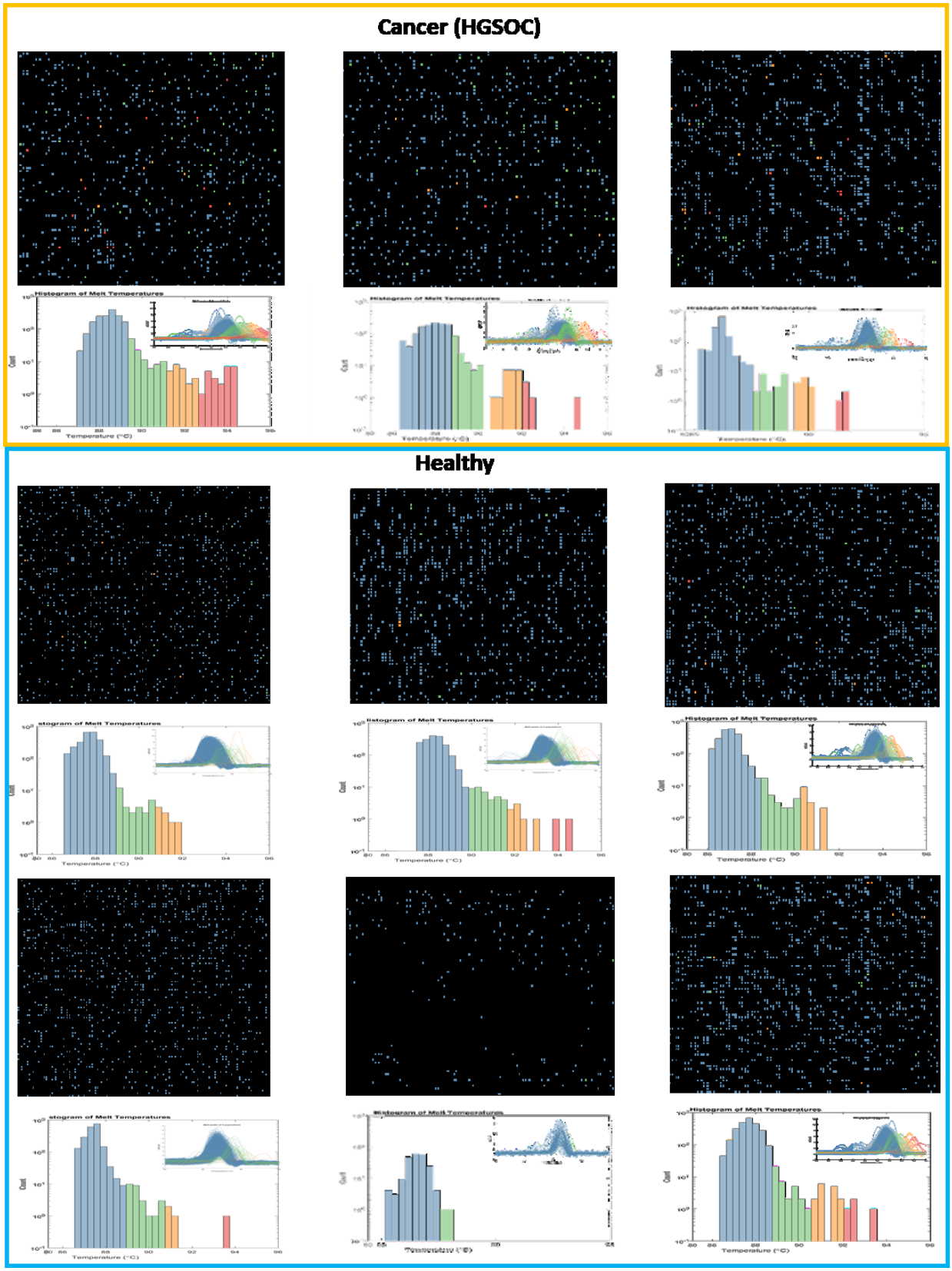
Cancer (HGSOC)
Healthy
Histogram of Melt Temperatures
Count
Temperature (°C)

Figure 7.4. Methylation Heterogeneity in Pap specimens

DNA was extracted from Pap specimens, bisulfite-converted, and interrogated for methylation heterogeneity of *IRX2* on the HYPER-Melt platform. Various levels of DNA methylation could be detected in cancer and in healthy samples.

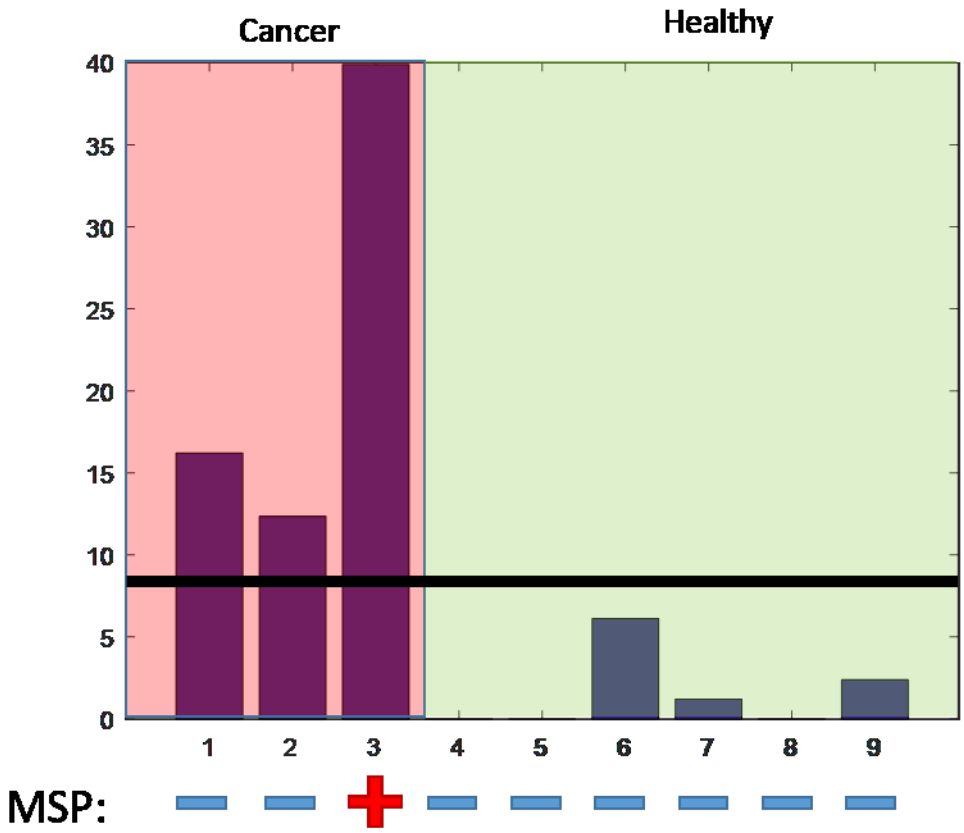

Figure 7.5. Methylated IRX2 in Cancer and Healthy Patients

The amount of heavily methylated DNA in copies/µL was calculated for all patients. Setting a threshold of 8 copies/µL produces 100% sensitivity and 100% specificity. Corresponding MSP results were positive for 1 out of 3 cancer patients.

Chapter 8

CONCLUSION

This dissertation describes the development of a digital microfluidic platform that performs ultra-sensitive intramolecular profiling through highly parallelized real-time analyses. Accessibility and facile operation were key design criteria for this platform, which were incorporated through use of a single-layer microarray design coupled with a simple ultra-thin fabrication protocol. The device can be rapidly loaded and digitized by surface-tension, a facile and scalable method. I demonstrated that this platform, termed HYPER-Melt (High-density Profiling and Enumeration by Melt) is capable of quantifying locus-specific methylation heterogeneity and detection of rare epialleles at fractions as low as 1 in 2,000,000 background molecules, or 0.00005%.

The capabilities of the HYPER-Melt platform were then expanded by increasing the efficiency of target capture as well as the sample throughput. Geometric manipulation of the fluid in a multilayer device improved loading efficiency to 80%. This dissertation

also reports the first demonstration of droplet digital high-resolution melt. I invented a microfluidic pseudo-sieve that achieved 100% efficiency in droplet loading and immobilization of droplets during high-temperature melt analysis. This device can be used in combination with commercial droplet techniques to greatly increase the throughput of epiallelic profiling. Finally, this platform demonstrated robustness towards complex clinical fluids. The HYPER-Melt platform achieved higher sensitivity and more comprehensive analysis in detecting methylation than the gold standard, MSP, in cell-free DNA in plasma as well as with DNA extracted from Pap specimens.

This platform is ideally suited towards applications that require real-time monitoring to identify rare variants, such as circulating biomarker detection, bacterial persistence, antibiotic susceptibility, drug discovery, and directed evolution. Here, the HYPER-Melt platform was applied to the assessment of methylation heterogeneity, a phenomena that occurs early in carcinogenesis but is not yet fully understood. The system resolved methylation differences of 4 CpGs within a locus. Recent studies suggest that changes at this level may have a significant effect on cancer progression. The principle advantages of this platform over current technologies are the high sensitivity for detection of rare molecules, and the simple, economic ability to profile variable sequence patterns. Sequencing remains the most suitable technology for comparing sequence variability in abundant starting material, whereas ddPCR has the fundamentally highest sensitivity towards ultra-rare detection. HYPER-Melt represents a facile profiling technique that combines ultra-high sensitivity with locus-specific sequencing capabilities, designed to be applied towards methylation profiling of a limited number of loci within samples containing scarce or rare biomarkers.

Future work could include efforts to increase the throughput of the device as well as relaxing the device storage requirements. Despite the demonstrated improvements in throughput, the current system is limited in practicality to assessment of 10-20 samples per day. This restriction limits its utility towards assessment of large patient cohorts. Improvements to the optical resolution and thermal uniformity of the platform may increase the capability of the platform to assess hundreds of samples per day, which would much be more attractive for clinical utility. In addition, the current loading method requires the device to be kept under vacuum, which mandates a limited timeframe between atmospheric exposure and loading. Eliminating the need for a vacuum could make the system more robust to a wider variety of users. Such improvements would facilitate more widespread adoption of this technology.

The ultimate long-term goal of this platform is to facilitate early cancer detection through screening for biomarkers in noninvasive fluids. Therefore, future studies should assess large patient cohorts to identify suitable biomarkers or biomarker panels within these fluids. Currently, efforts are ongoing to determine its potential for detection of lung cancer markers in plasma as well as ovarian cancer markers in Pap specimens. Biostatistic analytical tools should be developed to take advantage of the comprehensive datasets provided by the HYPER-Melt platform.

In conclusion, HYPER-Melt provides an all-in-one platform for quantitative molecular profiling and heterogeneity analysis. The platform allows deep insight at the single copy level of any target of interest. Furthermore, the practicality and high digitization power of the platform offers a tool for rapid and efficient DNA sequence

heterogeneity analysis by rapidly interrogating hundreds to thousands of individual molecules in parallel. Overall, this platform has the potential to detect intermolecular variability at ultra-high sensitivity even in difficult and highly-heterogeneous samples, allowing more comprehensive investigation of the dynamics and stochasticity of DNA molecular heterogeneity.

References

[1] B. Vogelstein, N. Papadopoulos, V. E. Velculescu, S. Zhou, L. A. Diaz, and K. W. Kinzler, "Cancer genome landscapes.," *Science*, vol. 339, no. 6127, pp. 1546–58, 2013.

[2] R. Burrell, N. McGranahan, J. Bartek, and C. Swanton, "The causes and consequences of genetic heterogeneity in cancer evolution," *Nature*, vol. 501, 2013.

[3] J. Iranzo, I. Martincorena, and E. V. Koonin, "Cancer-mutation network and the number and specificity of driver mutations," *Proc. Natl. Acad. Sci. U. S. A.*, vol. 115, no. 26, pp. E6010–E6019, Jun. 2018.

[4] H. Easwaran, H. C. Tsai, and S. B. Baylin, "Cancer Epigenetics: Tumor Heterogeneity, Plasticity of Stem-like States, and Drug Resistance," *Molecular Cell*, vol. 54, no. 5. pp. 716–727, 2014.

[5] S. B. Baylin and P. A. Jones, "Epigenetic determinants of cancer," *Cold Spring Harb. Perspect. Biol.*, vol. 8, no. 9, pp. 1–36, 2016.

[6] W. A. Flavahan, E. Gaskell, and B. E. Bernstein, "Epigenetic plasticity and the hallmarks of cancer," *Science*, vol. 357, no. 6348. 2017.

[7] S. Negrini, V. G. Gorgoulis, and T. D. Halazonetis, "Genomic instability — an evolving hallmark of cancer," *Nat. Rev. Mol. Cell Biol.*, vol. 11, no. 3, pp. 220–228, Mar. 2010.

[8] J. Sandoval and M. Esteller, "Cancer epigenomics: Beyond genomics," *Current Opinion in Genetics and Development*, vol. 22, no. 1. pp. 50–55, 2012.

[9] A. Portela and M. Esteller, "Epigenetic modifications and human disease," *Nat. Publ. Gr.*, vol. 28, 2010.

[10] J. D. Choi and J.-S. Lee, "Interplay between Epigenetics and Genetics in Cancer," *Genomics Inform.*, vol. 11, no. 4, p. 164, 2013.

[11] M. A. Dawson and T. Kouzarides, "Cancer Epigenetics: From Mechanism to Therapy," *Cell*, vol. 150, pp. 12–27, 2012.

[12] V. Santini, H. M. Kantarjian, and J.-P. Issa, "Changes in DNA Methylation in Neoplasia: Pathophysiology and Therapeutic Implications," *Ann. Intern. Med.*, vol. 134, no. 7, p. 573, Apr. 2001.

[13] M. Esteller, "Molecular Origins of Cancer Epigenetics in Cancer," *N Engl J Med*, vol. 358, pp. 1148–59, 2008.

[14] M. Szyf, "DNA methylation and cancer therapy," *Drug Resistance Updates*, vol. 6, no. 6. pp. 341–353, 2003.

[15] J. G. Herman and S. B. Baylin, "Gene Silencing in Cancer in Association with Promoter Hypermethylation," *n engl j med*, vol. 34921349, pp. 2042–54, 2003.

[16] P. a Jones and S. B. Baylin, "The fundamental role of epigenetic events in cancer.," *Nat. Rev. Genet.*, vol. 3, no. 6, pp. 415–28, 2002.

[17] S. A. Belinsky, "Gene-promoter hypermethylation as a biomarker in lung cancer," *Nat. Rev. Cancer*, vol. 4, no. 9, pp. 707–717, 2004.

[18] S. B. Baylin and J. E. Ohm, "Epigenetic gene silencing in cancer - A mechanism for early

oncogenic pathway addiction?," *Nat. Rev. Cancer*, vol. 6, no. 2, pp. 107–116, 2006.
[19] T. E. Bartlett *et al.*, "Epigenetic reprogramming of fallopian tube fimbriae in BRCA mutation carriers defines early ovarian cancer evolution," *Nat. Commun.*, 2016.
[20] A. E. Teschendorff *et al.*, "Epigenetic variability in cells of normal cytology is associated with the risk of future morphological transformation," *Genome Med.*, vol. 4, no. 3, 2012.
[21] A. E. Teschendorff *et al.*, "DNA methylation outliers in normal breast tissue identify field defects that are enriched in cancer," *Nat. Commun.*, 2016.
[22] A. P. Feinberg and B. Tycko, "The history of cancer epigenetics," *Nat. Rev. Cancer*, vol. 4, no. 2, pp. 143–153, 2004.
[23] H. Suzuki *et al.*, "Epigenetic inactivation of SFRP genes allows constitutive WNT signaling in colorectal cancer," *Nat. Genet.*, vol. 36, no. 4, pp. 417–422, Apr. 2004.
[24] H. S. Melkonyan *et al.*, "SARPs: A family of secreted apoptosis-related proteins (cloningsecreted proteinsfrizzled homologue)," 1997.
[25] P. B. Gupta *et al.*, "Stochastic state transitions give rise to phenotypic equilibrium in populations of cancer cells.," *Cell*, vol. 146, no. 4, pp. 633–44, Aug. 2011.
[26] D. A. Landau *et al.*, "Locally Disordered Methylation Forms the Basis of Intratumor Methylome Variation in Chronic Lymphocytic Leukemia," *Cancer Cell*, vol. 26, no. 6, pp. 813–825, Dec. 2014.
[27] N. C. Sheffield *et al.*, "DNA methylation heterogeneity defines a disease spectrum in Ewing sarcoma," *Nat. Med.*, vol. 23, no. 3, pp. 386–395, 2017.
[28] S. Li *et al.*, "Distinct evolution and dynamics of epigenetic and genetic heterogeneity in acute myeloid leukemia," *Nat. Med.*, vol. 22, pp. 792–799, 2016.
[29] W. Timp and A. P. Feinberg, "Cancer as a dysregulated epigenome allowing cellular growth advantage at the expense of the host," *Nat. Rev. Cancer*, vol. 13, no. 7, pp. 497–510, Jun. 2013.
[30] A. E. Teschendorff *et al.*, "The Dynamics of DNA Methylation Covariation Patterns in Carcinogenesis," *PLoS Comput. Biol.*, vol. 10, no. 7, 2014.
[31] A. E. Teschendorff and M. Widschwendter, "Differential variability improves the identification of cancer risk markers in DNA methylation studies profiling precursor cancer lesions," *Bioinformatics*, vol. 28, no. 11, pp. 1487–1494, 2012.
[32] H. H. McAdams and A. Arkin, "It's a noisy business! Genetic regulation at the nanomolar scale," *Trends in Genetics*, vol. 15, no. 2. pp. 65–69, 1999.
[33] L. A. Diaz and A. Bardelli, "Liquid Biopsies: Genotyping Circulating Tumor DNA," *J. Clin. Oncol.*, vol. 32, no. 6, pp. 579–586, Feb. 2014.
[34] C. D. M. Campos, J. M. Jackson, M. A. Witek, and S. A. Soper, "Molecular Profiling of Liquid Biopsy Samples for Precision Medicine," *Cancer J.*, vol. 24, no. 2, pp. 93–103, 2018.
[35] D. A. Haber and V. E. Velculescu, "Blood-based analyses of cancer: circulating tumor cells and circulating tumor DNA.," *Cancer Discov.*, vol. 4, no. 6, pp. 650–61, Jun. 2014.
[36] P. Podlesniy and R. Trullas, "Biomarkers in cerebrospinal fluid: Analysis of cell-free circulating mitochondrial dna by digital PCR," in *Methods in Molecular Biology*, vol. 1768, Humana Press, New York, NY, 2018, pp. 111–126.
[37] L. Gorgannezhad, M. Umer, M. N. Islam, N.-T. Nguyen, and M. J. A. Shiddiky, "Circulating tumor DNA and liquid biopsy: opportunities, challenges, and recent advances in detection technologies," *Lab Chip*, vol. 18, p. 1174, 2018.
[38] A. Agarwal, M. Balic, D. El-Ashry, and R. J. Cote, "Circulating Tumor Cells: Strategies for Capture, Analyses, and Propagation," *Cancer Journal (United States)*, vol. 24, no. 2. pp. 70–77, 2018.

[39] M. Chimonidou *et al.*, “DNA methylation of tumor suppressor and metastasis suppressor genes in circulating tumor cells.,” *Clin. Chem.*, vol. 57, no. 8, pp. 1169–77, Aug. 2011.
[40] T. Forshew *et al.*, “Noninvasive Identification and Monitoring of Cancer Mutations by Targeted Deep Sequencing of Plasma DNA,” *Sci. Transl. Med.*, vol. 4, no. 136, p. 136ra68, 2012.
[41] D. T. Miyamoto, D. T. Ting, M. Toner, S. Maheswaran, and D. A. Haber, “Single-Cell Analysis of Circulating Tumor Cells as a Window into Tumor Heterogeneity.,” *Cold Spring Harb. Symp. Quant. Biol.*, vol. 81, pp. 269–274, Jan. 2016.
[42] E. Crowley, F. Di Nicolantonio, F. Loupakis, and A. Bardelli, “Liquid biopsy: monitoring cancer-genetics in the blood,” *Nat. Rev. Clin. Oncol.*, vol. 10, no. 8, pp. 472–484, 2013.
[43] X. Han, J. Wang, and Y. Sun, “Circulating Tumor DNA as Biomarkers for Cancer Detection,” *Genomics, Proteomics and Bioinformatics*, vol. 15, no. 2. pp. 59–72, 2017.
[44] M. Ignatiadis, M. Lee, and S. S. Jeffrey, “Circulating tumor cells and circulating tumor DNA: Challenges and opportunities on the path to clinical utility,” *Clinical Cancer Research*, vol. 21, no. 21. pp. 4786–4800, 2015.
[45] H. Schwarzenbach, D. S. . B. Hoon, and K. Pantel, “Cell-free nucleic acids as biomarkers in cancer patients.,” *Nat. Rev. Cancer*, vol. 11, no. 6, pp. 426–37, 2011.
[46] G. Sharma, S. Mirza, C. P. Prasad, A. Srivastava, S. D. Gupta, and R. Ralhan, “Promoter hypermethylation of p16INK4A, p14ARF, CyclinD2 and Slit2 in serum and tumor DNA from breast cancer patients,” *Life Sci.*, vol. 80, no. 20, pp. 1873–1881, 2007.
[47] T. Xu *et al.*, “Cross-Platform Comparison of Four Leading Technologies for Detecting EGFR Mutations in Circulating Tumor DNA from Non-Small Cell Lung Carcinoma Patient Plasma,” *Theranostics*, vol. 7, no. 76, pp. 1437–1446, 2017.
[48] P. Ulz, E. Heitzer, J. B. Geigl, and M. R. Speicher, “Patient monitoring through liquid biopsies using circulating tumor DNA,” *Int. J. Cancer*, vol. 141, no. 5, pp. 887–896, May 2017.
[49] J. G. Herman, J. R. Graff, S. Myohanen, B. D. Nelkin, and S. B. Baylin, “Methylation-specific PCR: a novel PCR assay for methylation status of CpG islands.,” *Proc. Natl. Acad. Sci.*, vol. 93, no. 18, pp. 9821–9826, 1996.
[50] C. A. Eads *et al.*, “MethyLight: a high-throughput assay to measure DNA methylation,” *Nucleic Acids Res.*, vol. 28, no. 8, p. e32, 2000.
[51] M. Zeschnigk, S. Böhringer, E. A. Price, Z. Onadim, L. Masshöfer, and D. R. Lohmann, “A novel real-time PCR assay for quantitative analysis of methylated alleles (QAMA): analysis of the retinoblastoma locus.,” *Nucleic Acids Res.*, 2004.
[52] C. A. Eads, “MethyLight: a high-throughput assay to measure DNA methylation,” *Nucleic Acids Res.*, 2000.
[53] T. Mikeska, C. Bock, H. Do, and A. Dobrovic, “DNA methylation biomarkers in cancer: progress towards clinical implementation,” *Expert Rev. Mol. Diagn.*, vol. 12, no. 5, pp. 473–487, 2012.
[54] C. Alkan, S. Sajjadian, and E. E. Eichler, “Limitations of next-generation genome sequence assembly,” *Nature Methods*. 2011.
[55] N. Rieber *et al.*, “Coverage Bias and Sensitivity of Variant Calling for Four Whole-genome Sequencing Technologies,” *PLoS One*, 2013.
[56] M. Li *et al.*, “Sensitive digital quantification of DNA methylation in clinical samples,” *Nat. Biotechnol.*, vol. 27, no. 9, pp. 858–863, Sep. 2009.
[57] M. Yu *et al.*, “Methylight droplet digital PCR for detection and absolute quantification of infrequently methylated alleles,” *Epigenetics*, 2015.

[58] L. Labanieh, T. N. Nguyen, W. Zhao, and D. K. Kang, “Floating droplet array: An ultrahigh-throughput device for droplet trapping, real-time analysis and recovery,” *Micromachines*, vol. 6, no. 10, pp. 1469–1482, 2015.
[59] X. Bian *et al.*, “A microfluidic droplet digital PCR for simultaneous detection of pathogenic Escherichia coli O157 and Listeria monocytogenes,” *Biosens. Bioelectron.*, vol. 74, pp. 770–777, 2015.
[60] D. A. Selck and R. F. Ismagilov, “Instrument for real-time digital nucleic acid amplification on custom microfluidic devices,” *PLoS One*, vol. 11, no. 10, 2016.
[61] D. O. Velez *et al.*, “Massively parallel digital high resolution melt for rapid and absolutely quantitative sequence profiling,” *Sci. Rep.*, vol. 7, p. 42326, Feb. 2017.
[62] Y. Shimazaki, J. Tanaka, Y. Kohara, M. Kamahori, and T. Sakamoto, “Parallel Evaluation of Melting Temperatures of DNAs in the Arrayed Droplets through the Fluorescence from DNA Intercalators,” *Anal. Chem.*, vol. 89, no. 12, pp. 6305–6308, 2017.
[63] T. R. Pisanic *et al.*, “DREAMing: a simple and ultrasensitive method for assessing intratumor epigenetic heterogeneity directly from liquid biopsies.,” *Nucleic Acids Res.*, vol. 43, no. 22, p. e154, Dec. 2015.
[64] A. M. Kaushik, K. Hsieh, and T.-H. Wang, “Droplet microfluidics for high-sensitivity and high-throughput detection and screening of disease biomarkers,” *Wiley Interdiscip. Rev. Nanomedicine Nanobiotechnology*, p. e1522, May 2018.
[65] A. B. Theberge *et al.*, “Microdroplets in microfluidics: An evolving platform for discoveries in chemistry and biology,” *Angew. Chemie - Int. Ed.*, vol. 49, no. 34, pp. 5846–5868, 2010.
[66] Y. Ding, J. Choo, and A. J. DeMello, “From single-molecule detection to next-generation sequencing: microfluidic droplets for high-throughput nucleic acid analysis,” *Microfluid. Nanofluidics*, vol. 21, no. 3, p. 58, 2017.
[67] T. W. Murphy, Q. Zhang, L. B. Naler, S. Ma, and C. Lu, “Recent advances in the use of microfluidic technologies for single cell analysis,” *Analyst*, vol. 143, no. 1. pp. 60–80, 2018.
[68] K. Choi, A. H. C. Ng, R. Fobel, and A. R. Wheeler, “Digital Microfluidics,” *Annu. Rev. Anal. Chem. is online Annu. Rev. Anal. Chem*, vol. 5, pp. 413–440, 2012.
[69] K. a Heyries *et al.*, “Megapixel digital PCR.,” *Nat. Methods*, vol. 8, no. 8, pp. 649–651, 2011.
[70] Q. Zhu *et al.*, “Digital PCR on an integrated self-priming compartmentalization chip,” *Lab Chip*, vol. 14, no. 6, pp. 1176–1185, 2014.
[71] H. Zec, C. O’Keefe, P. Ma, and T. Wang, “Ultra-Thin, Evaporation-Resistent Pdms-Devices for Absolute Quantification of Dna Using Digital Pcr,” *Transducers*, pp. 536–539, 2015.
[72] J.-Y. Cheng, C.-J. Hsieh, Y.-C. Chuang, and J.-R. Hsieh, “Performing microchannel temperature cycling reactions using reciprocating reagent shuttling along a radial temperature gradient,” 2005.
[73] C. M. O’Keefe, T. R. Pisanic, H. Zec, M. J. Overman, J. G. Herman, and T. H. Wang, “Facile profiling of molecular heterogeneity by microfluidic digital melt,” *Sci. Adv.*, vol. 4, no. 9, pp. 6459–6485, 2018.
[74] D. P. Cahill, K. W. Kinzler, B. Vogelstein, and C. Lengauer, “Genetic instability and darwinian selection in tumours,” *Trends in Biochemical Sciences*, vol. 24, no. 12. 1999.
[75] J. W. Pepper, C. Scott Findlay, R. Kassen, S. L. Spencer, and C. C. Maley, “Cancer research meets evolutionary biology.,” *Evol. Appl.*, vol. 2, no. 1, pp. 62–70, Feb. 2009.
[76] P. D. Sniegowski, P. J. Gerrish, and R. E. Lenski, “Evolution of high mutation rates in experimental populations of E. coli,” *Nature*, vol. 387, no. 6634, pp. 703–705, Jun. 1997.
[77] E. Kussell, “Phenotypic Diversity, Population Growth, and Information in Fluctuating

Environments," *Science (80-.).*, vol. 309, no. 5743, pp. 2075–2078, Sep. 2005.
[78] M. Acar, J. T. Mettetal, and A. van Oudenaarden, "Stochastic switching as a survival strategy in fluctuating environments," *Nat. Genet.*, vol. 40, no. 4, pp. 471–475, Apr. 2008.
[79] A. Eldar and M. B. Elowitz, "Functional roles for noise in genetic circuits.," *Nature*, vol. 467, no. 7312, pp. 167–73, Sep. 2010.
[80] R. A. Burrell, N. McGranahan, J. Bartek, and C. Swanton, "The causes and consequences of genetic heterogeneity in cancer evolution," *Nature*. 2013.
[81] A. Goriely, G. A. T. Mcvean, M. Röjmyr, B. Ingemarsson, and A. O. M. Wilkie, "Evidence for Selective Advantage of Pathogenic FGFR2 Mutations in the Male Germ Line," 2003.
[82] R. L. Siegel, K. D. Miller, and A. Jemal, "Cancer statistics, 2016," *CA. Cancer J. Clin.*, vol. 66, no. 1, pp. 7–30, Jan. 2016.
[83] K. Ririe, R. Rasmussen, and C. Wittwer, "Product differentiation by analysis of DNA melting curves during the polymerase chain reaction," *Anal. Biochem.*, vol. 245, pp. 154–160, 1997.
[84] P. Yakovchuk, E. Protozanova, and M. D. Frank-Kamenetskii, "Base-stacking and base-pairing contributions into thermal stability of the DNA double helix," *Nucleic Acids Res.*, vol. 34, no. 2, pp. 564–574, Jan. 2006.
[85] Y. Zhang, Y. Zhu, B. Yao, and Q. Fang, "Nanolitre droplet array for real time reverse transcription polymerase chain reaction," *Lab Chip*, vol. 11, no. 8, p. 1545, 2011.
[86] H.-B. Liu, N. Ramalingam, Y. Jiang, C.-C. Dai, K. M. Hui, and H.-Q. Gong, "Rapid distribution of a liquid column into a matrix of nanoliter wells for parallel real-time quantitative PCR," *Sensors Actuators B*, vol. 135, pp. 671–677, 2009.
[87] T. Morrison *et al.*, "Nanoliter high throughput quantitative PCR," *Nucleic Acids Res.*, vol. 34, no. 18, 2006.
[88] H. Ma, K. Y. Horiuchi, Y. Wang, S. A. Kucharewicz, and S. L. Diamond, "Nanoliter Homogenous Ultra-High Throughput Screening Microarray for Lead Discoveries and IC 50 Profiling," *Assay Drug Dev. Technol.*, vol. 3, no. 2, 2005.
[89] N. R. Beer *et al.*, "On-chip single-copy real-time reverse-transcription PCR in isolated picoliter droplets," *Anal. Chem.*, vol. 80, no. 6, pp. 1854–1858, 2008.
[90] Y. Chen, J. D. Müller, P. T. C. So, and E. Gratton, "The Photon Counting Histogram in Fluorescence Fluctuation Spectroscopy," *Biophys. J.*, vol. 77, no. 1, pp. 553–567, Jul. 1999.
[91] M. J. Woods RP, Grafton ST, Watson JDG, Sicotte NL, "Automated image registration: II. Intersubject validation of linear and nonlinear models.," *J. Comput. Assist. Tomogr.*, vol. 2, pp. 153–165, 1998.
[92] F. Diehl *et al.*, "Detection and quantification of mutations in the plasma of patients with colorectal tumors," *Proc. Natl. Acad. Sci.*, vol. 102, no. 45, pp. 16368–16373, 2005.
[93] Z. Dwight, R. Palais, and C. T. Wittwer, "uMELT: prediction of high-resolution melting curves and dynamic melting profiles of PCR products in a rich web application," *Bioinformatics*, vol. 27, no. 7, pp. 1019–1020, Apr. 2011.
[94] N. Amirouchene-Angelozzi, C. Swanton, and A. Bardelli, "Tumor evolution as a therapeutic target," *Cancer Discovery*, vol. 7, no. 8. pp. 805–817, 2017.
[95] A. N. Abou Tayoun, P. R. Burchard, A. M. Caliendo, A. Scherer, and G. J. Tsongalis, "A multiplex PCR assay for the simultaneous detection of Chlamydia trachomatis, Neisseria gonorrhoeae, and Trichomonas vaginalis," *Exp. Mol. Pathol.*, vol. 98, no. 2, pp. 214–218, 2015.
[96] J. Gonzalez-Bosquet *et al.*, "Detection of Somatic Mutations by High-Resolution DNA Melting (HRM) Analysis in Multiple Cancers," *PLoS One*, vol. 6, no. 1, p. e14522, Jan. 2011.

[97] G. H. Reed and C. T. Wittwer, “Sensitivity and specificity of single-nucleotide polymorphism scanning by high-resolution melting analysis.,” *Clin. Chem.*, vol. 50, no. 10, pp. 1748–54, Oct. 2004.
[98] K. Osafune *et al.*, “Marked differences in differentiation propensity among human embryonic stem cell lines.”
[99] B. Keeley *et al.*, “Extraction and processing of circulating DNA from large sample volumes using methylation on beads for the detection of rare epigenetic events,” *Clin. Chim. Acta*, vol. 425, pp. 169–175, Oct. 2013.
[100] Y. Fu *et al.*, “A microfluidic chip based on surfactant-doped polydimethylsiloxane (PDMS) in a sandwich configuration for low-cost and robust digital PCR,” *Sensors Actuators B Chem.*, vol. 245, pp. 414–422, Jun. 2017.
[101] A. M. Thompson *et al.*, “Self-digitization chip for single-cell genotyping of cancer-related mutations,” *PLoS One*, vol. 13, no. 5, p. e0196801, May 2018.
[102] I. Garcia-Murillas *et al.*, “Mutation tracking in circulating tumor DNA predicts relapse in early breast cancer,” *Sci. Transl. Med.*, vol. 7, no. 302, 2015.
[103] H. Boukellal, E. Selimović, Y. Jia, G. Cristobal, and S. Fraden, “Simple, robust storage of drops and fluids in a microfluidic device,” *Lab Chip*, vol. 9, no. 2, pp. 331–338, 2009.
[104] T. Schneider, G. S. Yen, A. M. Thompson, D. R. Burnham, and D. T. Chiu, “Self-digitization of samples into a high-density microfluidic bottom-well array,” *Anal. Chem.*, vol. 85, no. 21, pp. 10417–10423, 2013.
[105] Q. Zhu *et al.*, “Lab on a Chip A scalable self-priming fractal branching microchannel net chip for digital PCR †,” vol. 17, p. 1655, 2017.
[106] S. W. Lee and S. S. Lee, “Shrinkage ratio of PDMS and its alignment method for the wafer level process,” *Microsyst. Technol.*, vol. 14, no. 2, pp. 205–208, Oct. 2007.
[107] C. Moraes, Y. Sun, and C. A. Simmons, “Solving the shrinkage-induced PDMS alignment registration issue in multilayer soft lithography,” *J. Micromechanics Microengineering*, vol. 19, p. 6, 2009.
[108] J. S. Marcus, W. F. Anderson, and S. R. Quake, “Microfluidic single-cell mRNA isolation and analysis,” *Anal. Chem.*, vol. 78, no. 9, pp. 3084–3089, 2006.
[109] M. Esteller *et al.*, “Hypermethylation-associated Inactivation of p14 ARF Is Independent of p16 INK4a Methylation and p53 Mutational Status 1,” *CANCER Res.*, vol. 60, pp. 129–133, 2000.
[110] T. R. Pisanic, P. Athamanolap, and T. H. Wang, “Defining, distinguishing and detecting the contribution of heterogeneous methylation to cancer heterogeneity,” *Seminars in Cell and Developmental Biology*, vol. 64. pp. 5–17, 2017.
[111] C. M. O’Keefe, D. Giammanco, S. Li, T. R. Pisanic, and T. H. J. Wang, “Multilayer microfluidic array for highly efficient sample loading and digital melt analysis of DNA methylation,” *Lab Chip*, 2019.
[112] D. Pekin *et al.*, “Quantitative and sensitive detection of rare mutations using droplet-based microfluidics,” *Lab Chip*, vol. 11, no. 13, pp. 2156–2166, 2011.
[113] V. Yelleswarapu, J. R. Buser, M. Haber, J. Baron, E. Inapuri, and D. Issadore, “Mobile platform for rapid sub–picogram-per-milliliter, multiplexed, digital droplet detection of proteins,” *Proc. Natl. Acad. Sci.*, vol. 116, no. 10, pp. 4489–4495, 2019.
[114] J. Shuga *et al.*, “Single molecule quantitation and sequencing of rare translocations using microfluidic nested digital PCR,” *Nucleic Acids Res.*, vol. 41, no. 16, pp. 1–11, 2013.
[115] H. Zec, D. J. Shin, and T.-H. Wang, “Novel droplet platforms for the detection of disease biomarkers,” *Expert Rev. Mol. Diagn.*, vol. 14, no. 7, pp. 787–801, Sep. 2014.

[116] S. Y. Teh, R. Lin, L. H. Hung, and A. P. Lee, “Droplet microfluidics,” *Lab on a Chip*, vol. 8, no. 2. pp. 198–220, 2008.
[117] L. M. Boettger, R. E. Handsaker, M. C. Zody, and S. A. McCarroll, “Structural haplotypes and recent evolution of the human 17q21.31 region,” *Nat. Genet.*, vol. 44, no. 8, pp. 881–885, Aug. 2012.
[118] L. Miotke, B. T. Lau, R. T. Rumma, and H. P. Ji, “High sensitivity detection and quantitation of DNA copy number and single nucleotide variants with single color droplet digital PCR,” *Anal. Chem.*, vol. 86, no. 5, pp. 2618–2624, Mar. 2014.
[119] J. Beck *et al.*, “Genome Aberrations in Canine Mammary Carcinomas and Their Detection in Cell-Free Plasma DNA,” *PLoS One*, vol. 8, no. 9, p. e75485, Sep. 2013.
[120] J. A. Beaver *et al.*, “Detection of Cancer DNA in Plasma of Patients with Early-Stage Breast Cancer,” *Clin. Cancer Res.*, vol. 20, no. 10, pp. 2643–2650, May 2014.
[121] G. Zhu *et al.*, “Highly Sensitive Droplet Digital PCR Method for Detection of EGFR-Activating Mutations in Plasma Cell–Free DNA from Patients with Advanced Non–Small Cell Lung Cancer,” *J. Mol. Diagnostics*, vol. 17, no. 3, pp. 265–272, May 2015.
[122] H.-G. Goh *et al.*, “Sensitive quantitation of minimal residual disease in chronic myeloid leukemia using nanofluidic digital polymerase chain reaction assay,” *Leuk. Lymphoma*, vol. 52, no. 5, pp. 896–904, May 2011.
[123] J. B. Jackson, D. S. Choi, J. D. Luketich, A. Pennathur, A. Ståhlberg, and T. E. Godfrey, “Multiplex Preamplification of Serum DNA to Facilitate Reliable Detection of Extremely Rare Cancer Mutations in Circulating DNA by Digital PCR.,” *J. Mol. Diagn.*, vol. 18, no. 2, pp. 235–43, Mar. 2016.
[124] P. S. Mitchell *et al.*, “Circulating microRNAs as stable blood-based markers for cancer detection,” *Proc. Natl. Acad. Sci.*, vol. 105, no. 30, pp. 10513–10518, Jul. 2008.
[125] G. P. McDermott *et al.*, “Multiplexed Target Detection Using DNA-Binding Dye Chemistry in Droplet Digital PCR,” *Anal. Chem.*, vol. 85, no. 23, pp. 11619–11627, Dec. 2013.
[126] I. C. Gilg *et al.*, “Differential gene expression is tied to photo chemical efficiency reduction in virally infected Emiliania huxleyi,” *Mar. Ecol. Prog. Ser.*, vol. 555, pp. 13–27, 2016.
[127] A. D. Tadmor, E. A. Ottesen, J. R. Leadbetter, and R. Phillips, “Probing Individual Environmental Bacteria for Viruses by Using Microfluidic Digital PCR,” *Science (80-.).*, vol. 333, no. 6038, pp. 58–62, Jul. 2011.
[128] S. Pholwat, S. Stroup, S. Foongladda, and E. Houpt, “Digital PCR to Detect and Quantify Heteroresistance in Drug Resistant Mycobacterium tuberculosis,” *PLoS One*, vol. 8, no. 2, p. e57238, Feb. 2013.
[129] F. Schuler *et al.*, “Digital droplet PCR on disk,” *Lab Chip*, vol. 16, no. 1, pp. 208–216, 2016.
[130] X. Leng and C. J. Yang, “Agarose droplet microfluidics for highly parallel and efficient single molecule emulsion PCR.,” *Methods Mol. Biol.*, vol. 949, no. 21, pp. 413–422, 2013.
[131] B. J. Hindson *et al.*, “High-throughput droplet digital PCR system for absolute quantitation of DNA copy number,” *Anal. Chem.*, vol. 83, no. 22, pp. 8604–8610, 2011.
[132] J. Chen *et al.*, “Capillary-based integrated digital PCR in picoliter droplets,” *Lab Chip*, vol. 18, no. 3, pp. 412–421, 2018.
[133] S. I. Fraley *et al.*, “Universal digital high-resolution melt: a novel approach to broad-based profiling of heterogeneous biological samples,” *Nucleic Acids Res.*, vol. 41, no. 18, pp. e175–e175, Oct. 2013.
[134] N. Andini *et al.*, “Microbial Typing by Machine Learned DNA Melt Signatures,” *Sci. Rep.*, vol. 7, p. 42097, Feb. 2017.
[135] P. Athamanolap *et al.*, “Trainable High Resolution Melt Curve Machine Learning Classifier

for Large-Scale Reliable Genotyping of Sequence Variants," *PLoS One*, vol. 9, no. 10, p. e109094, Oct. 2014.
[136] E. L. Jackson-Holmes, T. C. McDevitt, and H. Lu, "A microfluidic trap array for longitudinal monitoring and multi-modal phenotypic analysis of individual stem cell aggregates," *Lab Chip*, vol. 17, no. 21, pp. 3634–3642, 2017.
[137] C. L. Hansen *et al.*, "High-throughput analysis of single hematopoietic stem cell proliferation in microfluidic cell culture arrays," *Nat. Methods*, 2011.
[138] S. L. Sjostrom, H. N. Joensson, and H. A. Svahn, "Multiplex analysis of enzyme kinetics and inhibition by droplet microfluidics using picoinjectors3," vol. 13, p. 1754, 2013.
[139] C. H. J. Schmitz, A. C. Rowat, S. Köster, and D. A. Weitz, "Dropspots: a picoliter array in a microfluidic device," *Lab Chip*, vol. 9, no. 1, pp. 44–49, 2009.
[140] S. S. Terekhov *et al.*, "Microfluidic droplet platform for ultrahigh-throughput single-cell screening of biodiversity," *Proc. Natl. Acad. Sci.*, vol. 114, no. 10, pp. 2550–2555, 2017.
[141] Z. Hua *et al.*, "Multiplexed Real-Time Polymerase Chain Reaction on a Digital Microfluidic Platform," *Anal. Chem*, vol. 82, no. 6, pp. 2310–2316, 2010.
[142] D. A. Selck and R. F. Ismagilov, "Instrument for real-time digital nucleic acid amplification on custom microfluidic devices," *PLoS One*, vol. 11, no. 10, pp. 1–20, 2016.
[143] A. C. Hatch *et al.*, "1-Million droplet array with wide-field fluorescence imaging for digital PCR," *Lab Chip*, vol. 11, no. 22, p. 3838, 2011.
[144] S. H. Kim, S. Iwai, S. Araki, S. Sakakihara, R. Iino, and H. Noji, "Large-scale femtoliter droplet array for digital counting of single biomolecules," *Lab Chip*, vol. 12, no. 23, pp. 4986–4991, 2012.
[145] P. Abbyad, R. Dangla, A. Alexandrou, and C. N. Baroud, "Rails and anchors: guiding and trapping droplet microreactors in two dimensions," *Lab Chip*, vol. 11, no. 5, pp. 813–821, 2011.
[146] A. Huebner *et al.*, "Static microdroplet arrays: a microfluidic device for droplet trapping, incubation and release for enzymatic and cell-based assays," *Lab Chip*, vol. 9, no. 5, pp. 692–698, 2009.
[147] N. Q. Balaban, J. Merrin, R. Chait, L. Kowalik, and S. Leibler, "Bacterial persistence as a phenotypic switch," *Science (80-.).*, vol. 305, no. 5690, pp. 1622–1625, 2004.
[148] N. Safa, M. Vaithiyanathan, S. Sombolestani, S. Charles, and A. T. Melvin, "Population-based analysis of cell-penetrating peptide uptake using a microfluidic droplet trapping array," *Anal. Bioanal. Chem.*, 2019.
[149] F. Courtois *et al.*, "An integrated device for monitoring time-dependent in vitro expression from single genes in picolitre droplets," *ChemBioChem*, vol. 9, no. 3, pp. 439–446, 2008.
[150] P. Athamanolap, K. Hsieh, L. Chen, S. Yang, and T.-H. Wang, "Integrated Bacterial Identification and Antimicrobial Susceptibility Testing Using PCR and High-Resolution Melt," *Anal. Chem*, vol. 89, p. 33, 2017.
[151] K. E. Mach, A. M. Kaushik, K. Hsieh, P. K. Wong, T. H. Wang, and J. C. Liao, "Optimizing peptide nucleic acid probes for hybridization-based detection and identification of bacterial pathogens," *Analyst*, 2019.
[152] W. Guan, L. Chen, T. D. Rane, and T. H. Wang, "Droplet Digital Enzyme-Linked Oligonucleotide Hybridization Assay for Absolute RNA Quantification," *Sci. Rep.*, 2015.
[153] A. M. Kaushik, K. Hsieh, L. Chen, D. J. Shin, J. C. Liao, and T. H. Wang, "Accelerating bacterial growth detection and antimicrobial susceptibility assessment in integrated picoliter droplet platform," *Biosens. Bioelectron.*, 2017.
[154] M. Baker, "Digital PCR hits its stride," *Nat. Methods*, vol. 9, no. 6, pp. 541–544, 2012.

[155] K. Yin *et al.*, “Stable Colloidosomes Formed by Self-Assembly of Colloidal Surfactant for Highly Robust Digital PCR,” *Anal. Chem.*, p. acs.analchem.9b00470, 2019.
[156] G. Du, Q. Fang, and J. M. J. den Toonder, “Microfluidics for cell-based high throughput screening platforms-A review,” *Analytica Chimica Acta*, vol. 903. pp. 36–50, Jan-2016.
[157] R. R. Pompano, W. Liu, W. Du, and R. F. Ismagilov, “Microfluidics using spatially defined arrays of droplets in one, two, and three dimensions.,” *Annu. Rev. Anal. Chem. (Palo Alto. Calif).*, vol. 4, pp. 59–81, 2011.
[158] H. N. Joensson and H. Andersson Svahn, “Droplet microfluidics-A tool for single-cell analysis,” *Angewandte Chemie - International Edition*, vol. 51, no. 49. pp. 12176–12192, 2012.
[159] C. M. O’Keefe, A. M. Kaushik, and T. H. Wang, “Highly Efficient Real-Time Droplet Analysis Platform for High-Throughput Interrogation of DNA Sequences by Melt,” *Anal. Chem.*, vol. 91, no. 17, pp. 11275–11282, 2019.
[160] T. Reungwetwattana, S. J. Weroha, and J. R. Molina, “Oncogenic pathways, molecularly targeted therapies, and highlighted clinical trials in non-small-cell lung cancer (NSCLC),” *Clinical Lung Cancer*, vol. 13, no. 4. pp. 252–266, Jul-2012.
[161] S. Guo *et al.*, “Identification and validation of the methylation biomarkers of non-small cell lung cancer (nsclc),” *Clin. Epigenetics*, vol. 7, no. 1, pp. 2–9, 2015.
[162] A. Hulbert *et al.*, “Early detection of lung cancer using DNA promoter hypermethylation in plasma and sputum,” in *Clinical Cancer Research*, 2017, vol. 23, no. 8, pp. 1998–2005.
[163] K. Lokk *et al.*, “Methylation markers of early-stage non-small cell lung cancer,” *PLoS One*, vol. 7, no. 6, 2012.
[164] S. Chakravorty *et al.*, “Rapid universal identification of bacterial pathogens from clinical cultures by using a novel sloppy molecular beacon melting temperature signature technique,” *J. Clin. Microbiol.*, vol. 48, no. 1, pp. 258–267, 2010.
[165] Q. Huang, Z. Liu, Y. Liao, X. Chen, Y. Zhang, and Q. Li, “Multiplex Fluorescence Melting Curve Analysis for Mutation Detection with Dual-Labeled, Self-Quenched Probes,” *PLoS One*, vol. 6, no. 4, p. e19206, Apr. 2011.
[166] E. Zonta *et al.*, “Multiplex Detection of Rare Mutations by Picoliter Droplet Based Digital PCR: Sensitivity and Specificity Considerations,” *PLoS One*, vol. 11, no. 7, 2016.
[167] A. Hulbert *et al.*, “Early detection of lung cancer using DNA promoter hypermethylation in plasma and sputum,” in *Clinical Cancer Research*, 2017.
[168] A. E. Teschendorff *et al.*, “Epigenetic variability in cells of normal cytology is associated with the risk of future morphological transformation,” *Genome Med.*, vol. 4, no. 24, Mar. 2012.
[169] S. Ramón y Cajal *et al.*, “Clinical implications of intratumor heterogeneity: challenges and opportunities,” *Journal of Molecular Medicine*. 2020.
[170] Cancer.org, “Survival Rates for Colorectal Cancer,” *Cancer*, 1996. [Online]. Available: https://www.cancer.org/cancer/colon-rectal-cancer/detection-diagnosis-staging/survival-rates.html. [Accessed: 05-Feb-2020].
[171] A. B. Knudsen *et al.*, “Estimation of Benefits, Burden, and Harms of Colorectal Cancer Screening Strategies,” *JAMA*, vol. 315, no. 23, pp. 2595–2609, Jun. 2016.
[172] T. F. Imperiale *et al.*, “Multitarget Stool DNA Testing for Colorectal-Cancer Screening,” no. 14, Apr. 2014.
[173] T. Venesio, G. Siravegna, A. Bardelli, and A. Sapino, “Liquid Biopsies for Monitoring Temporal Genomic Heterogeneity in Breast and Colon Cancers.,” *Pathobiology*, 2017.
[174] V. Taly *et al.*, “Multiplex picodroplet digital PCR to detect KRAS mutations in circulating

DNA from the plasma of colorectal cancer patients," *Clin. Chem.*, vol. 59, no. 12, pp. 1722–1731, 2013.
[175] M. L. Thomas and P. Marcato, "Epigenetic modifications as biomarkers of tumor development, therapy response, and recurrence across the cancer care continuum," *Cancers*, vol. 10, no. 4. Multidisciplinary Digital Publishing Institute, p. 101, 01-Apr-2018.
[176] V. Constâncio *et al.*, "Early detection of the major male cancer types in blood-based liquid biopsies using a DNA methylation panel."
[177] H. Luo *et al.*, "Circulating tumor DNA methylation profiles enable early diagnosis, prognosis prediction, and screening for colorectal cancer," 2020.
[178] Z. Lin *et al.*, "Combined Detection of Plasma ZIC1, HOXD10 and RUNX3 Methylation is a Promising Strategy for Early Detection of Gastric Cancer and Precancerous Lesions.," *J. Cancer*, vol. 8, no. 6, pp. 1038–1044, 2017.
[179] Z. Li *et al.*, "Methylation analysis of plasma cell-free DNA for breast cancer early detection using bisulfite next-generation sequencing," *Tumor Biol*, vol. 37, no. 10, pp. 13111–13119, Oct. 2016.
[180] A. Di Meo, J. Bartlett, Y. Cheng, M. D. Pasic, and G. M. Yousef, "Liquid biopsy: A step forward towards precision medicine in urologic malignancies," *Molecular Cancer*, vol. 16, no. 1. BioMed Central Ltd., 14-Apr-2017.
[181] C.-X. Song *et al.*, "5-Hydroxymethylcytosine signatures in cell-free DNA provide information about tumor types and stages," *Cell Res.*, vol. 27, no. 10, pp. 1231–1242, Oct. 2017.
[182] T. Ohki, S. Hongo, N. Nakada, A. Maeda, and M. Takeda, "Inhibition of neurite outgrowth by reduced level of NDRG4 protein in antisense transfected PC12 cells," *Dev. Brain Res.*, vol. 135, pp. 55–63, 2002.
[183] D. A. Ahlquist *et al.*, "Next-generation stool DNA test accurately detects colorectal cancer and large adenomas.," *Gastroenterology*, vol. 142, no. 2, pp. 248–56; quiz e25-6, Feb. 2012.
[184] V. Melotte *et al.*, "N-Myc Downstream-Regulated Gene 4 (NDRG4): A Candidate Tumor Suppressor Gene and Potential Biomarker for Colorectal Cancer," *JNCI J. Natl. Cancer Inst.*, vol. 101, no. 13, pp. 916–927, Jul. 2009.
[185] T. Mikeska, I. L. Candiloro, and A. Dobrovic, "The implications of heterogeneous DNA methylation for the accurate quantification of methylation," *Epigenomics*, vol. 2, no. 4, pp. 561–573, 2010.
[186] R. Siegel, C. Desantis, and A. Jemal, "Colorectal Cancer Statistics, 2014," *CA Cancer J. Clin.*, vol. 64, no. 1, pp. 104–17, 2014.
[187] S. I. Labidi-Galy *et al.*, "High grade serous ovarian carcinomas originate in the fallopian tube," *Nat. Commun.*, vol. 8, p. 1093, Dec. 2017.
[188] L. A. Torre *et al.*, "Ovarian cancer statistics, 2018," *CA. Cancer J. Clin.*, vol. 68, no. 4, pp. 284–296, 2018.
[189] R. D. Cress, Y. S. Chen, C. R. Morris, M. Petersen, and G. S. Leiserowitz, "Characteristics of Long-Term Survivors of Epithelial Ovarian Cancer."
[190] R. J. Kurman and I. M. Shih, "Molecular pathogenesis and extraovarian origin of epithelial ovarian cancer - Shifting the paradigm," *Human Pathology*. 2011.
[191] N. N. Nik, R. Vang, I.-M. Shih, and R. J. Kurman, "Origin and Pathogenesis of Pelvic (Ovarian, Tubal, and Primary Peritoneal) Serous Carcinoma," *Annu. Rev. Pathol. Mech. Dis.*, 2014.
[192] R. J. Kurman and I. M. Shih, "The dualistic model of ovarian carcinogenesis revisited,

revised, and expanded," *Am. J. Pathol.*, 2016.
[193] C. P. DeSimone, M. E. Day, M. M. Tovar, C. S. Dietrich, M. L. Eastham, and S. C. Modesitt, "Rate of pathology from atypical glandular cell Pap tests classified by the Bethesda 2001 nomenclature," *Obstet. Gynecol.*, vol. 107, no. 6, pp. 1285–1291, Jun. 2006.
[194] I. Kinde *et al.*, "Evaluation of DNA from the papanicolaou test to detect ovarian and endometrial cancers," *Sci. Transl. Med.*, 2013.
[195] Y. Wang *et al.*, "Evaluation of liquid from the Papanicolaou test and other liquid biopsies for the detection of endometrial and ovarian cancers.," *Sci. Transl. Med.*, vol. 10, no. 433, p. eaap8793, 2018.
[196] I. M. Shih *et al.*, "Distinct DNA methylation profiles in ovarian serous neoplasms and their implications in ovarian carcinogenesis," *Am. J. Obstet. Gynecol.*, 2010.
[197] C. A. Barton, N. F. Hacker, S. J. Clark, and P. M. O'Brien, "DNA methylation changes in ovarian cancer: Implications for early diagnosis, prognosis and treatment," *Gynecologic Oncology*. 2008.
[198] M. A. Earp and J. M. Cunningham, "DNA methylation changes in epithelial ovarian cancer histotypes," *Genomics*, vol. 106, no. 6, pp. 311–321, Dec. 2015.
[199] O. Koukoura, D. A. Spandidos, A. Daponte, and S. Sifakis, "DNA methylation profiles in ovarian cancer: Implication in diagnosis and therapy (Review)," *Molecular Medicine Reports*. 2014.
[200] C. C. Chang *et al.*, "The feasibility of detecting endometrial and ovarian cancer using DNA methylation biomarkers in cervical scrapings," *J. Gynecol. Oncol.*, 2018.
[201] G. S. Watts, B. W. Futscher, N. Holtan, K. Degeest, F. E. Domann, and S. L. Rose, "DNA methylation changes in ovarian cancer are cumulative with disease progression and identify tumor stage," 2008.
[202] T. R. Pisanic *et al.*, "Methylomic analysis of ovarian cancers identifies tumor-specific alterations readily detectable in early precursor."
[203] T. E. Bartlett *et al.*, "Epigenetic reprogramming of fallopian tube fimbriae in BRCA mutation carriers defines early ovarian cancer evolution," *Nat. Commun.*, vol. 7, no. May, 2016.
[204] T. R. Pisanic *et al.*, "Methylomic analysis of ovarian cancers identifies tumor-specific alterations readily detectable in early precursor lesions," *Clin. Cancer Res.*, vol. 24, no. 24, pp. 6536–6547, Aug. 2018.

Curriculum Vitale

Christine Mangione O'Keefe

514 South Washington Street
Baltimore, MD 21231
(410) 419-9650
cmokeefe@jhmi.edu

Johns Hopkins University
School of Medicine
Department of Biomedical Engineering
Clark Hall, Room 122
Baltimore, MD 21218

EDUCATION

Johns Hopkins University, Ph.D. in Biomedical Engineering, March 2020 (expected)
School of Medicine, Department of Biomedical Engineering, GPA: 3.9

University of Maryland, College Park, B.S. in Bioengineering, May 2013
University Honors College, A. James Clark School of Engineering, Summa Cum Laude, GPA: 4.0

BIOGRAPHICAL SKETCH

Christine O'Keefe received her PhD in Biomedical Engineering from Johns Hopkins University. During her undergraduate studies, she designed an RF-based tracking device to monitor endotracheal tube positioning and prevent distal migration into the lungs during intubation. She also developed an ode-based computational model of neuronal outgrowth in response to calcium gated ion channel activity. While pursuing her graduate degree, Christine developed a microfluidic platform to detect and quantify epigenetic heterogeneity with respect to DNA methylation, particularly for rare species identification in liquid biopsies. She has gained extensive experience in microfabrication, assay optimization, thermal stabilization, image processing, and data processing and analysis methods. She is part of a cancer research team using the microfluidic digital HRM platform to investigate the utility of epigenetic heterogeneity in diagnostics, theranostics, and mechanistic studies.

AWARDS AND FELLOWSHIPS

National/ International

- Siebel Scholar Award, 2019
- Transducers/Eurosensors Best Paper, 2019
- P.E.O. PSA Scholar Fellowship, 2018
- MicroTAS Travel Award, 2018
- BMES Graduate Design and Research Award, 2017

University-wide

- Institute of NanoBioTechnology Annual Graduate Poster Competition, 1st Place, 2019
- Institute of NanoBioTechnology Business Pitch Competition, 1st Place, 2019
- NIH Biomedical Engineering Training Grant, Johns Hopkins University, 2013

- Graduate Research Fellowship, National Science Foundation, 2014-2018
- Banneker/Key Scholarship, 2009-2013
- Maryland Distinguished Scholar, 2009-2013
- National Merit Scholar, 2009-2013
- Primannum Honor Society, 2009
- Fischell Department of Bioengineering Outstanding Senior Award, 2013

RESEARCH EXPERIENCE

Department of Biomedical Engineering, School of Medicine, Johns Hopkins University
Doctoral Research 2013-present
Research Advisor: Dr. Tza-Huei "Jeff" Wang

- Developed imaging system and biological assay for ultra-sensitive high-throughput epigenetic identification of DNA methylation biomarkers in circulating DNA
- Developed simple and facile soft lithography microfabrication technique for PDMS-based microfluidic chips to withstand high temperature assays
- Computational investigation of image processing and data filtering techniques for high-throughput analysis of large microarray fluorescence images
- Automated serial sample loading system for high throughput screening of reagents on a droplet digital BioMEMs device
- Developed an image processing pipeline for segmentation, filtering, and co-registering uCT and uMR images of angiogenesis in mouse tumors

Department of Systems Biology, George Mason University and University of Maryland, Baltimore
Undergraduate Research June 2012-December 2012
Research Advisor: Dr. Saleet Jafri

- Modeled dynamics of the development of the human neuronal growth cone using ode computational models in Matlab and Fortran

Department of Kinesiology, University of Maryland, College Park
Undergraduate Research October 2011- May 2012
Research Advisor: Dr. John Jeka

- Measured effects of cerebellum frequency stimuli on postural control using a Vicon system

TEACHING EXPERIENCE

Johns Hopkins University
Teaching Assistant, Cell and Tissue Engineering Lab, Fall 2018, Spring 2019

- Gave introductory lectures on microfabrication, its techniques and applications
- Led team-based laboratory exercises in photolithography, soft lithography, and metal etching
- Developed discussion questions for exams and laboratory reports

Teaching Assistant, Biomedical Engineering Modeling & Design, Fall 2017

- Directed laboratory experiments developing and testing models of human kinetics

- Led discussion sections
- Graded laboratory reports

Teaching Assistant, Systems Pharmacology and Personalized Medicine, Spring 2017
- Developed rubric for computational assignments modeling pharmacokinetics
- Graded homework assignments and assisted with project completion

Teaching Assistant, Cell and Tissue Engineering Lab, Spring 2017
- Led cleanroom laboratory exercises in photolithography and soft lithography techniques
- Developed discussion questions and graded lab reports

United States Naval Academy
Intern, Summer 2010
- Led summer project for high school students in designing and constructing a SeaPerch underwater navigation robot

University of Maryland, College Park
Teaching Fellow, Women in Engineering, Summer 2010
- Lead multidisciplinary engineering lab projects including building a solar powered car, animation using Scratch, Dance pad Mania using electrical circuits for middle school students

PROFESSIONAL EXPERIENCE

Enterprise Sciences
Intern, December 2012-August 2013
- Developed interactive software and ran experiments with novel blood clotting devices
- Developed and performed automated data analysis procedures
- Prepared daily reports of experimental performance and statistical analysis

GO Consulting, Inc.
Social Media and Website Analytics Manager, 2005-present
- Developed and administered client social media accounts
- Analyzed website and social media traffic data and presented quarterly analytics reports

ACADEMIC SERVICE

Johns Hopkins University
Biomedical Engineering Extramural Development in Graduate Education (EDGE)
President 2017-2018, *Treasurer* 2015-2017, *Director of Public Relations* 2013-2015
- Coordinated efforts to educate graduate students in predominantly non-academic career paths
- Hosted speakers to discuss professional development, career paths, and career milestones
- Facilitated Ph.D.-level internships with companies related to biomedical engineering
- Co-hosted a career fair geared toward biomedical scientists and Ph.D. graduates
- Managed the budget through the administrative "Systems, Applications, and Products in Data Processing" (SAP) system and processed reimbursements

STEM Achievement in Baltimore City Elementary School Students (SABES)
Mentor, 2016-2018

- Led semester-long projects that teach engineering concepts and community involvement to elementary students at Baltimore city elementary schools

Women in Science and Engineering Mentorship Program (WISE)
Mentor, 2019
- Mentored high school student over a semester-long project to fabricate and test a microfluidic device and understand the research process in biomedical engineering

University of Maryland, College Park
Flexus Women in Engineering Living & Learning Community
Tutor, 2010-2012
- Tutored freshmen and sophomore women in engineering and STEM classes

PUBLICATIONS

Journal papers:

O'Keefe C., Pisanic T., Zec H., Overman M., and Wang T.-H. *Facile Profiling of Molecular Heterogeneity by Microfluidic Digital Melt.* Science Advances, 4, (September 2018), eaat6459.

O'Keefe C., Giammanco D., and Wang T.-H. *Multilayer digital device for highly efficient capture and parallelized analysis of rare molecules*. Lab on a Chip, 19, (January 2019), 444, doi: 10.1039/c8lc01189c

O'Keefe C., Li, S., and Wang T.-H. *Digital DNA sequence profiling of rare epigenetic cancer biomarkers in a highly parallelized microfluidic platform.* Analytical Chemistry, 91, (July 2019), 11275-11282, doi: 10.1021/acs.analchem.9b02346.

Athamanolap, P., Hsieh W., **O'Keefe C.**, Zhang Y., Wang T-.H. *Nanoarray digital PCR with high-resolution melt enables broad bacteria identification and pheno-molecular antimicrobial susceptibility test*. Analytical Chemistry, 91, (September 2019), 12784-12792, doi: 10.1021/acs.analchem.9b02344.

O'Keefe C., Zhang Y., Pisanic T., Herman, J., and Wang T.-H. *Ratiometric Probe-ID Scheme for Multiplexed Analysis of Methylation Heterogeneity by Microfluidic Digital Melt*. (Manuscript in preparation).

O'Keefe C., Pisanic T., Zhang Y., Wang T.-L., Wang Y., and Wang T.-H. *Sensitive Analysis of Methylation Heterogeneity in Pap specimens for Detecting Ovarian Cancer*. (Manuscript in preparation).

Peer reviewed conference paper

Zec, H., **O'Keefe, C.**, Ma, P., Wang, T.H. *Ultra-Thin, Evaporation-Resistant PDMS Devices for Absolute Quantification of DNA Using Digital PCR*. Proc. 18th International Conference on Solid-State Sensors, Actuators and Microsystems (Transducers 2015), p.536-539, 2015, doi: 10.1109/TRANSDUCERS.2015.7180979

O'Keefe, C., Pisanic, T., and Wang, T.H. *Digital High Resolution Melt Platform for Assessing Epigenetic Heterogeneity on a Microfluidic Chip*. Proc. 21st International Conference on

Miniaturized Chemical and Biochemical Analysis Systems (micro-TAS 2017), p. 1267-1268, 2017

O'Keefe, C. and Wang, T.H. *Digital High-Resolution Melt Platform for Rapid and Parallelized Molecule-by-Molecule Genetic Profiling.* Proc. 40th Annual International Conference of the IEEE Engineering in Medicine and Biology Society (EMBC 2018), p. 5342-5345, 2018, doi: 10.1109/EMBC.2018.8513609

O'Keefe C., Li, S.., and Wang T.-H. *High-throughput real-time profiling of rare molecules with highly efficient droplet digital microfluidics.* Proc. 20th International Conference on Solid-State Sensors, Actuators and Microsystems (Transducers 2019)

PATENT APPLICATIONS

U.S. Patent Application 62870258: High-Throughput Microfluidic Platform for High-Density Immobilization and Parallelized Quantitative Real-Time Measurements of Droplets. **O'Keefe, C.**, Wang, T.H., Kaushik, A., (Filed July 3, 2019). Patent Pending.

CONFERENCE PRESENTATIONS

Oral

O'Keefe C., Pisanic T., Athamanolop P., Zec H., and Wang T.-H. *Microfluidic Digital Melt Array for Accessing Rare Methylation Biomarkers in Cancer*. Paper presented to Biomedical Engineering Society Annual Meeting. Minneapolis, Minnesota. (October 2016)

O'Keefe C., Pisanic T., and Wang T.-H. *Ultra-Sensitive Digital Detection of Epigenetic DNA Methylation Heterogeneity*. Paper presented to Biomedical Engineering Society Annual Meeting. Phoenix, Arizona (October 2017)

Poster

Pisanic T., **O'Keefe C.**, Athamanolap P., Poh W., Chen C., Hulbert A., Brock M., Herman J., and Wang T.-H. *Digital Detection of DNA Methylation Heterogeneity from Liquid Biopsies*. Poster presented to Johns Hopkins Institute for NanoBioTechnology and Physical Sciences-Oncology Center Annual Symposium Poster Session. Baltimore, Maryland. (May 2017)

O'Keefe C., Pisanic T., and Wang T.-H. *Profiling Molecular Heterogeneity by Microfluidic Digital Melt*. Poster presented to Women in STEM Symposium. Baltimore, Maryland (April 2018)

O'Keefe C., Pisanic T., and Wang T.-H. *Profiling Rare Molecules by Digital Melt.* Poster presented to Johns Hopkins Institute for NanoBioTechnology Annual Symposium Poster Session. Baltimore, Maryland. (May 2019)

PROFESSIONAL ASSOCIATIONS/ MEMBERSHIPS

- Member, Theta Tau, Eta Delta Chapter, 2011 – present

- Student Member, Biomedical Engineering Society, 2013 – present
- Student Member, IEEE EMBC, 2018
- Student Member, Women in Engineering, 2011 – present